Study on the Growth Anomaly in Al-Ni Melts under Gravity and Microgravity Conditions

Dissertation

zur Erlangung des akademischen Grades

doctor rerum naturalium (Dr. rer. nat.)

vorgelegt dem Rat der Physikalisch-Astronomischen Fakultät

der Friedrich-Schiller-Universität Jena

von M. Sc., Marcus Reinartz

geboren am 17. Januar 1991 in Köln

Gutachter

1. Prof. Dr. rer. nat. habil. Markus Rettenmayr
Otto-Schott-Institut für Materialforschung
Friedrich-Schiller-Universität Jena

2. Priv.-Doz. Dr. rer. nat. Jürgen Brillo (Korreferent)
Fakultät für Georessourcen und Materialtechnik
Rheinisch-Westfälische Technische Hochschule Aachen (RWTH Aachen)

Institut für Materialphysik im Weltraum
Deutsches Zentrum für Luft- und Raumfahrt (DLR)

3. Prof. Dr.-Ing. habil. Manja Krüger
Institut für Werkstoff- und Fügetechnik (IWF)
Otto-von-Guericke-Universität Magdeburg

Tag der Disputation: 26.06.2020

Zusammenfassung

In dieser Arbeit wird das Erstarrungsverhalten verschiedener Al-Ni Legierungen mit Hilfe der Methode der elektromagnetischen Levitation (EML) untersucht. Von besonderem Interesse ist eine Wachstumsanomalie, bei der eine abnehmende Wachstumsgeschwindigkeit mit zunehmender Unterkühlung beobachtet wurde. Theoretische Modelle erwarten jedoch eine zunehmende Wachstumsgeschwindigkeit mit zunehmender Unterkühlung. Um diese Anomalie genauer zu untersuchen, werden Levitationsexperimente sowohl auf der Erde ($1g$) als auch im elektromagnetischen Levitator auf der Internationalen Raumstation (ISS) in Mikrogravitation (μg) durchgeführt. Der elektromagnetische Levitator auf der ISS (ISS-EML) bietet eine einzigartige Experimentierumgebung in μg, in der die äußeren Einflüsse deutlich verringert sind.

Die neuen Ergebnisse, die aus den Experimenten in μg und $1g$ gewonnen wurden, zeigen in Bezug auf die Wachstumsgeschwindigkeit keinen Unterschied. Hochgeschwindigkeitsvideos, die während der Erstarrung aufgenommen wurden, zeigen ein unerwartetes Verhalten. Die sichtbare Front besteht aus vielen kreisförmigen Strukturen, die wachsen und nacheinander entstehen, sogenannte Schuppen. Die gemessene Frontgeschwindigkeit ist daher eine Überlagerung aus dem Entstehen von neuen und Wachsen der vorhandenen Schuppen. Begleitende Mikrostrukturuntersuchungen von Proben, die auf der Erde prozessiert wurden, zeigen, dass die Schuppen einzelnen Keimstellen entsprechen. Daraus wird gefolgert, dass die beobachtete Front keine dendritische Wachstumsfront, sondern eine Nukleationsfront ist. Dies löst den Widerspruch zwischen den experimentellen Ergebnissen und den theoretischen Erwartung, die für dendritisches Wachstum ausgelegt sind, auf.

Zum genaueren Verständnis ihres Verhaltens wird die Nukleationsfront genauer untersucht. Dazu wird die Anzahl der Schuppen sowie deren Größe gemessen. Es

zeigt sich, dass bei zunehmender Unterkühlung weniger, jedoch größere Keime entstehen. Der Verlust an Keimen wird nicht durch die größere Fläche ausgeglichen, und führt daher zu einem Abfall der Frontgeschwindigkeit. Die Geschwindigkeit der Dendriten kann auf Grund der Opazität der Schmelzen nicht gemessen werden. Wenn von den Keimen Dendriten radial in die Probe wachsen, sollten sich diese an einem Punkt in der Probe treffen. Dieser Punkt ist bestimmt durch die dendritische Wachstumsgeschwindigkeit. In Gefügeanalysen zeigt sich, dass sich die Dendriten meist im Probenmittelpunkt treffen. Dies lässt darauf schließen, dass die dendritische Wachstumsgeschwindigkeit deutlich kleiner als die Geschwindigkeit der Front ist.

Abstract

In this thesis the solidification behavior of different Al-Ni alloys is studied by means of the electromagnetic levitation (EML) technique. Of special interest is an anomaly of the growth behaviour, a decreasing solidification velocity for increasing undercooling. However, according to theoretical considerations the growth velocity should increase with increasing undercooling. In order to study the anomaly, levitation experiments on earth ($1g$) as well as levitation experiments using the electromagnetic levitation facility on board the International Space Station (ISS) are carried out. The electromagnetic levitator on board the ISS (ISS-EML) provides a unique processing environment in microgravity μg where external influences are severely reduced.

The new results obtained in μg and $1g$ show no difference in terms of the growth velocity. However, the high-speed video data used to capture the solidification show an unexpected behaviour. The visible front consists of circular features which grow and consecutively form, referred to as scales. The measured front velocity is therefore a superposition of formation of new and growth of the existing scales. Accompanying microstructure analyses of samples processed on earth show that each scale corresponds to a nucleation event. It is concluded that the observed front is not a dendritic growth front, but a nucleation front. This resolves the contradiction between experimental results and theoretical considerations since the theoretical approaches are valid only for dendritic growth fronts.

For a better understanding of its behaviour, the nucleation front is studied in greater detail. The number and size of the scales is measured. It is found that for an increasing undercooling fewer, yet larger scales form. The loss of nuclei is not compensated by the larger area, and therefore leads to a decrease of the front velocity. The velocity of the dendrites cannot be measured due to the opacity of

the melt. If dendrites grow from the nuclei towards the sample centre, they should meet at one point inside the sample. This point is determined by the dendritic growth velocity. Microstructure analyses show that the dendrites often intersect at the sample centre. This leads to the conclusion that the dendritic growth velocity is significantly smaller than the front velocity.

Contents

CHAPTER 1

Introduction

In modern industry, the knowledge about material properties is crucial to obtain the best material for an application. The applied casting method plays a decisive role during the production process. Achieving the optimal result requires detailed knowledge about the casting method, solidification and microstructure. For many applications, Al-based alloys are still the materials of choice. In aerospace and automotive systems, Al-Ni alloys are often used because of their low specific mass and excellent corrosion resistance.

To elucidate the different material properties, an abundance of possible processing routes and testing devices is available. One processing route is the application of levitation techniques where a sample is containerlessly processed. Containerless processing reduces the number of heterogeneous nucleation sites, and therefore allows to keep a sample completely liquid below the liquidus temperature; the melt is undercooled. By using the electromagnetic levitation (EML) technique, undercoolings of several hundred Kelvin can be reached. EML uses high-frequency alternating electromagnetic fields to counteract the gravitational pull on earth [1]. High-speed cameras can then be used to capture the solidification front propagating along the sample surface.

From a theoretical and intuitive point of view, it is expected that the front velocity becomes larger the greater the undercooling is [2,3]. A decade ago, however, EML was used to study the solidification behaviour of Al-Ni alloys. In Refs. [4,5] it is reported that the dendrite growth velocity decreases for increasing undercooling. A decrease or even a drop in the growth velocity occurs for several other alloys. In

contrast to these cases, the anomaly in Al-Ni cannot be explained in terms of the usual rationales, like glass formation or different primary phases.

Besides experiments on ground, sounding rocket missions providing microgravity μg conditions were used to study the solidification [4, 5]. The usage of EML during sounding rocket missions allows to reduce the gravitational force acting on the sample, and provides an experimental environment with lesser disturbances. Yet, the data obtained in microgravity was scarce, and the anomaly was never explained. Modelling approaches were also made which were not able to reproduce the negative slope of the velocity-vs.-undercooling relation.

In this thesis, the main question is on the reason for the anomalous behaviour of the growth front velocity. Besides the reason which will be proven as responsible for the anomaly, other possible explanations are discussed in terms of the new results.

The study of the solidification behaviour will be carried out using data obtained on ground and in space using the EML facility on board the International Space Station (ISS-EML) which is expected to complement the available data and to elucidate the behaviour of the front velocity in μg. The front morphology and its dependence on the undercooling also provide information about the solidification process and are studied alongside on ground and in space. A difference between the front velocity and the dendrite growth velocity is found. From microstructure analysis, a first suggestion for the dendrite growth velocity is given.

CHAPTER 2

Literature review

2.1 Experimental and theoretical approach to nucleation

In order to initiate solidification, a nucleus of critical size needs to form. The most simple case for solidification is the nucleation due to atomic motion which is called homogeneous nucleation. Volmer and Weber presented their considerations for condensation of supersaturated vapours in Ref. [6]. The Volmer-Weber approach was later extended by Becker and Döring in Ref. [7] to better suit the experimental conditions. A transfer of these theories onto solidification was presented by Fisher and Turnbull in Refs. [8, 9]. When nucleation is initiated by contact of the melt to a substrate or an impurity, e.g. oxides on the sample surface, heterogeneous nucleation takes place. Volmer presented first results on this process in Ref. [10].

From the above mentioned approaches, nucleation rates can be deduced. However, these are only valid in equilibrated systems. Due to the experimental conditions of rapid cooling, the system needs time to adapt to the new conditions. This leads to the so-called transient nucleation which describes the adaption time necessary for the formation of clusters and therefore a possible delay in the formation of a cluster of critical size [1, 11].

Descriptions of the developments in the experimental studies of nucleation with a special focus on levitation techniqes are given in [1, 12–14] which are used as a basis for the following paragraphs. The nucleation in an undercooled melt is mainly influenced by the structure of the melt, the nucleating phase, the nucleation

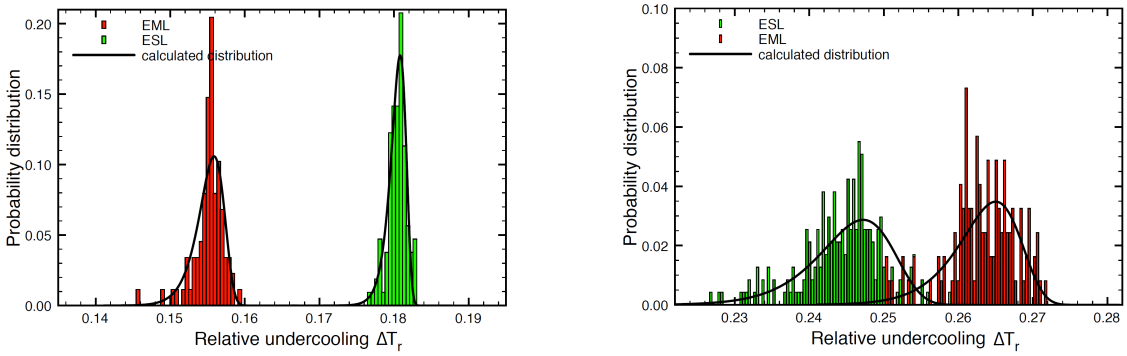

(a) Nucleation study in pure Zr melts.

(b) Nucleation study in $PdZr_2$ melts.

Figure 2.1: Results from nucleation studies with opposite results (images taken from [12]): larger undercoolings for pure Zr using the electrostatic levitation (ESL) technique (a) in contrast to larger undercoolings using the electromagnetic levitation (EML) technique for $PdZr_2$ (b).

barrier and the solid-liquid interfacial energy. Due to the containerless processing environment provided by electrostatic and electromagnetic levitation techniques, the determination of the short range order in the melt became easier [1, 14]. The measurements combined the levitation techniques with either neutron diffraction [15] or synchrotron radiation [16, 17]. First results using a resistor furnace were obtained by using neutron scattering on Al-Pd-Mn and Al-Mn-Cr samples [18, 19] and X-ray diffraction using Pb [20]. These measurements showed icosahedral short-range order for all examined systems. For pure Ni, Zr and Fe it is reported that the bulk liquid also shows the icosahedral short-range order independent of the nucleating phase [15]. In Refs. [16, 17], Kelton et al. identified the icosahedral short-range order in the liquid of pure Ni and Ti-Zr-Ni, too. In Ti-Zr-Ni it is reported in Refs. [16, 17] that an icosahedral quasi-crystalline phase nucleated first. In a second step, the expected C14 Laves phase formed. Therefore, it is suggested in Refs. [16, 17] that this preferred growth of the quasi-crystalline phase is enhanced by the icosahedral structure of the melt which reduces the nucleation barrier for the quasi-crystalline phase below the one for the Laves phase. Kelton et al. put forward that the short-range order in the liquid influences the phase selection and its nucleation. Besides the determination of the liquid structure, the same methods can be applied to determine the precipitating phase in a levitated sample [21–28]. For a description of the findings in the Al-Ni system, see Subsection 2.2.1.

To assess the nucleation barrier and the pre-factor of the nucleation rate density

from the classical nucleation theory [29], a statistical analysis of nucleation events during levitation can be applied, e.g. [1,12–14]. The analysis method was introduced by Skripov in Refs. [30,31]. At least 100 cycles need to be carried out [1]. From each cycle the undercooling is recorded, and the probability distribution for nucleation is calculated, as done for pure Zr and $PdZr_2$ in Fig. 2.1 [12]. Because of the independence of each nucleation event, a Poisson distribution can be fitted to the experimentally obtained data [12–14]. For pure Zr, it is evident in Fig. 2.1 (a) that deeper undercoolings were reached by using electrostatic levitation (ESL) technique than by means of electromagnetic levitation (EML) [12]. In contrast to that, the results for $PdZr_2$ in Fig. 2.1 (b) show deeper undercoolings for EML [12]. The prefactors K_V known from nucleation theory which were deduced from these results are $K_V = 10^{25}\,\mathrm{m^{-3}\,s^{-1}}$ for EML and $K_V = 10^{42}\,\mathrm{m^{-3}\,s^{-1}}$ for ESL using pure Zr [12]. In the case of the $PdZr_2$ alloy, the prefactors are $K_V = 10^{17}\,\mathrm{m^{-3}\,s^{-1}}$ for EML and $K_V = 10^{16}\,\mathrm{m^{-3}\,s^{-1}}$ for ESL, respectively [12]. Theoretical expectations of the prefactors are $K_V = 10^{39}\,\mathrm{m^{-3}\,s^{-1}}$ by Turnbull [29] or $K_V = 10^{41}\,\mathrm{m^{-3}\,s^{-1}}$ by Dantzig and Rappaz [32]. Only the ESL measurements on pure Zr are close to the expected results by Dantzig and Rappaz calculated for homogeneous nucleation [14]. The reasons for the different and even opposite results are still unclear [14].

Parallel to the development of the experimental techniques, simulation and modelling techniques were developed and improved. The different techniques which were developed are not described here. A detailed review of current results using phase-field simulations is given by Gránásy et al. in Ref. [33]. Gránásy et al. provide a short list of the possible techniques which were developed including further references in Ref. [33], like molecular dynamics, Monte Carlo, Brownian dynamics simulations, cluster dynamics techniques, Waals/Cahn-Hilliard/Ginzburg-Landau/Φ^4 models or more complex phase-field models. According to Ref. [33], these models all work on a length scale larger than the molecular or atomistic level, which has been overcome by new phase-field models, so-called phase-field crystal models. For further references, see [33].

A finding from the phase-field approaches is the observation of growth front nucleation, see Refs. [34–37] and references therein. Phase-field studies of an undercooled melt showed this behaviour for spherulitic solidification [38]. According to Ref. [38], faceted growth, weak density depletion at the solid-liquid interface and density fluctuations are necessary to promote the nucleation in the vicinity of the growth front. The formation of new grains is then initiated either by disloca-

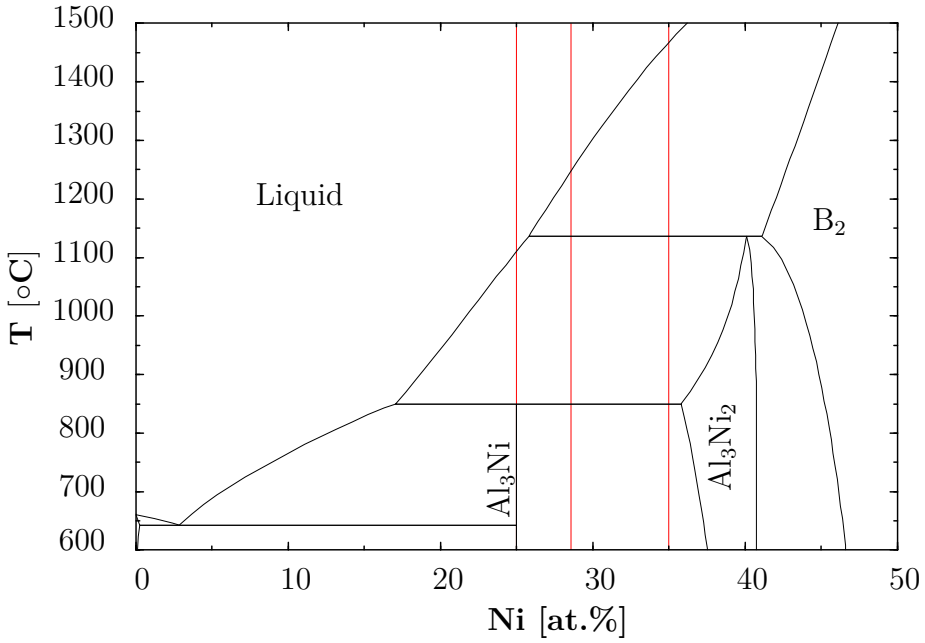

Figure 2.2: Phase diagram of the Al-Ni system calculated with FactSage [41] with red lines denoting the three compositions with $c_{\mathrm{Ni}} = 25\,\mathrm{at.\%}$, $28.5\,\mathrm{at.\%}$ and $35\,\mathrm{at.\%}$ examined in this thesis.

tions growing into the crystal or by small nuclei forming close to the interface. A molecular dynamics simulation with a billion atoms of pure Fe also reproduced the growth front nucleation in deeply undercooled melts [39]. In Ref. [39], the formation is attributed to an enhanced number of icosahedra in the melt close to the interface. As the description of all available literature on the subject of nucleation is not extensive here, more references can be found either in the already mentioned literature, or in [33, 40] and references therein.

2.2 Observed solidification behaviour in Al-Ni melts

This thesis is concerned with the solidification of different Al-Ni alloys. The velocity curves measured by Lengsdorf et al. [4, 5] show an anomalous behaviour of the growth velocity, i.e. the velocities decrease with increasing undercooling. Before going into detail on this, a short description of the phase diagram and the phase selection is necessary to elucidate the peculiarities of the Al-Ni system.

The phase diagram of the Al-rich side of the Al-Ni system is shown in Fig. 2.2. The three selected compositions for this work, i.e. $c_{\mathrm{Al}} = 25\,\mathrm{at.\%}$, $28.5\,\mathrm{at.\%}$ and $35\,\mathrm{at.\%}$ are marked with red lines. In the region of interest three phases are dominant,

Al_3Ni, Al_3Ni_2 and an AlNi phase with a B2 structure [42]. This AlNi phase is denoted as AlNi B2 in the following. For Al-28.5at.%Ni and Al-35at.%Ni it is expected that the AlNi B2 phase forms primarily. At a temperature of $T_{p1} = 1133\,°C$, the AlNi B2 phase transforms to Al_3Ni_2 according to the peritectic reaction $L + \text{AlNi B2} \rightarrow Al_3Ni_2$. Under equilibrium conditions, the Al_3Ni_2 phase primarily precipitates during the solidification of Al-25at.%Ni. A second peritectic reaction, $L + Al_3Ni_2 \rightarrow Al_3Ni$, occurs at a temperature of $T_{p2} = 854\,°C$. This denotation of T_{p1} and T_{p2} was already used by Shuleshova [23]. Because of segregation effects and isolated melt pools in the dendrite network inside the sample, a eutectic can also form at a temperature of $T_{eu} = 640\,°C$ with the reaction $L \rightarrow Al_3Ni + Al$.

Not included in the equilibrium phase diagram in Fig. 2.2 are metastable phases. Phase diagrams showing the range of existence is given in Refs. [23, 43]. This paragraph is a summary based on the description of the metastable phases in Al-Ni provided in [23]. Two different metastable phases were found by rapid solidification, a metastable decagonal quasicrystalline phase (D-phase) [44] and a metastable monoclinic Al_9Ni_2 phase [44–47]. The Al-Ni-Co system shows the same D-phase [43, 45] which allowed Grushko and Holland-Moritz to calculate the composition of the D-Phase in the Al-Ni system, yielding $c_{Ni} = 31\,\text{at.}\%$ [45]. A composition in the range of $c_{Ni} = 24$ to $30\,\text{at.}\%$ is documented in Ref. [47], which is in good agreement with the calculated value.

2.2.1 Phase selection in undercooled Al-Ni melts

According to the phase diagram, the phase selection strongly depends on the undercoolings prior to solidification if the metastable phases occured only in deeply undercooled samples. This was extensively studied by Shuleshova in high-energy synchrotron radiation experiments [23–27]. Because the Al-28.5at.%Ni alloy shows the same primary phase as the Al-31.5at.%Ni alloy, it is expected to show the same behaviour with respect to the primary phase and the subsequent transformations.

The measurements by Shuleshova et al. [23–27] on alloys with $c_{\text{Ni}} = 18$ to $25\,\text{at.}\%$ showed that the primary phase is always Al_3Ni_2. Rarely, no peritectic event was recorded within the temperature/time profile in Al-18at.%Ni, indicating that the Al_3Ni_2 did not form. However, the diffraction showed peaks for Al_3Ni_2 and Al_3Ni, indicating that both phases formed simultaneously. Furthermore, only a metastable D-phase formed after the first recalescence and before the peritectic reaction [23–27]. It only occurred in the temperature range of $T \approx 920$ to $975\,\text{K}$ and decomposed

completely before the microstructures could be examined.

In Al-31.5at.%Ni alloys, the undercooling had a significant influence on the phase selection according to Shuleshova et al. [23–27]. For $\Delta T < 320\,\mathrm{K}$, the AlNi B2 phase precipitates primarily. At deeper undercoolings, $\Delta T > 320\,\mathrm{K}$, Al_3Ni_2 forms. Nevertheless, the primary formation and instantaneous decomposition of the AlNi B2 phase could not be excluded as the reflections of Al_3Ni_2 mask those of AlNi B2 [23]. Also, the AlNi B2 was not found in fully solidified samples. Again, the metastable phase formed after the first recalescence event and the peritectic.

These changes in the primary phase were also observed with a model by Tourret et al. [48–51]. The model was applied to impulse atomization experiments since a direct observation of the thermal history of the droplets is not possible during the experiments, but also to electromagnetically levitated samples. For the gas atomization of Al-20at.%Ni, three different growth modes were identified depending on the diameter of the spheres [51]. For diameters $d \approx 120\,\mu\mathrm{m}$, Al_3Ni_2 grows with a simultaneous growth of the peritectic zone which is stopped and remelted due to the temperature increase. Consequently, the peritectic reforms and the solidification is completed by the eutectic. For the smallest diameters, $d \approx 10\,\mu\mathrm{m}$, the Al_3Ni_2 and Al_3Ni grow simultaneously, but the Al_3Ni overtakes the Al_3Ni_2 and hinders it growth. Therefore, only the eutectic reaction occurs and Al_3Ni and $\alpha - \mathrm{Al}$ are predominant in these samples. At intermediate diameters, the amount of Al_3Ni_2 increases continuously dominant primary phase finally changes.

Impulse atomization experiments by Ilbagi et al. [52–56] confirmed these modeling results for Al-20at.%Ni alloys. In droplets with $d < 165\,\mu\mathrm{m}$ the primary Al_3Ni_2 phase was suppressed. Also in X-ray scattering measurements, unidentified peaks were found which were attributed to the metastable D-phase. In particles of Al-22at.%Ni, Ilbagi observed that the amount of phases depends on the size of the droplets, which is directly correlated to the cooling rate [57]. Ilbagi et al. found also that in these alloys more than one heterogeneous nucleation site was present on the sample surface, and more porosity occurred in larger droplets. For Al-31.5at.%Ni experiments [52–56], Ilbagi et al. observed that the porosity is more randomly distributed in larger droplets whereas it is closer to the surface at smaller diameters.

Besides the application of the model by Tourret et al. to impulse atomization [48–51], electromagnetically levitated samples were also analysed [48, 50]. The model nicely described the thermal history of the levitated droplets including the height

of the recalescence events and the selected phases and their amounts [48,50]. In Al-25at.%Ni, Tourret et al. often observed three recalescence events, first the formation of Al_3Ni_2, followed by the peritectic reaction leading to the formation of Al_3Ni, and finally the eutectic reaction.

The model by Tourret et al. [48–51] showed that the primary formation of Al_3Ni_2 leads to the formation of the mushy zone, and also that the phase fraction increases upon cooling. When the peritectic Al_3Ni forms, the amount of Al_3Ni_2 drops, but not the entire fraction is transformed. Finally, the eutectic formation ends the solidification.

2.2.2 The growth anomaly in Al-Ni melts

Measurements of the velocity-vs.-undercooling relationship were carried out by Lengsdorf et al. [4, 5]. The results show an anomalous behaviour, see Fig. 2.3. For the Al-rich Al-Ni alloys the growth velocity decreases for increasing undercooling [4, 5]. The curve for Al-25at.%Ni shows an overall decrease which is interrupted by a small peak around $\Delta T \approx 150\,\mathrm{K}$. However, for larger Ni-contents up to $c_{\mathrm{Ni}} \leq 31.5\,\mathrm{at.\%}$, the velocity decreases monotonically. At higher Ni-contents, the velocity passes through a minimum around $\Delta T \approx 250\,\mathrm{K}$ for Al-35at.%Ni and $\Delta T \approx 175\,\mathrm{K}$ for Al-40at.%Ni, respectively. For $c_{\mathrm{Ni}} \geq 45\,\mathrm{at.\%}$, the curve shows the expected monotonic increase.

A first idea by Lengsdorf et al. [4, 5] was that this anomaly is due to forced convection in the levitated samples. This forced convection is induced by the strong electromagnetic fields acting on the sample which causes fluid flow velocities of the order of $0.32\,\mathrm{m\,s^{-1}}$ [58]. This strong influence was already confirmed in Al-50at.%Ni alloys processed in microgravity and on earth, showing a significantly reduced growth velocity in microgravity [59]. Yet, the influence is only observable if the growth velocity is of the order of the fluid flow velocity.

The results of the microgravity measurements by Lengsdorf et al. [4,5] are shown as the black triangles for the Al-31.5at.%Ni alloy in Fig. 2.3. These show a different behaviour compared to the ground data. The authors' conclusion from these two data points was that in microgravity the velocity follows the expected trend and the anomaly is due to the gravitational preconditions [4, 5].

The microstructure of the Al-31.5at.%Ni sample processed in microgravity was analysed by Ilbagi et al. [52]. The sample showed a solid layer beneath the surface, which Ilbagi et al. called outer rim. In there, the Al_3Ni_2 dendrites were found to

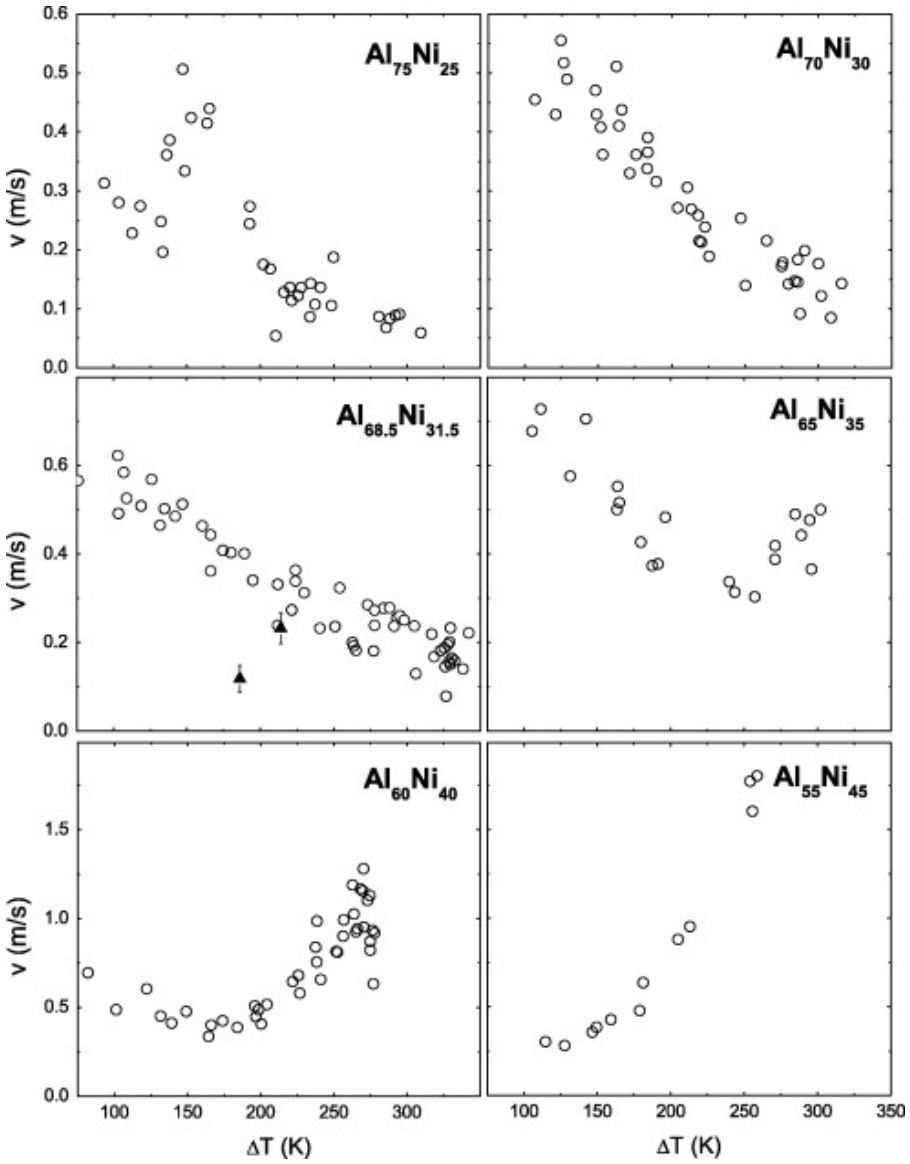

Figure 2.3: Extensive measurements of the velocity-vs.-undercooling relation carried out by Lengsdorf et al. [5] showing an anomalous behaviour of the growth velocity for increasing undercooling in Al-rich Al-Ni alloys.

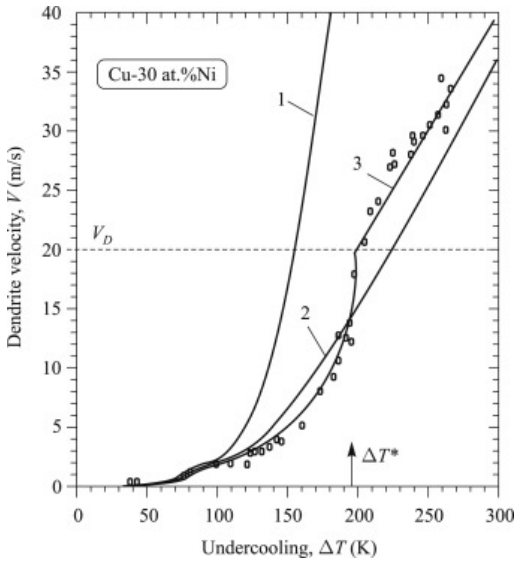

Figure 2.4: Measured and calculated growth velocity in Cu-30at.%Ni from [62, 63] showing a monotonous increase for increasing undercooling.

be enclosed by Al_3Ni and eutectic. However, the inner part of the sample showed a strong dominance of Al_3Ni_2 and porosity, but no eutectic. In Ref. [60] the whole sample is depicted, and it is visible that the inner part consists of dendrites pointing radially inwards to the sample centre, away from the surface. The shrinkage pores look like they are completely enclosed by the outer rim of the sample. It is suggested in Ref. [60] that due to heterogeneous nucleation on the sample surface only radially inwards pointing growth directions are allowed for the dendrites.

To determine the growth velocity of the solid-liquid interface, Lengsdorf et al. [4, 5] used a high-speed camera similar to [61]. This approach makes use of the visible height of the sample between the two windings of the coil of the EML and the time the front needs to propagate along the whole sample surface. It is assumed that the solid grows isotropically into the melt, i.e. the solid is spherical. Then, the visible sample height and the required time interval can be used to determine the growth velocity. Furthermore, it is implicitly assumed that nucleation occurs on the sample surface and not inside the bulk, and that only one nucleation event occurs.

2.2.3 Modelling approaches to the anomaly

Sharp-interface models for non-equilibrium solidification are capable of calculating the velocity-vs.-undercooling relationship. A class of models was developed by

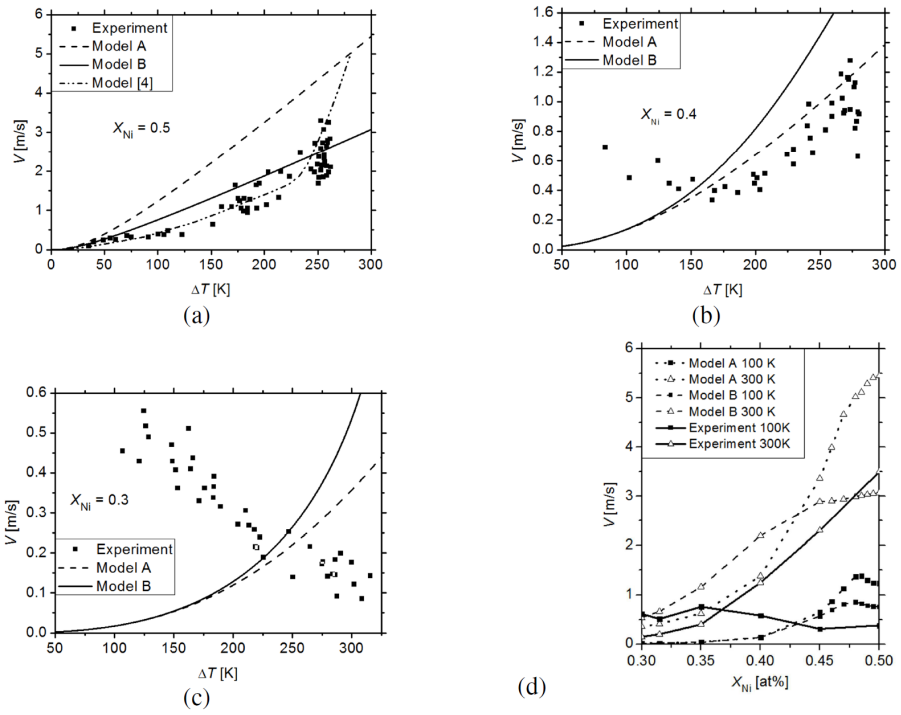

Figure 2.5: Modelling results by Ehlen [70, 71] with results in the correct order of magnitude capturing increasing branches well, but not reproducing the negative slope (taken from [70]).

Galenko in [62, 64]. Fig. 2.4 shows a representative result for the calculations in a Cu-30at.%Ni alloy. The velocity shows a monotonous increase for increasing undercooling. At an undercooling of $\Delta T^* \approx 200\,\mathrm{K}$, the growth behaviour changes due to solute trapping. Solute trapping describes the case where the growing solid has the same composition as the initial melt composition, i.e. $k(V) = \frac{c_s}{c_l} = 1$ [62,65, 66]. This describes the onset of diffusionless solidification for growth velocities $v \geq v_D$, where v_D is the diffusive speed [62]. When the atoms in intermetallic compounds are not able to form the correct lattice structure, it is called disorder trapping [1]. This has been reported in the Al-Ni system for Al-50at.%Ni by Hartmann [67]. However, this also leads to the same behaviour of a steep rise.

A maximum in the velocity curve was successfully modelled in Refs. [68, 69]. Nevertheless, the decreasing velocity or the minimum cannot be reproduced. To cope with this problem, modelling approaches were developed by Ehlen et al. in [70, 71] which are an extension of the sharp-interface models by Galenko, see references in [70, 71].

Ehlen et al. mainly concentrate on the AlNi B2 phase treating it either as a solid

solution (A) or an intermetallic phase (B). At the largest Ni-content, Al-50at.%Ni, the models capture the increasing trend. Denoted with "Model [4]" in Fig. 2.5, the results obtained by using a model presented in [67] including disorder-trapping at an undercooling of $\Delta T \approx 250\,\mathrm{K}$ are shown in Fig. 2.5. For Al-40at.%Ni, see Fig. 2.5(b), both models yield velocities close to the increasing branch. However, in Al-30at.%Ni in Fig. 2.5(c), it fails completely to capture the decreasing trend. When plotting the velocity for two different undercoolings, namely $\Delta T = 100\,\mathrm{K}$ and $\Delta T = 300\,\mathrm{K}$, the models show a decrease for lower Ni-contents, Fig. 2.5(d). Yet, the measured velocities at $\Delta T = 100\,\mathrm{K}$ show an increase which is not captured by the models.

By taking a closer look at the undercooling contributions, Ehlen noticed that the constitutional undercooling overrides the kinetic undercooling at low Ni-contents and low undercoolings. Because the velocity directly depends on the kinetic undercooling according to Ehlen, the velocity decreases with decreasing Ni-content, and the models are not able to reproduce the increasing velocity for decreasing Ni-contents. This leads Ehlen to the conclusion that there are effects not covered by modelling.

2.2.4 Reasons for the anomaly as proposed in literature

Ehlen et al. [70, 71] came to the conclusion that another mechanism is responsible for the growth anomaly. The suggestions for this are the following five [71]:

1. Convection influences the growth velocity. Ehlen directly refers to the available data on Al-31.5at.%Ni solidifying in microgravity by Lengsdorf [4, 5] which does not provide a conclusive correlation due to the small number of data points.

2. For the analysis it is often assumed that a single nucleus forms on the sample surface. The results obtained in microgravity by Lengsdorf et al. [4,5] indicate that multiple nucleation sites are located on the sample surface, and the assumption of a single nucleus is not met. Hence, the different parts of the velocity-vs.-undercooling relation with negative and positive slope could be due to different growth mechanism.

3. The solid does not grow in steady-state, concerning the uneven temperature distribution inside the sample. Ehlen et al. suggest that the sample is hotter

on the inside than on the surface due to cooling of the surface. This would require the use of temperature dependent heat and solute diffusivities in the models, which is not included. Indications are proposed that the velocity is not constant during solidification, especially during the final transient.

4. By equiaxed nucleation in the vicinity of the growth front, the propagation is sped up or slowed down.

5. The unknown influence of vacancies in the AlNi B2 phase could influence growth.

In his master thesis, Paul [72] also used electromagnetic levitation and observed that the front in Al-31.5at.%Ni and Al-40at.%Ni is build by circles which he called scales. The size of these scales is determined by the undercooling leading to larger scales at larger undercoolings. Furthermore, he suggests that these are nuclei forming in the vicinity of the growth front which block the growth, which is similar to the suggestion of equiaxed dendrites by Ehlen et al. [71]. Paul also indicated that different solidification mechanisms appear on branches featuring the negative slope and those with positive slope.

CHAPTER 3

The EML technique and sample preparation

3.1 Sample preparation for levitation and analysis

In the present thesis, electromagnetic levitation is applied to Al-Ni alloys with $c_{\mathrm{Ni}} = 25\,\mathrm{at.\%}$, $28.5\,\mathrm{at.\%}$ and $35\,\mathrm{at.\%}$. The samples are produced from High Purity Al 4N5 provided by Hydro Rolled Products, and Alfa Aesar Nickel rod 5N raw materials. The necessary amount for the samples is cut from the raw materials with a high precision linear saw (Buehler IsoMet 5000) and ground to the desired weight (Row Rathenau Metasinex). The pure metals are alloyed using a cold wall crucible for inductive melting, and composition is checked using EDX measurements. The samples are cut from the melting pearl and ground to a similar weight. Finally, the samples are cleaned and stored in isopropyl.

After processing, selected samples are analysed by means of tomography (Phoenix nanotom at the Institute of Materials Physics in Space, German Aerospace Centre (DLR), Cologne) and Scanning Electron Microscopy (LEO 1530 VP, Zeiss Merlin at DLR Cologne or Zeiss Evo 40 at FSU Jena). For embedding, an electrically conducting mounting resin (PolyFast, Struers with a Struers LaboPress-3) is used. Final polishing is done using a Buehler Pheonix 4000.

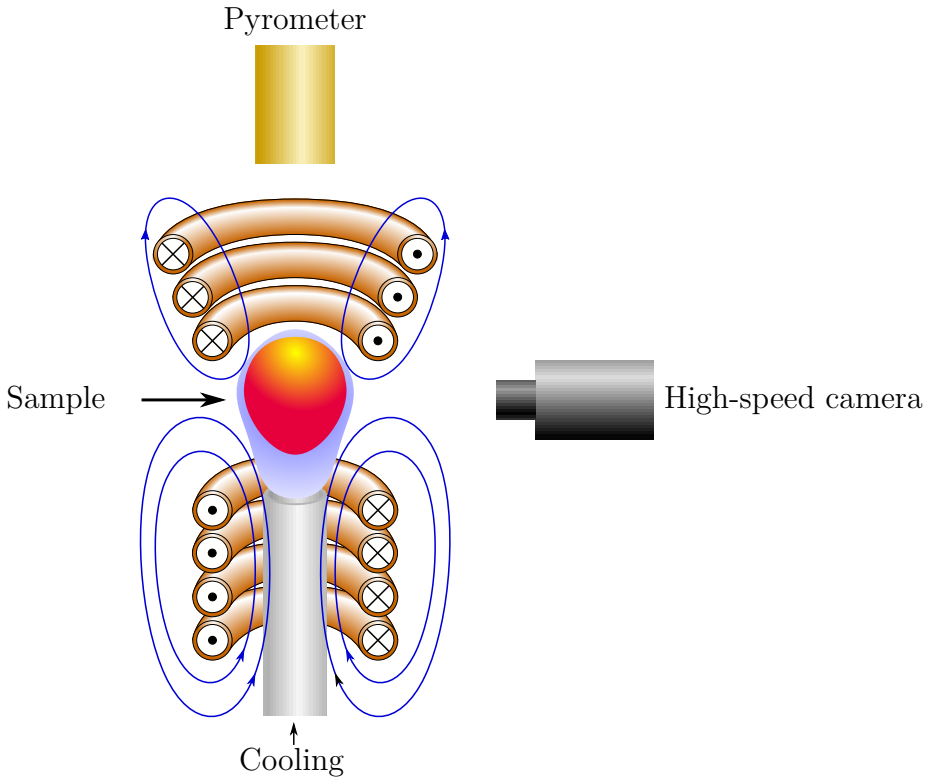

Figure 3.1: Schematic of a coil system used for electromagnetic levitation with the ability to cool the sample by directing a gas stream through the sample holder below the sample.

3.2 Description of the electromagnetic levitation

Electromagnetic levitation is a method for containerless solidification [1]. The samples have a diameter of 5 to 8 mm and are placed on a sample holder between two coils according to Fig. 3.1. An alternating current with a frequency of $f \approx 300\,\mathrm{kHz}$ and a power of $P = 0.5$ to $10\,\mathrm{kW}$ is applied to the coil generating an alternating electromagnetic field, see blue lines in Fig. 3.1. The lower coil windings create a field pointing upwards which, according to Lenz's rule, induces currents in the sample resulting in a magnetic field with the opposite orientation to the primary field. This leads to a repulsion of the sample from the lower coil, and a compensation of the gravitational force. Above the sample, a smaller coil is placed to dampen sample motion by generating an opposing electromagnetic field.

Because of the induced currents, the sample is not only levitated between the two coils, but also heated. To obtain a stable levitation, the power cannot be reduced below a lower limit. The temperature cannot be decreased independently of the levitation force leading to a minimum temperature in the levitated sample. The limit is not necessarily lower than the solidification temperature and depends strongly on the sample material and size as well as the coil geometry. For cooling below the low temperature limit, high purity He (6N) gas is guided onto the sample through the sample holder to cool the sample.

A high-speed camera detecting the visual range of light is used to monitor the solidification front. The camera is pointed at the sample with the field of view between the two coils. A pyrometer contactlessly measures the temperature/time profile. The temperature measurement is carried out on the top of the sample.

3.3 Advantages of experiments in microgravity

During experiments convection cannot be suppressed easily. Due to thermal or convectional gradients, buoyancy not only of the melt, see e.g. [73], but also of the growing solid occurs. Solidified parts can move through the melt because of a difference between their density and the density of the melt [74]. Gradients of the surface tension lead to Marangoni convection. In electromagnetically levitated samples, the strong electromagnetic field necessary for levitation leads to forced convection in the sample. The determination of fluid flow velocities due to forced convection inside levitated samples has been approached by Hyers et al. [58, 75, 76].

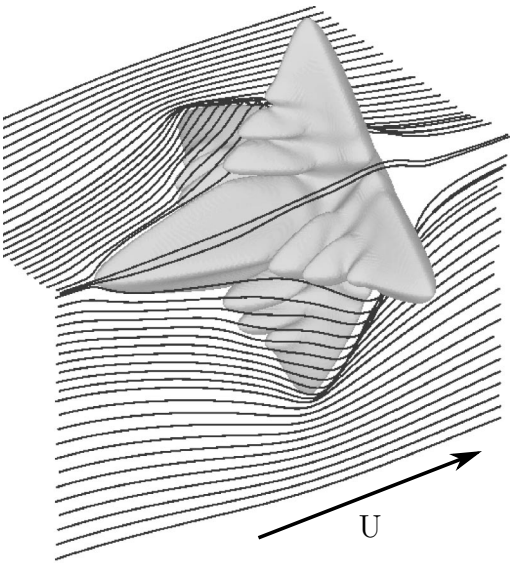

(a) Phase-field calculations exploring the influence of convection showing a pronounced growth against the direction of flow U (taken from [77]).

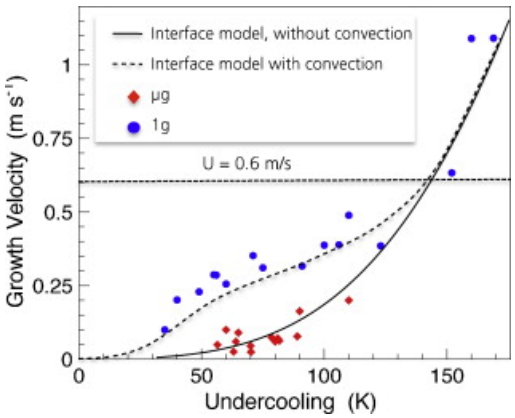

(b) Growth velocity measurements of Al-50at.%Ni [59] exhibiting a significant difference between measurements on ground (with convection) and in microgravity (withouth convection) (taken from [78]).

Figure 3.2: Fluid flow around a growing dendrite in Fig. 3.2 (a) obtained by phase-field simulations and its influence on the growth velocity, Fig. 3.2 (b).

The authors found that the fluid flow velocity in levitated samples on earth is of the order of $v_{\text{flow}} \approx 0.3\,\text{m}\,\text{s}^{-1}$ and $v_{\text{flow}} \approx 0.05\,\text{m}\,\text{s}^{-1}$ in microgravity, respectively. By comparison with experiments in microgravity, Hyers et al. were able to describe a change of the flow regime depending on the Reynolds number. The Reynolds number Re is defined by setting the inertial to viscous forces into relation [32]. For $Re > 600$ turbulent flow occurs, which was found for electromagnetic levitation on earth. Changing the experimental conditions to microgravity allows to reduce the external electromagnetic field leading to $Re < 600$ and laminar flow.

By using phase-field simulations, it was shown that the fluid flow around a growing dendrite significantly alters the growth behaviour, see Fig. 3.2 (a) [77]. The dendrite arm pointing against the flow direction is able to grow faster than the dendrites perpendicular. The dendrite arm parallel to the flow, behind the solid in Fig. 3.2 (a). The dendrite arms in the plane perpendicular to the flow direction show pronounced secondary branches pointing against the flow direction. This can be described phenomenologically, e.g. [61, 79]. When the solid grows, latent heat is released and, if the concentration differs between solid and liquid, the solid rejects

excess solute. This leads to the formation of temperature and concentration gradients around the solid. If the fluid now flows around the solid, it can transport the solute and heat away from the dendrite tip. The growth direction is then following the steepest gradients, and the dendrite grows into to the opposite direction of the fluid flow [79].

Measurements of the growth velocity in Al-50at.%Ni samples nicely show the influence of forced convection onto the solidification velocity [59]. The experiments carried out on earth show a significantly increased velocity (blue circles) compared to that from microgravity (red squares) in Fig. 3.2 (b). In order to model the influence of forced convection, sharp-interface models for non-equilibrium solidification were extended to include the fluid flow velocity, which are described in detail elsewhere [79, 80].

Besides the terrestrial (1g) experiments, experiments in microgravity (μg) were carried out using the electromagnetic levitation facility on board the International Space Station (ISS-EML) [81–84]. For the experiments, the Al-25at.%Ni and Al-35at.%Ni alloys were chosen. These experiments allow the measurement of a sample with a laminar fluid flow.

The electromagnetic levitator uses a decoupled heating and positioning system with a single coil producing a dipole field for heating and a quadrupole field for positioning [82]. Unlike levitation on earth, which induces strong fluid flow inside the sample, levitation in microgravity requires much weaker fields. The lack of gravity and the decoupled heating and positioning allows to significantly reduce the fluid flow inside the sample.

The ISS-EML is equipped with two cameras, one high-speed camera and a camera with a lower time resolution for observing the sample in real time. A trigger needle is also build into the sample holder. This trigger is used to initiate the solidification at a defined undercooling. Elaborate descriptions of the ISS-EML facility are presented in Refs. [81–84].

3.4 The conduction of a levitation cycle

During one experimental run, the samples are heated and cooled several times. During each cycle, the sample is thus melted and solidified. An exemplary cycle is shown in Fig. 3.3. This is a profile captured on board the ISS during processing of Al-25at.%Ni. A detailed interpretation of the profile is given in Subsection 4.1.1,

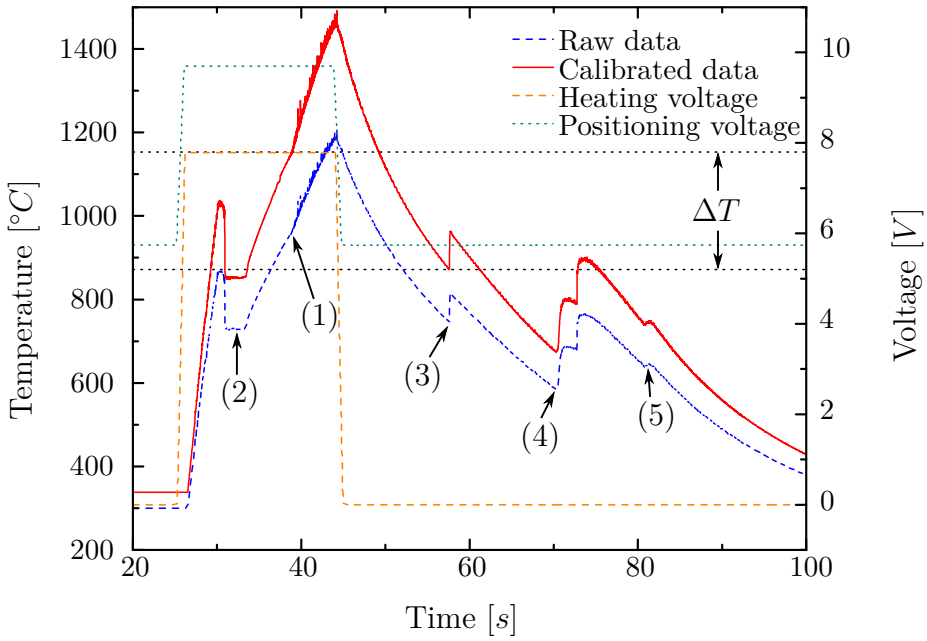

Figure 3.3: Temperature/time profile of an Al-25at.%Ni sample processed on board the ISS with higlighted important points: (1) liquidus temperature, (2) oxide evaporation, (3) first recalescence, (4) second and third recalescence, (5) fourth and last recalescence.

while in this section general aspects are discussed.

The diagram in Fig. 3.3 shows the measured temperature as a dashed blue line. As the temperature measurement relies on a pyrometer, the raw data do not directly provide the correct temperature and need to be calibrated according to [85],

$$\frac{1}{T} = \frac{1}{T^{\mathrm{pyr}}} + \frac{1}{T_l} - \frac{1}{T_l^{\mathrm{pyr}}}. \tag{3.1}$$

T^{pyr} is the temperature recorded by the pyrometer, T_l is the liquidus temperature according to the phase diagram, and T_l^{pyr} is the measured liquidus temperature. Applying this equation to the blue curve in Fig. 3.3 yields the red solid curve.

For the experiments in microgravity, extensive studies on the emissivity of the samples were carried out beforehand. As the surface is covered with oxides up to the temperature where their evaporation is observed, the determined emissivity value is not valid for higher temperatures, and during cooling not until oxide reformation. Therefore, between the oxide evaporation and reformation, the measured temperature data need to be calibrated. Although the emissivity changes for every transformation step in Al-Ni alloys, too, see also [23, 24, 50], only the temperature

curve calibrated to the liquidus temperature is shown as the undercooling before the first recalescence is of interest. The measured liquidus temperature T_l^{pyr} is set to the change of slope marked with number (1) in Fig. 3.3. At this point, the melting is completed, and the energy which is introduced into the sample is entirely used to heat up the sample. Hence, the slope increases.

The positioner and heater control voltages are also shown in Fig. 3.3. The sample is heated by switching on the heating field. During heating, the temperature shows a distinct decrease followed by a plateau marked with (2) in the graph. The temperature decrease is due to oxide evaporation. The oxides have a higher emissivity, leading to an overestimation of the real temperature. This has been described before for the Al-Ni system [23, 24, 50]. When the oxides evaporate, the clean metallic melt surface becomes visible for the pyrometer, and the temperature shows an artificial decrease.

Further heating initiates melting that is completed when the liquidus temperature (1) is reached. To improve the homogeneity of the melt and further reduce possible oxide residues on the sample surface, the sample is overheated. When the limit temperature is reached, the heater is switched off, the positioner control voltage is reduced, and the sample cools by radiative and convective heat loss. Due to the stochastic formation of nuclei, the rapid solidification starts at an arbitrary undercooling. The solidification can also be initiated by using a trigger needle which is brought into contact with the sample. When the rapid solidification starts, the release of latent heat heats up the sample. Recalescence events, (3), can occur several times because of different phase transformation steps, peritectic, marker (4), or eutectic, (5), reactions. The curve in Fig. 3.3 shows four different recalescence events after the beginning of solidification.

The undercooling is determined according to the respective equilibrium liquidus temperature of the solidifying phase. For example, the first recalescence represents the solidification of the primary phase (Al_3Ni_2 for the example in Fig. 3.3). The temperature difference between the liquidus temperature and the melt temperature right before the recalescence is defined as the relevant undercooling. This is marked by ΔT for the primary solidifying phase in Fig. 3.3, and in this case it is $\Delta T = 282\,\mathrm{K}$.

CHAPTER 4

Experimental results and discussion

4.1 Results for the Al-25at.%Ni alloy

The first investigated alloy was the Al-25at.%Ni alloy. As depicted in Fig. 2.3, a decreasing growth velocity over wide parts of measured undercoolings was observed at this Ni-content by Lengsdorf et al. [5]. Between $\Delta T = 125$ and 200 K, a peak in the velocity-vs.-undercooling curve is observed. However, due to the overall negative trend of the velocity curve measure on earth, this alloy was processed on board the ISS as well as on ground.

4.1.1 Characteristics of the temperature/time profile

The first step in the analysis is the examination of the temperature/time profile. An analysis of the brightness of the sample is carried out for this alloy, too.

Fig. 4.1 shows a temperature/time profile for a cycle of the sample processed on the ISS, with a similar course as the one shown in Fig. 3.3. The calibrated temperature is depicted for the entire cycle, whereas the raw data are only shown for the last part of the cycle. From the second camera in the ISS-EML, a frequency distribution of grey values in each frames was calculated. The mean value of the distribution for each frame is calculated and plotted together with the temperature/time profile. The brightness of the sample in the video is governed by the thermal radiation. Hence, temperature changes should lead to changes of the mean value of the grey value frequency distribution.

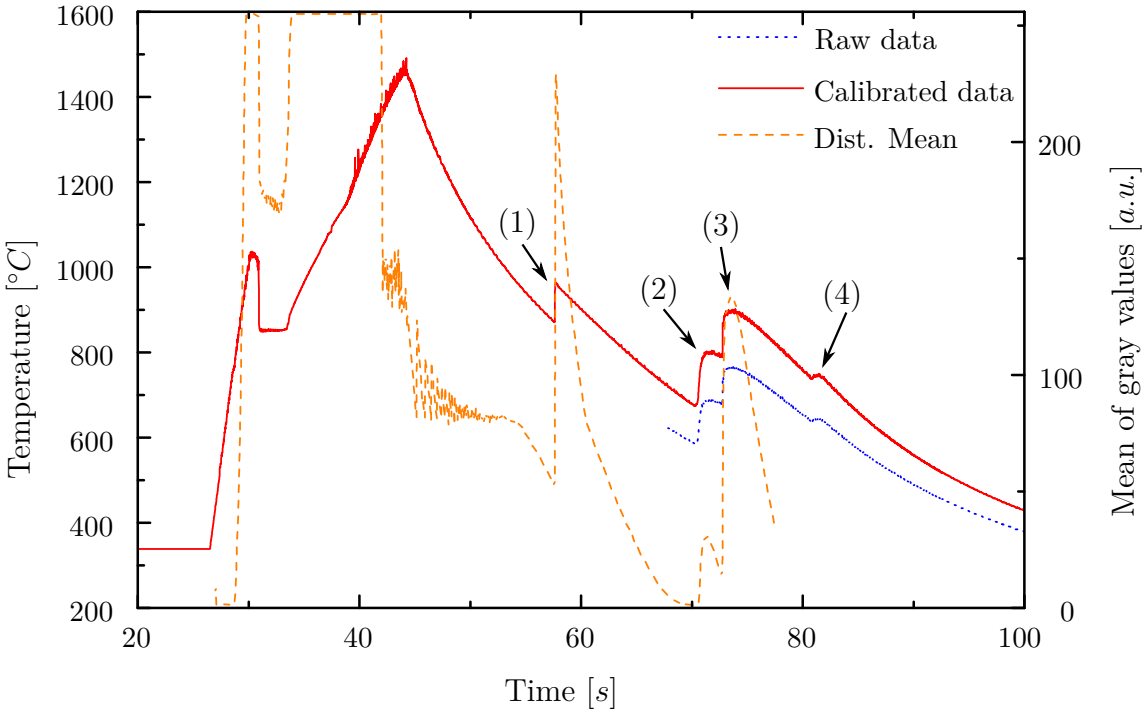

Figure 4.1: Temperature/time profile obtained in microgravity for a sample solidifying at $\Delta T = 282\,\mathrm{K}$ depicting that changes in the temperature (raw, dotted blue line, and calibrated, solid red line, temperature data) lead to changes in the brightness of the sample (mean of relative frequency distribution, dashed orange line).

When the heater is switched off, the sample starts to cool until the first recalescence (1). The released latent heat leads to a temperature increase. According to the phase diagram, during the first recalescence the Al_3Ni_2 phase should solidify.

In Fig. 4.1, the temperature after recalescence is well below the liquidus temperature. The released latent heat is not sufficient to heat the sample to the liquidus temperature. That the temperature does not rise to the liquidus temperature, is usually associated with the hypercooled state where the entire sample solidifies during the first recalescence [1, 13, 66]. The hypercooling limit describes the undercooling at which the whole sample solidifies during the recalescence [1, 13, 66]. At this undercooling, the released latent heat is assumed to be exactly sufficient to heat the sample to the liquidus temperature [1, 13, 66]. However, this requires a congruently melting alloy, a temperature independent specific heat capacity in the undercooled state and adiabatic solidification [1, 13]. The hypercooling is then given by [1]:

$$\Delta T_{\mathrm{hyp}} = \frac{\Delta H_m}{c_p^l}, \tag{4.1}$$

with c_p^l the specific heat capacity of the liquid and ΔH_m the heat of fusion. Using the values $\Delta H_m = 19\,606\,\mathrm{J\,mol^{-1}}$ and $c_p^l = 33.13\,\mathrm{J\,mol^{-1}\,K}$ calculated with the ThermoCalc Software [86] in Ref. [87], the hypercooling limit is calculated as $\Delta T_{\mathrm{hyp}} = 592\,\mathrm{K}$. Undercoolings in this order of magnitude were not achieved in Al-25at.%Ni.

From the undercooling prior to the first recalescence, the solid fraction after the first recalescence can be calculated according to [1, 66]:

$$f_S = \frac{\Delta T}{\Delta T_{\mathrm{hyp}}}. \tag{4.2}$$

The solid fraction for the presented cycle for the observed undercooling of $\Delta T = 282\,\mathrm{K}$ is $f_S = 48\%$. For the highest undercooling, $\Delta T = 352\,\mathrm{K}$, the solid fraction reaches $f_S = 59\%$. Thus, there is always a considerable fraction of the sample that does not solidify.

Upon further cooling, a second and third recalescence were observed, see (2) and (3) in Fig. 4.1. A comparison with the phase diagram, Fig. 2.2, shows that after the solidification of the primary phase, where Al_3Ni_2 forms, a peritectic reaction leading to the formation of Al_3Ni should be observed. The sample is fully solid after the eutectic reaction, denoted by point (4). The temperature of the uncalibrated

blue curve in Fig. 4.1 shows the correct eutectic temperature. Calibration after the oxide evaporation and before the eutectic reaction is necessary because of different emissivities of the melt and the oxides. Because the oxides form after the first recalescence, different calibrations are necessary to cover the entire levitation cycle as each transformation step in Al-Ni alloys requires a different emissivity, too, see also [23, 24, 50]. As only the undercooling prior to the solidification of the primary phase is of interest, only the calibration for the liquidus temperature which is of importance is shown in Fig. 4.1.

The curve showing the mean value of the distribution of grey values for each frame in Fig. 4.1 shows a similar behaviour as the temperature curve. When the temperature reaches its maximum, the brightness shows an irregular behaviour. This is due to an automatic adjustment of the exposure time, where the brightness is too low for shorter exposure times but too bright for longer exposure times. This leads to a constant switching between the two exposure times. When the brightness decreases due to the temperature decrease, this switching of exposure times stops.

At the first recalescence, the brightness increases steeply due to the temperature change, but also steeply decreases again as the sample cools. When the two peaks in the temperature curve at (2) and (3) are observed, the brightness again changes steeply. At (2), the brightness changes only slightly, whereas at (3) it changes distinctly. This can of course be also an influence of an adapted exposure time, yet it correlates well with the temperature/time profile. It is suggested that a reaction takes place, either a transformation which is not fully covered by the phase diagram or a completely different reaction. However, from the available data no conclusive answer can be obtained. The video file stops before the eutectic reaction.

4.1.2 Scaled and spiked front morphologies

The usage of a high-speed camera allows the observation of the solidification front during the recalescence. The high-speed videos captured during the experiments on board the ISS show two different front morphologies. A scaled front morphology was observed mainly, while in some cycles the front had a dendritic morphology. The different morphologies correspond to distinct ranges of undercooling and are described in the following.

Fig. 4.2 show image sequences captured at two different undercoolings of (a) $\Delta T = 179\,\mathrm{K}$ and (b) $\Delta T = 350\,\mathrm{K}$. In the first image sequence in Fig. 4.2 (a), the first solid forms in the upper right part of the sample. It is screened by one of four

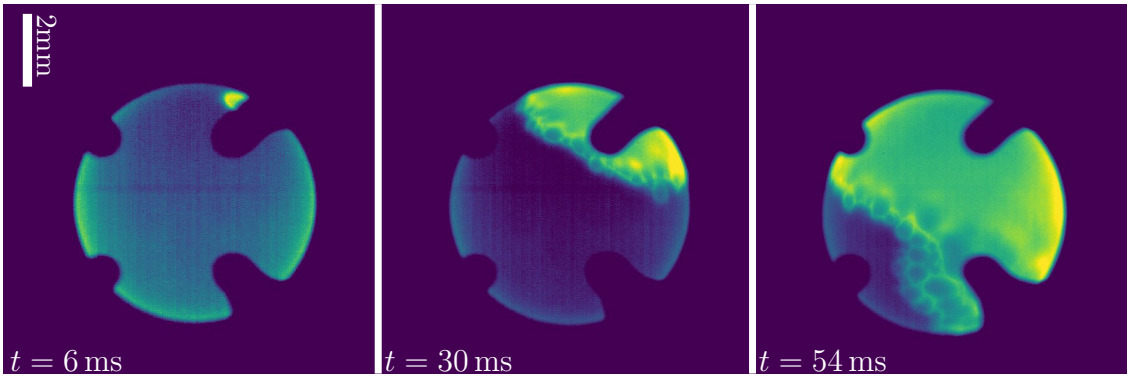

(a) Scaled morphology at $\Delta T = 179\,\mathrm{K}$

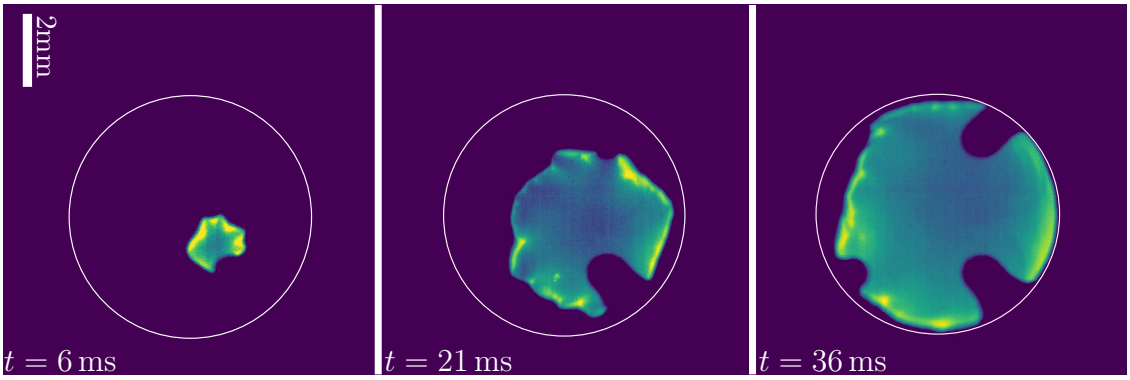

(b) Dendritic morphology at $\Delta T = 350\,\mathrm{K}$

Figure 4.2: Pseudocolour images of two different front morphologies captured at 1000 fps: Fig. 4.2 (a) "scales" (spherical features with an approximate diameter of $d \approx 700\,\mu\mathrm{m}$) at an undercooling of $\Delta T = 179\,\mathrm{K}$, and Fig. 4.2 (b) with a dendritic growth front at $\Delta T = 350\,\mathrm{K}$.

dark fingers. These are shadows of the cylindrical sample holder which has a hole within, shaped like a four-leaf clover. The solid appears in bright yellow, because it is hotter than the surrounding liquid. The high-speed camera works in the range of visible light and captures grey-scale images. The intensity at each pixel represents the temperature which, however, cannot be directly attributed to a temperature value. To improve the contrast, the images are displayed as pseudocolour images, mapping white to yellow and black to blue.

As the front propagates along the sample surface during the solidification in Fig. 4.2 (a), circular features can be observed. These circular features show a bright outline enclosing a darker area. This is the most often observed front morphology in Al-25at.%Ni that is referred to as "scales" [72, 88]. It is observed for undercoolings of $\Delta T < 300\,\mathrm{K}$. New scales do not appear stochastically distributed over the sample surface, but always close to the previously existing solid.

Fig. 4.3 shows cropped frames from the image sequence in Fig. 4.2 (a) with a higher time resolution showing a more detailed view of the scale formation and growth. The red dashed circular segment shows the solidification front position in the first frame at $t = 28\,\mathrm{ms}$. In the following frames, the initial front position is shown, too, but corrected for the small motion of the sample. The scale marked with the white arrow forms close to the solidification front in the first frame. The white arrow follows the scale in each frame and denotes approximately the scale centre. The solid white line connects the highest point of the scale in the first four frames. As the motion of the top of the scale slows down in the last two frames, the slope of the white line would change and it is thus not continued in the these frames. As the scale grows, it is not fixed at one point on the sample surface but is shifted slightly downwards. Otherwise either the topmost point of the scale or the scale centre would be observed at the same position on the sample surface, and the scale would grow asymmetrically due to the other scales blocking the growth. At $t = 34\,\mathrm{ms}$ further scales form in the vicinity of the marked scale which are more apparent in the following frame at $t = 36\,\mathrm{ms}$. The new scales are denoted by the magenta arrows. At $t = 36\,\mathrm{ms}$, another scale forms at the junction of the magenta marked scales. This is better visible at $t = 38\,\mathrm{ms}$ and indicated by the three magenta lines. The cyan arrow in the last frame denotes one case where a scale forms at the junction of three scales. However, scales forming in the vicinity of the front and at the junction of two other scales are more frequently observed. Since the motion of the white scale is due to the growth of itself, but also of adjacent

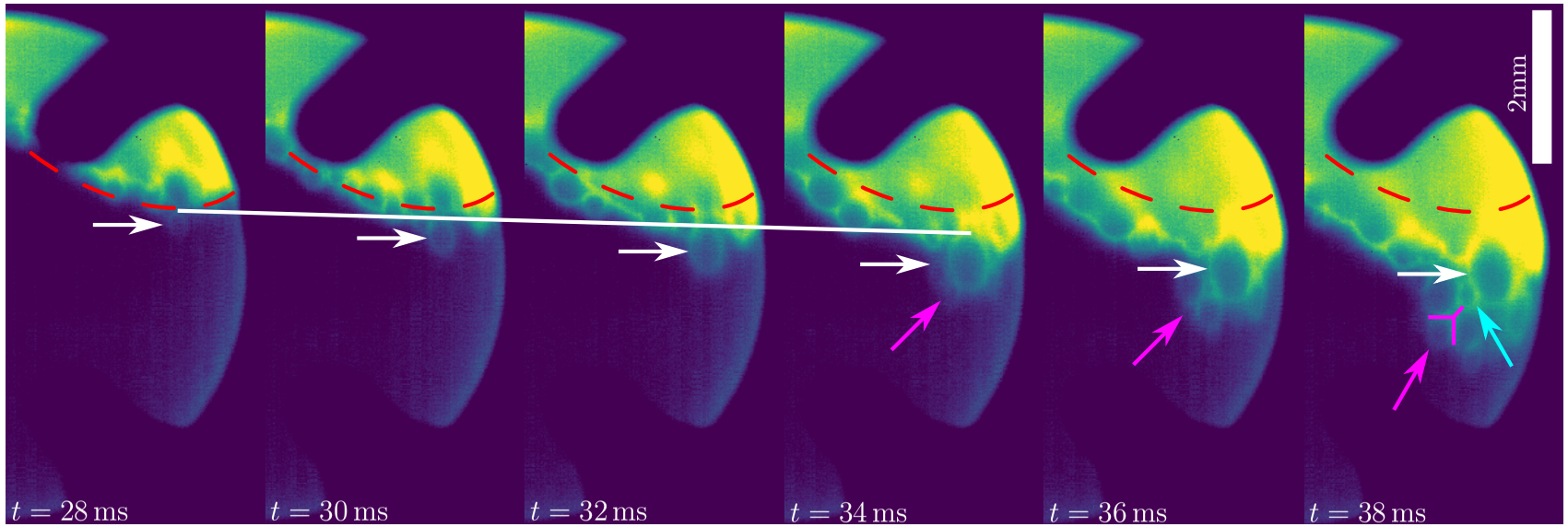

Figure 4.3: Cropped frames from the sequence in Fig. 4.2 (a). The scale marked by the white arrow is not fixed at one position (increasing distance between scale and front position at the time the scale formed, dashed red line). New scales forming close to the shifted scale, magenta and cyan arrows.

scales, this leads to a superposition of two contributions to the migration of the solidification front: growth (as motion of scales is due to the growth of adjacent scales) and formation of new scales.

On the ISS, undercoolings of up to $\Delta T = 350\,\mathrm{K}$ were achieved. At undercoolings of $\Delta T \geq 300\,\mathrm{K}$, the growth front behaves differently. The image sequence in Fig. 4.2 (b) shows the first solid close to the visible centre of the sample surface in the frame. The solidification front consists of "spikes" which resemble dendrite envelopes. Hence, it is called dendritic front morphology.

On earth, one experimental cycle with an undercooling of $\Delta T = 347\,\mathrm{K}$ was observed where the front morphology was planar. This is a difference to the front morphology observed in μg. However, as the solid appeared darker than the melt with only a frail contrast difference, this observation cannot be verified. The respective front velocity is included in Fig. 4.5, but is not used for discussion.

4.1.3 Velocity-vs.-undercooling relationship

Besides the front morphologies, the dendrite growth velocity can be determined from the high-speed video data. Several techniques are available, see Refs. [89, 90] and references therein. Before describing the results of the velocity analysis, a description of the analysis method is necessary.

In the present work, the velocity determination was done frame by frame using the videos from the high-speed camera. The method described in the following is based on the one used by Karrasch [91], who used the software *ftt* [92] developed at the Institute of Materials Physics in Space, DLR Cologne, as well as on Assadi et al. [93].

As only the surface of the sample and the solidification front on this surface are visible, some assumptions about the growing solid inside the sample need to be made. Observations on levitated Al-Ni samples by Assadi et al. [93] showed that the solidification front visible on the sample surface is the intersection of two spheres. One sphere represents the sample outline. The other sphere is assumed to represent the outline enclosing the growing dendrites [93]. Fig. 4.4 depicts the assumptions made by Assadi et al. and used here. A cut through the geometrical center of the sample is shown and not the surface.

In Fig. 4.4, the nucleation is assumed to occur on the right side of the sample surface, black circle. Shown are the spheres denoting the position of the outline of the dendrite tips at different time steps, similar to [89, 93]. The different time

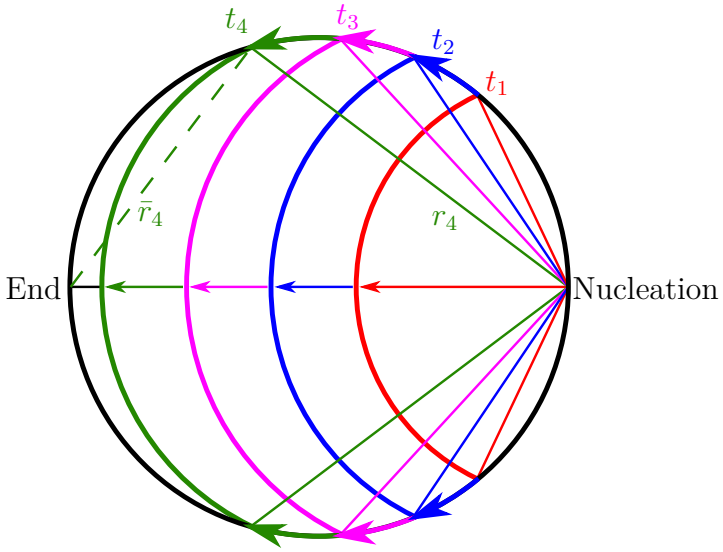

Figure 4.4: Spherical solid growing in a spherical drop of undercooled melt where the intersection of the spherical solid with the sample surface is the observed growth front, and allows for a direct determination of the growth velocity.

steps are denoted by different colours, and the increasing radius is described by the stacked arrows along the diametre pointing to the left. The visible growth front on the surface is described by the intersection of the "solid" sphere and the sphere describing the sample outline, see [93]. When the visible front moves across the sample surface (coloured arrows on the surface), its velocity is not equal to the velocity of the solidification front [93]. The spherical outline of the foremost solid, visible on the surface, is used to calculate the radius at each time step. The radius is extracted by calculating the 3-dimensional distance between the front position on the surface and the nucleation point on the surface.

In cases where the front outline is not exactly described by a circle on the sample surface, a distinct front feature, e.g. a dendrite tip which is visible throughout the entire video, is selected and tracked.

If the solidification starts at a point outside of the field of view, only the end of solidification is visible. Therefore, the measured radii need to be corrected. Fig. 4.4 shows a dashed green line, $\bar{r}_4$ which connects the end point of solidification with the position at time t_4. The actual radius r_4 can then be calculated using simple geometric considerations (Thales's and Pythagorean theorems). However, this can lead to errors in the calculated velocity as the end of solidification also shows a final transient [71] where the velocity can be altered due to the changing conditions, e.g.

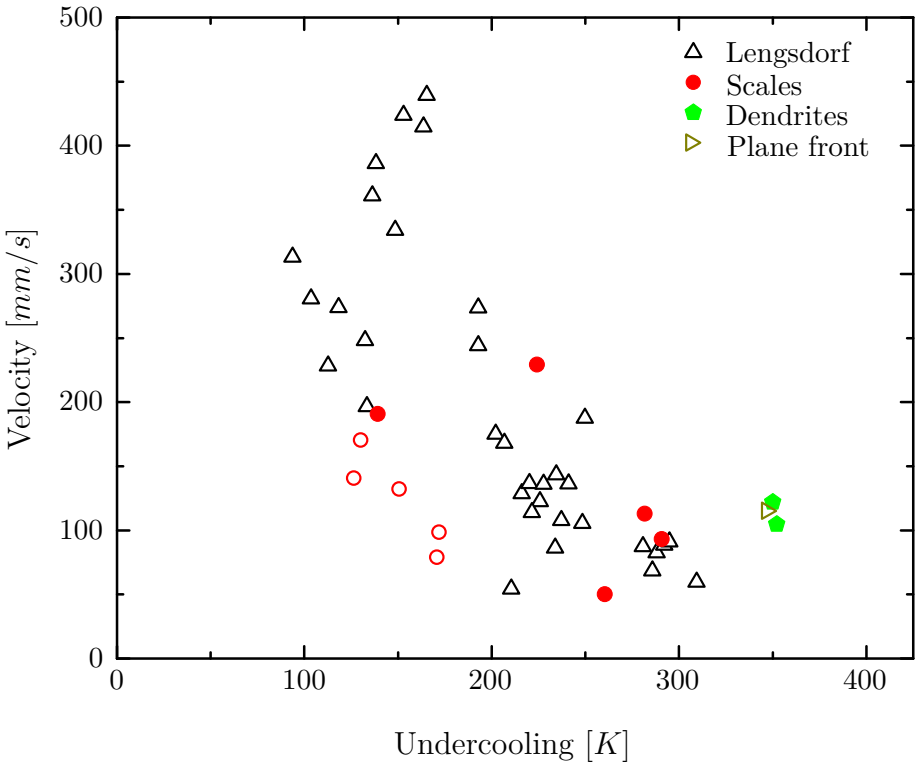

Figure 4.5: Growth velocity in an Al-25at.%Ni alloy measured on ground by Lengsdorf et al. [5] and on board the ISS in the present work with different markers for the observed front morphologies: red circles for scaled and green diamonds for dendritic morphologies [88]; empty markers depicting data obtained on earth, filled obtained in microgravity.

a heating of the remaining liquid.

After the determination of the radius, t velocity is calculated as the slope of the radius over time [89,91,92]. A more detailed description of how to extract positions from the videos and the calculation of different information is given in the following section, see Subsection 4.1.4.

The results of this analysis are shown in Fig. 4.5. The different front morphologies, described in the previous section Subsection 4.1.2, are indicated by different markers: red dots for the scaled morphology, and green diamonds for the dendritic morphology. Results from Ref. [5] are shown by empty black triangles. The new data points from microgravity, filled markers, essentially reproduce the old data. The data obtained on earth, empty red dots, also show the negative slope of the growth curve. The new terrestrial data are slightly below the literature data as they are obtained using the correction for the end of solidification. The data point for the highest undercooling measured on earth showed a plane front. The

achieved undercooling is close to the highest ones observed in space. Referring to Subsection 4.1.2, the data point recorded at the highest undercooling on earth is disregarded in the further analysis.

The range of undercoolings on the ISS is increased by $\sim 50\,\mathrm{K}$ to $\Delta T \approx 350\,\mathrm{K}$ compared to the data in literature. The new data points around the highest undercooling are of the same order of magnitude as the data at the undercooling $\Delta T \approx 300\,\mathrm{K}$. A sharp transition from the scaled to the dendritic morphology is visible in the new data. Scales appear for undercoolings below $\Delta T < 300\,\mathrm{K}$, whereas dendrites are observed at higher undercoolings.

4.1.4 Analysis of the distance between scales

As the dominant front morphology for undercoolings below $\Delta T < 300\,\mathrm{K}$ is the scaled morphology, an analysis of the scales in terms of number, their size and the distance between scale centres to their nearest neighbours was carried out. In order to extract these information, an analysis method was developed relying on three steps: 1) selection of the scales, 2) application of a Delaunay triangulation to find the nearest neighbours and the respective scale distance, and 3) calculation of the scale distribution function and finding the most frequent scale distance. Fig. 4.6 illustrates the different steps of the analysis. The results show a clear dependence of the number of scales, the mean scale radius and the scale distance on the undercooling, see Fig. 4.7.

Selection of scales

The extraction of scale positions is carried out manually, and is based on the analysis software, ftt, developed at the Institute of Materials Physics in Space, DLR Cologne [91, 92].

First, the sample outline is marked, large green circle in Fig. 4.6 (a). The sample center (x_0, y_0) is marked by a small green circle. The sample outline has to be adjusted in every frame to correct for sample drift. The outline is also used for calibration of the video data [91, 92]. The sample diameter is known, and the spatial extension of each pixel can be calculated. The sample in the analysis shown in Fig. 4.2 has a diameter of $2 \cdot r_0 = 6.5\,\mathrm{mm}$, and the corresponding calibration factor is $f \approx 0.017\,\mathrm{mm/pixel}$.

Similar to the marking of a single solid in Refs. [91, 92], each scale is marked like

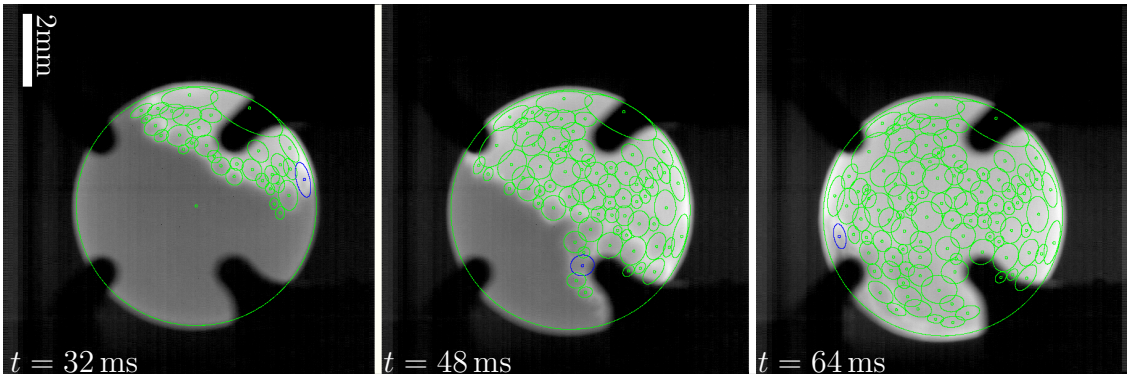

(a) Manually mark scales

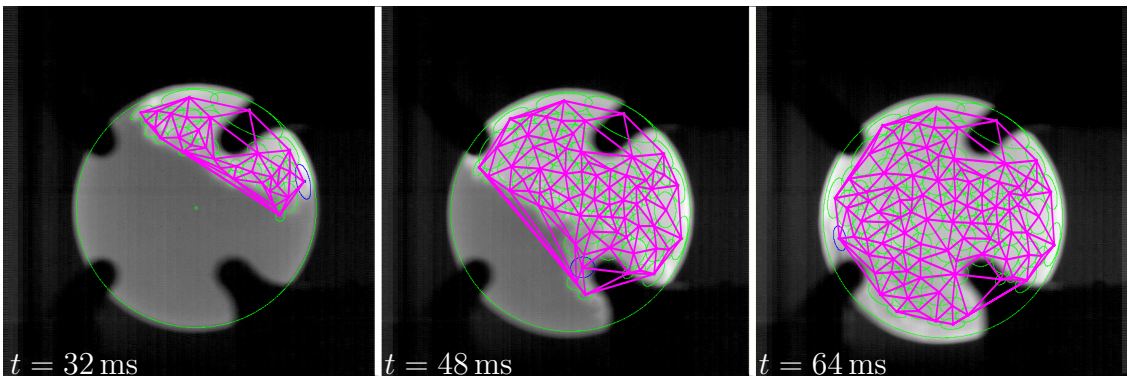

(b) Determination of nearest neighbours via Delaunay triangulation

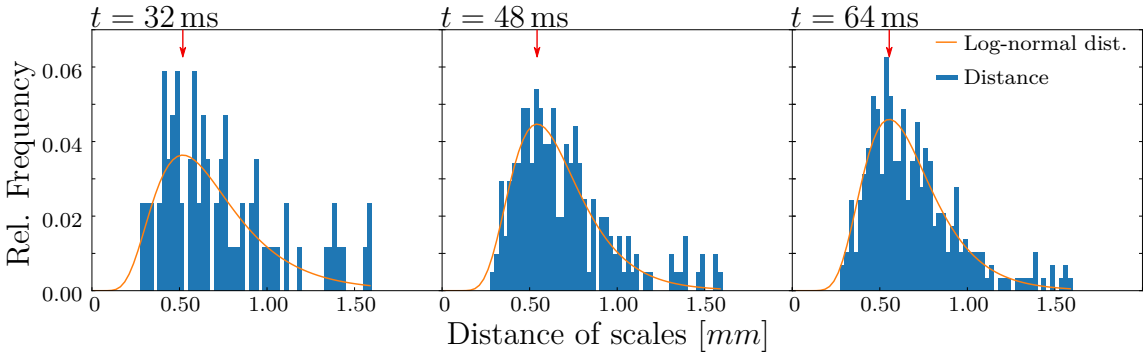

(c) Scale distance distribution function

Figure 4.6: Number and size of scales and distance to nearest neighbours is determined in a three step procedure: (a) marking of each scale throughout the whole image sequence manually; (b) applying Delaunay triangulation to find adjacent scales; (c) sorting the distances between adjacent scales into a histogram (bin size 0.025 mm and cut-off at $d = 1.6$ mm), fitting a log-normal distribution and determining the peak position.

the sample outline by a green circle. The currently selected scale is highlighted by a blue circle. The scale outlines are adjusted to the position on the sample surface to correct for the projection from a sphere onto the 2D sensor plane of the camera [92]. The sensor plane onto which the sample surface is projected is defined as the x-y-plane of the coordinate system. The z-axis is thus perpendicular to the image plane. The position of a scale (marked by a small green or blue circle) in the image plane (x, y) is calculated relatively to the sample center [92]. Due to the spherical geometry, the z-component is calculated by:

$$z = \sqrt{r_0^2 - (x - x_0)^2 - (y - y_0)^2}. \tag{4.3}$$

The position of a scale centre on the sample surface is now given in a Cartesian coordinate system. The position is transformed into spherical coordinates according to basic geometrical considerations:

$$\text{Azimuthal angle} \quad \theta = \arccos\left(\frac{x - x_0}{\sqrt{(x - x_0)^2 + (y - y_0)^2}}\right), \tag{4.4}$$

$$\text{Polar angle} \quad \phi = \arccos\left(\frac{z}{r_0}\right). \tag{4.5}$$

The azimuthal angle is calculated in the projected sample surface plane (x-y-plane). The shifted x-coordinate relative to the sample center is, hence, divided by the absolute distance between itself and the sample centre in the x-y-plane, whereby the latitude (z-coordinate) has no influence. The polar angle uses the z-coordinate divided by the sample radius, as the scale is located on the sample surface.

Each scale outline has a circular shape. In the following it is thus assumed that each scale is a representation of a spherical solid growing into the undercooled melt (similar to the velocity analysis in Refs. [89, 91, 92]) to apply the same equations for the calculation of the radius of the scales as for the velocity measurement. Each scale outline is thus an intersection of the isotropically growing solid with the sample surface, c.f. [89, 92, 93]. To obtain the position and radius of any scale, the scale centre and the scale outline need to be adjusted to the position and shape of the respective scale. Let $(x\prime, y\prime, z\prime)$ be an arbitrary point on the scale outline. The scale centre at (x, y, z) is known, and the distance between these two can be calculated using:

$$r_{\text{new}} = \sqrt{(x\prime - x)^2 + (x\prime - y)^2 + (z\prime - z)^2}. \tag{4.6}$$

This is assumed to be the radius of a scale.

The sample holder shadows parts of the sample surface. This leads to an error in terms of the number of the scales. The number of scales given here is therefore expected to be smaller than the true number of scales on the visible hemisphere.

Delaunay triangulation and calculation of distances

In the first step data were acquired with spherical coordinates and radii of each scale for each frame. A Delaunay triangulation is used to find the nearest neighbours of each scale. The evolution of this network is shown in Fig. 4.6 (b).

The Delaunay triangulation connects scales with their neighbours by filling the area with non-overlapping triangles. For the triangulation, the scale centre positions in the x-y-plane of the sensor were used. The triangulation returns a list of the vertices and neighbours.

As solidification proceeds, more scales form and contribute to the network of scales. However, the shadows from the sample holder introduce a certain error in the method as scales behind the shadows are concealed. Therefore, scales on the opposite side of a shadow can be erroneously identified as neighbours. At the solidification front and on the outline of the scale network, erroneous identifications of neighbours are found which are visible as long lines in the frames at $t = 48\,\mathrm{ms}$ and $t = 64\,\mathrm{ms}$. This artefact of the video analysis and the Delaunay triangulation is handled in the next step of the analysis.

To obtain the distance between the centre of each scale and one of its neighbours, the equation for great-circle distances on a sphere is applied:

$$d = r_0 \cdot \arccos\left(\sin\left(\theta_1\right)\sin\left(\theta_2\right) + \cos\left(\theta_1\right)\cos\left(\theta_2\right)\cos\left(\phi_2 - \phi_1\right)\right). \tag{4.7}$$

The indexes denote the two scales.

Histogram and fit

For finding the most frequent scale distance at one frame, the distances of scale centres were calculated and sorted into a histogram with a bin size of $0.025\,\mathrm{mm}$ to obtain the relative frequency of the scale centre distances. To solve the problem of the erroneous classification of neighbours, a cut-off was used at $d \geq 1.6\,\mathrm{mm}$. Not using a cut-off would shift the distribution to larger values. Although there may be some lines which are correct and longer than the cut-off, this is assumed to be of

a smaller influence on the distribution than the usage of the wrong lines. Different cut-off parameters were tested, and for $d \geq 1.6\,\mathrm{mm}$ the best results were achieved.

Fig. 4.6 (c) shows the relative frequency of the scale centre distances. The histogram gradually fills as new nuclei appear. The first histogram in the sequence is still sparsely filled after $t = 32\,\mathrm{ms}$ as 32 scales with 89 scale distances were measured. When solidification proceeds, more scales appear, and more scale distances are defined. At $t = 48\,\mathrm{ms}$ already 204 scale distances of 72 scales were analysed for the relative frequency. For the last histogram, 101 scales were analysed yielding 287 scale distances. The relative frequency develops a distinct peak with a tail at the right side (larger distances, i.e. positive skew). The last histogram shows the result for the last frame of the high-speed video.

In order to characterise the evolution of the scale distances throughout the entire video, a distribution is fitted to the histogram. Calculating the average distance would also be a possible way. However, the right tail would falsify the average value. Therefore, a log-normal distribution is chosen, and the maximum of the distribution is set as the characteristic value.

Fig. 4.6 (c) shows the fitted log-normal distributions for three time steps. Regarding the sparsely filled histograms at the beginning of the video the fitting method does not always converge to a plausible value. This may lead to erroneous values, and the results are therefore disregarded. The relative frequency is well represented by the log-normal distribution at longer solidification times.

Measured scale distances

The analysis method mentioned above was applied to three cycles. It provides the number of the scales, the mean radius, and the peak of the scale distance distribution. The time scale in Fig. 4.7 was set to $t = 0\,\mathrm{ms}$ for the first frame with more than one scale. The video for the initial undercooling of $\Delta T = 261\,\mathrm{K}$ only shows the end of the solidification process. This aggravates the analysis, and the result is interpreted with caution.

The number of scales shows a linear increase in all three cycles with time. At the medium undercooling, $\Delta T = 282\,\mathrm{K}$, the curve remains at low values in the beginning, but shows a steep increase after $t \approx 10\,\mathrm{ms}$. For the undercoolings of $\Delta T = 261\,\mathrm{K}$ and $\Delta T = 291\,\mathrm{K}$ the curves show a linear increase right from the beginning of solidification. The curve for $\Delta T = 261\,\mathrm{K}$ shows a plateau after $t \approx 18\,\mathrm{ms}$. Disregarding the result for the video that only shows the end of solidification,

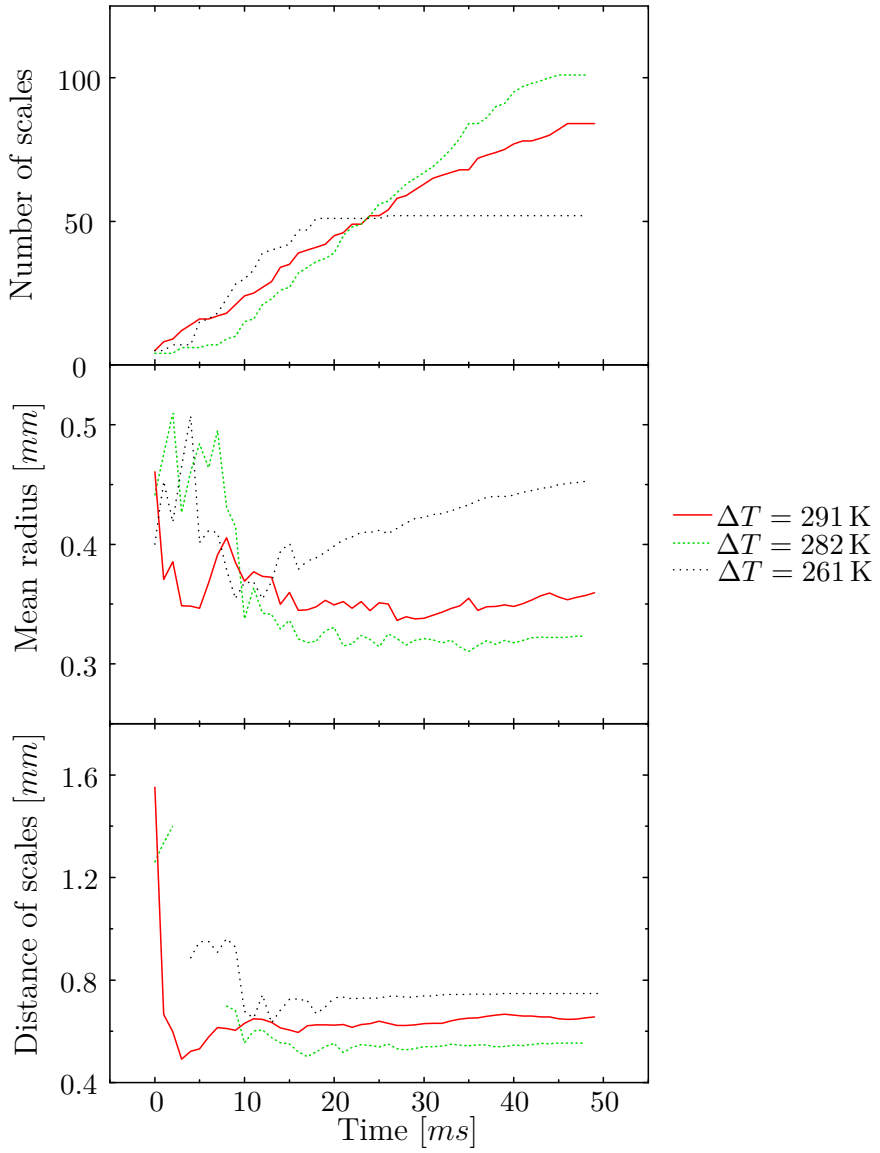

Figure 4.7: Results from the experiments in microgravity: number of scales increasing linearly, mean scale radius and scale distance showing initial transient before reaching a constant value.

the slope, i.e. the number of nuclei forming per time unit, decreases for larger undercoolings. Hence, the nucleation rate decreases with increasing undercooling.

The mean radius shows larger values in the beginning. Because of the small number of scales, there is not sufficient statistical validation, and a few large scales can distinctly change the mean radius. After $t \approx 10\,\mathrm{ms}$, the mean radius drops to a nearly constant value. At the lowest undercooling, the number of scales shows a plateau. This is accompanied by an increase of the mean radius of the scales. The existing scales seem to grow, but no new nuclei form. Yet, an overall trend becomes visible: the higher the undercooling is, the larger becomes the mean radius.

Similar to the evolution of the mean radius up to $t \approx 10\,\mathrm{ms}$, the scale distance shows strongly deviating curves. The two curves for $\Delta T = 282\,\mathrm{K}$ and $\Delta T = 291\,\mathrm{K}$ show large values of the scale distance for the first $\sim 2\,\mathrm{ms}$. During these cycles one large scale grew until new scales formed. Hence, the distance between the scale centres of the new scales and the previously existing scale is strongly influenced by the radius of the first scale. For the curves representing the undercoolings of $\Delta T = 261\,\mathrm{K}$ and $\Delta T = 282\,\mathrm{K}$ some data are missing due to bad convergence of the fitting routine, and curves are left blank. After $t \approx 10\,\mathrm{ms}$, the fitting routine was able to provide stable data. The curves show a drop of the scale distances to nearly constant values. As for the mean radius, a trend can be found showing larger scale distances with increasing undercooling.

4.1.5 Tomographic analysis of undercooled samples

For non-destructive analysis of the microstructure, tomography was used. As no microstructure of a sample solidified in microgravity is currently available, a sample solidified under terrestrial conditions was selected for tomographic analysis. The sample solidified at an undercooling of $\Delta T = 137\,\mathrm{K}$ with the scaled morphology. The microstructure of this sample is shown in the next section, see Subsection 4.1.6.

The tomography reconstructs outline and microstructure of the sample three-dimensionally, see Fig. 4.8. The sample is surrounded by a grey "dust" (Fig. 4.8 (a)) which stems from the mounting resin. The sample is nearly spherical and shows two different microstructural features on the surface. On the right hand side of the surface, circular features are visible. These resemble small dendritic structures that emerge from a single point. Their distribution looks arbitrary. However, to the left of the equator, a belt is visible which is again divided into a shining metallic part to the right and a dull one to the left. Inside this belt no distinct circular features

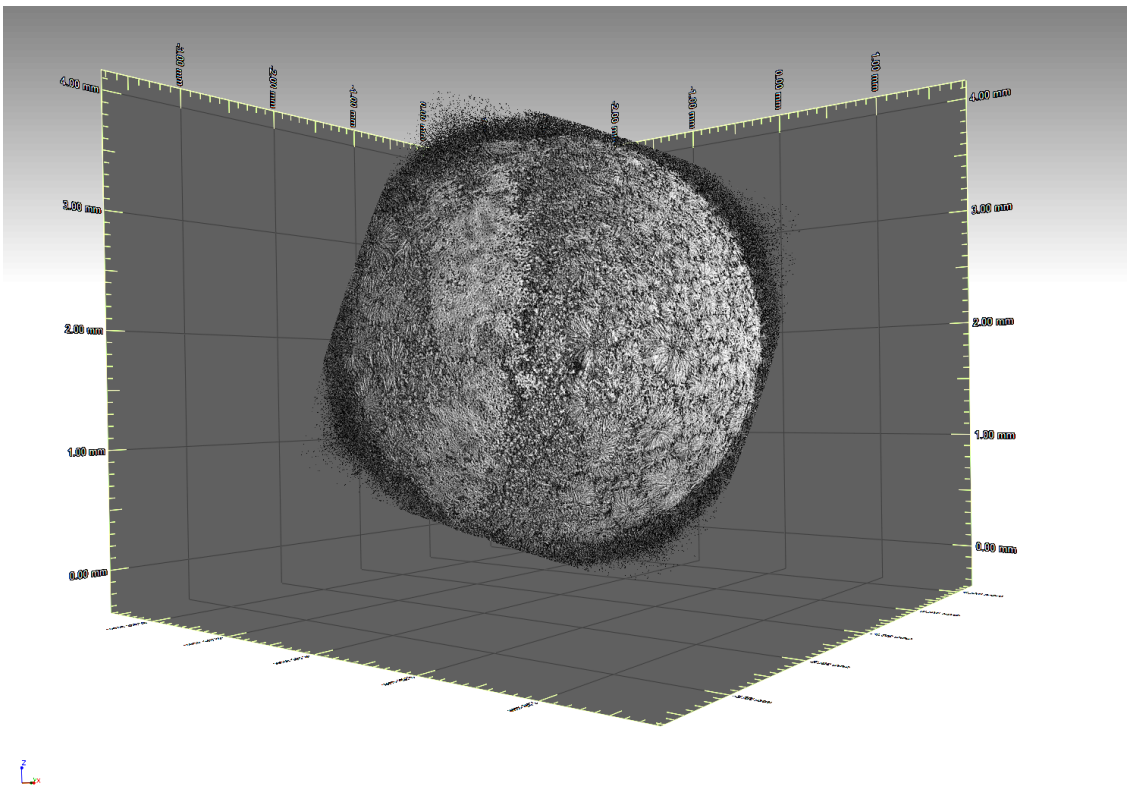

(a) Reconstructed sample surface with circular features distributed over the whole sample surface.

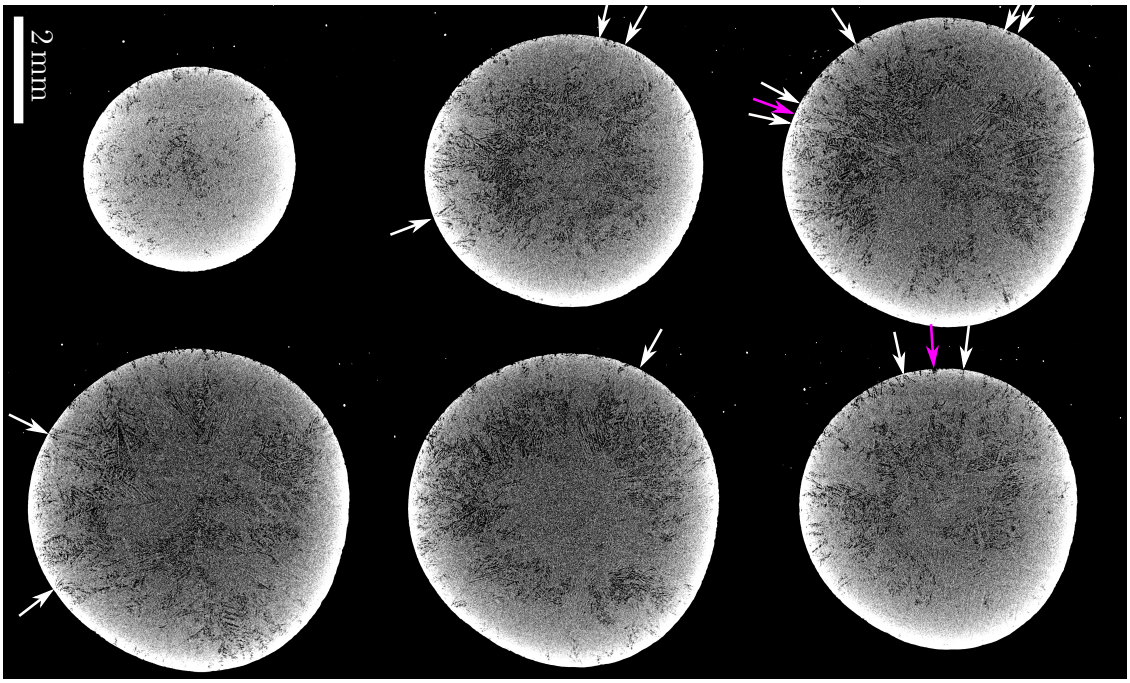

(b) Sections through the sample with inwards growing dendrites; closer to the surface, a finer structure with less prominent features is visible.

Figure 4.8: Tomography results for a sample solidified at $\Delta T = 137\,\mathrm{K}$ under terrestrial conditions showing dendrites pointing towards the sample centre and a region of finer structure close to the surface.

are visible. This is a feature some samples processed by means of EML show.

By virtually cutting the sample at different heights, images like in Fig. 4.8 (b) can be obtained. When going from the upper left to the lower right image, the sequence moves through the sample. Shortly beneath the surface, no very distinct features except large black areas are visible. These black areas can either be shrinkage pores or consist of chemical elements with lower atomic order number as e.g. in the Al-rich eutectic. Inside the sample, dendritic structures are visible which point radially inwards. Their origin can be tracked to several locations on the sample surface. From each of these locations, from which some are highlighted with white arrows, dendrite arms emerge. The dendrite arms coming from one point on the surface show an almost isotropic growth direction. However, shortly beneath the surface, dendrites with a strong deviation from the radial direction encounter dendrites from adjacent surface points, and stop growing (marked by magenta arrows). Therefore, only dendrites are selected that grow close to the radial direction. This is better pronounced in the microstructure images in the following Subsection 4.1.6.

4.1.6 Microstructure of samples processed under terrestrial conditions

In the previous sections, the analysis mostly covered the properties of the scales. To correlate the front morphologies to microstructures, three different undercoolings were chosen: $\Delta T = 15\,\mathrm{K}$, $137\,\mathrm{K}$ and $347\,\mathrm{K}$.

The results for the lowest undercooling are shown in Fig. 4.9. The microstructure in Fig. 4.9 (a) shows dendrites with various crystallographic orientations. The bright interior of the dendrites is identified as Al_3Ni_2. The dark grey shell around the dendrite centres is the Al_3Ni phase.

Electron-backscatter diffraction (EBSD) was used to characterise crystal structure and orientation. The result for the Al_3Ni_2 phase in Fig. 4.9 (b) shows large grains of various orientation. For a small number of dendrites, the size of the Al_3Ni_2 region was determined using the EBSD result ranging from $d = 164$ to $523\,\mu\mathrm{m}$.

The results for the sample solidified at $\Delta T = 137\,\mathrm{K}$ are displayed in Fig. 4.10, Fig. 4.11 and Fig. 4.12. The sample showed the scaled morphology. No velocity analysis was carried out due to the nucleation outside the field of view and oxides on the sample surface which alter the growth into different directions and distort the normally nearly circular front. Fig. 4.10 shows a typical circular feature with

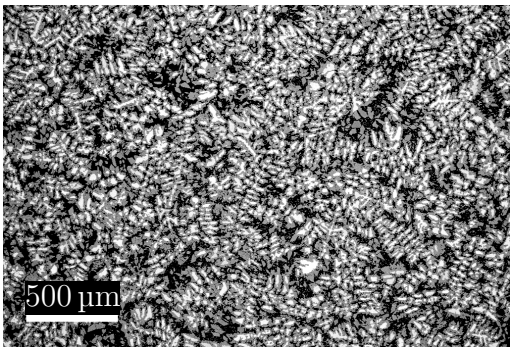

(a) Backscatter diffraction image showing bright dendrite cores surrounded by a darker peritectic phase.

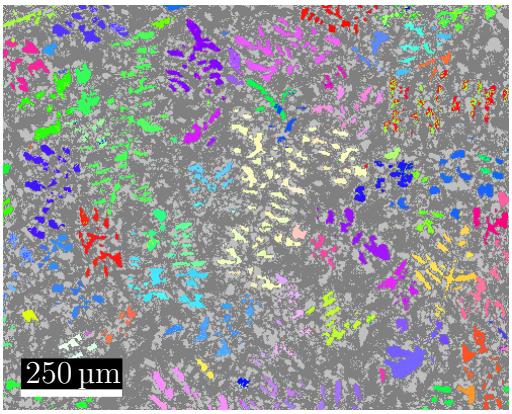

(b) Electron backscatter-diffraction depicting various crystallographic orientations of large dendrites.

Figure 4.9: Microstructures for the lowest undercooling, $\Delta T = 15\,\mathrm{K}$, showing large grains with arbitrary crystallographic orientations.

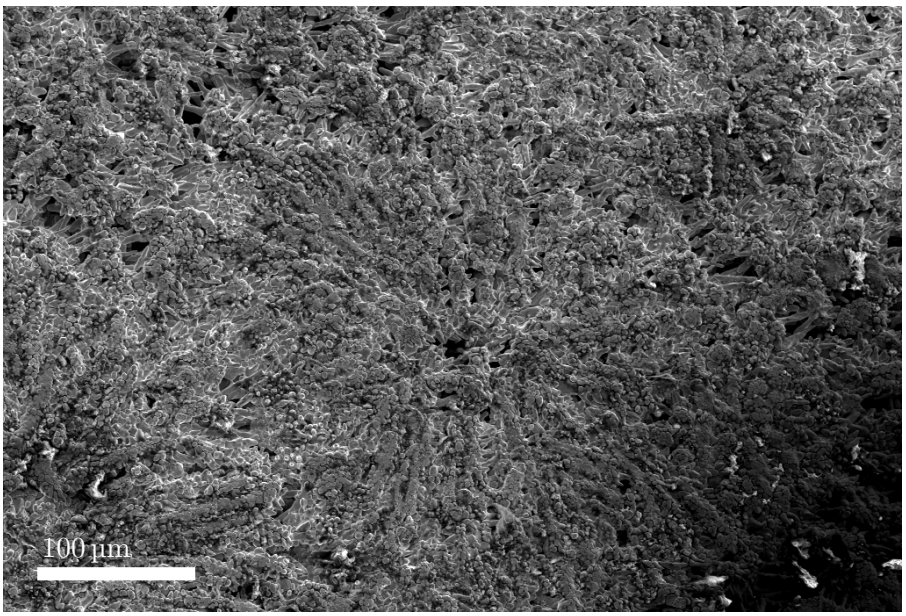

Figure 4.10: Exemplary surface feature which is found all over the surface of the sample solidified at an undercooling of $\Delta T = 137\,\mathrm{K}$.

higher resolution which has already been introduced in Fig. 4.8 (a). This feature has a diameter of $d \approx 300\,\mu m$. In the centre, a hole is visible. From this hole, dendrite arm-like features grow along the surface in numerous, apparently arbitrary directions.

For microstructure analysis, two different sections were analysed, see Fig. 4.11. For the first section, shown in Fig. 4.11 (a) and Fig. 4.11 (b), the sample is cut through the geometrical centre. The microstructure shows long dendritic structures pointing radially inwards, marked by red arrows. These long dendrites are emerging from a layer beneath the sample surface. Going away from the surface, the long dendrites develop side branches.

At a higher magnification, Fig. 4.11 (b), the dendritic structures starting from a single location on the sample surface become visible. In this case, two starting points can be identified on the sample surface, as indicated by white arrows. The distance between these locations is $d \approx 460\,\mu m$. Close to the sample surface, various growth directions of the dendrite arms emerging from one starting point are visible. The dendrite arms with a strong deviation from the radial direction encounter dendrite arms from adjacent starting points, and their growth is thus stopped. Therefore, the number of dendrite arms originating from a single spot reaching further into the sample centre is reduced. This selection only allows dendrite arms with a small deviation from the radial direction to grow into the sample centre. The other dendrite arms are overgrown and stopped. This area of orientation selection beneath the surface is found around the entire sample. Between the stopped dendrites, shrinkage pores have formed, marked by the magenta arrow. These were already visible in the tomographic analysis, see Fig. 4.8 (b).

A section which is only a few micrometres below the sample surface is shown in Fig. 4.11 (c). In the upper right corner, the sample outline is located. From that, straight lines, looking again like dendrite arms without side branches point into the sample. These dendrite arms are pointing to a single location on the sample surface. Similar structures with dendrite arms either parallel or tilted relatively to the section are found around the whole outline. Of special interest is the largest area in the shown image. Small points are visible. Together with their dark grey surroundings, these resemble dendrite arms which are cut perpendicular to their growth direction.

EBSD analysis was carried out to study the crystallographic orientations. Fig. 4.12 depicts the results, with the used IPF colouring. The picture in Fig. 4.12 (a) dis-

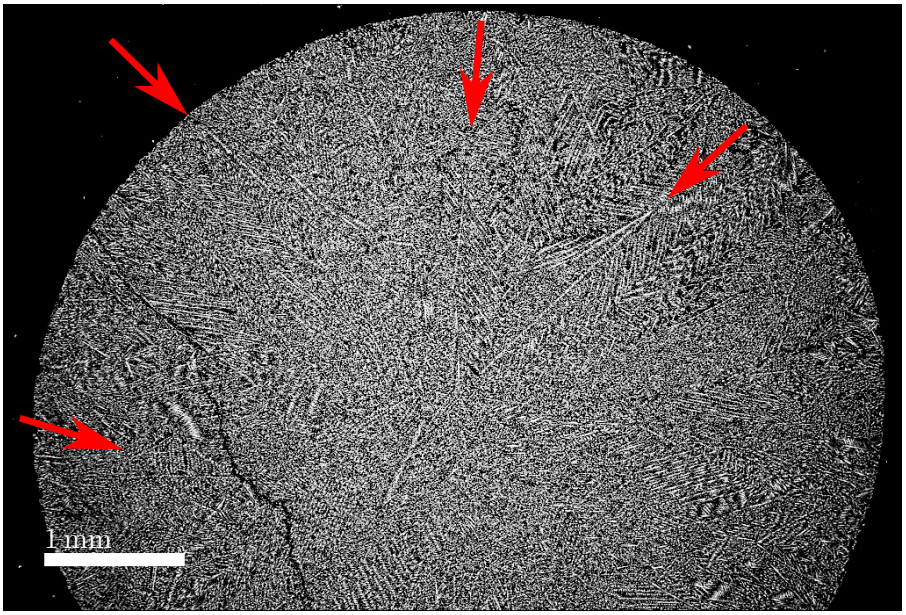

(a) Long dendrites pointing towards the sample centre.

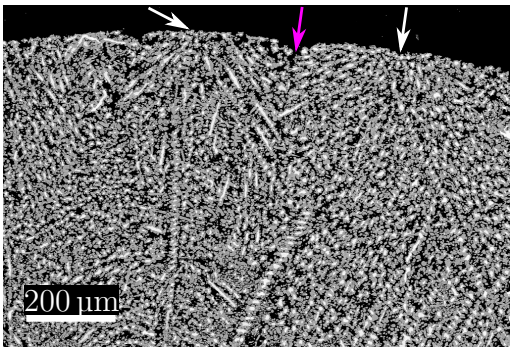

(b) Two locations on the sample surface from which long dendrite arms reach out.

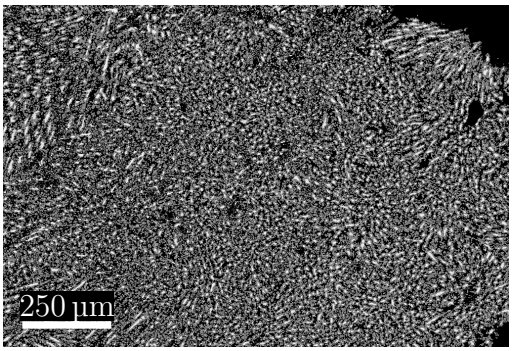

(c) Section directly underneath the sample surface shows a large region with small interios of dendrite arms (white spots).

Figure 4.11: Microstructure images of a sample solidified at $\Delta T = 137\,\mathrm{K}$ showing long dendrite arms with (a) and (b) section parallel and (c) perpendicular to the dendrite arms.

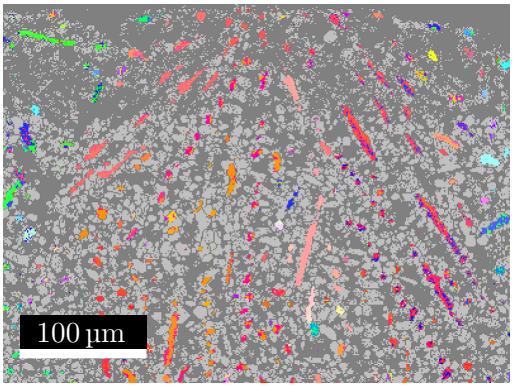

(a) EBSD analysis of the left location in Fig. 4.11 (b) of the dendrite arms showing the same crystallographic orientation belonging to the same dendrite.

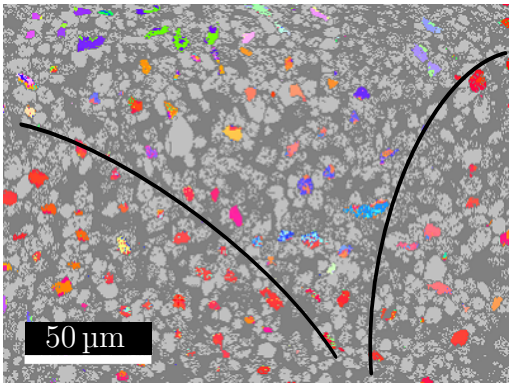

(b) Different areas of similar orientation marked by circular segments

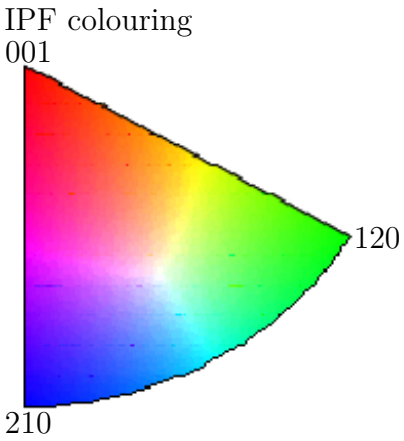

(c) IPF colouring used for Al_3Ni_2 in (a) and (b)

Figure 4.12: EBSD analysis of (a) and (b) in Fig. 4.11, showing dendrite arms growing from the sample surface towards the sample centre with a similar crystallographic orientation for dendrite arms which therefore belong to one dendrite coming from one surface spot.

plays the analysis of the left starting point in Fig. 4.11 (b). As already indicated at the lowest undercooling, the interior of the dendrites is again identified as the Al_3Ni_2 phase. The light grey surroundings are identified as the Al_3Ni phase but are omitted here for clarity and to obtain information about the crystallographic orientation during the primary solidification as the Al_3Ni phase forms by transformation. The distribution of the Al_3Ni_2 phase supports the suggestion that the dendrite arms all emerge from one point on the surface.

In order to support the idea that the dendrite arms emerge from the same location on the surface, an estimation of the angular difference between the crystallographic orientations in the different arms in Fig. 4.12 (a) can be made. This estimation yields a difference of $\Delta\alpha \approx 15°$ by assuming a linear change of the angle between the [001] and the two [210] and [120] directions. This facilitates the suggestion that the different dendrite arms belong to the same dendrite, and therefore to the same starting point on the surface.

The second EBSD analysis in Fig. 4.12 (b) was carried out using the section beneath the sample surface shown in Fig. 4.11 (c). The analysis yielded that the light grey centres visible in the microstructure are the Al_3Ni_2 phase, and the dark grey shell is the Al_3Ni phase. Different areas with similar colouring of the centres can be identified. The areas marked by the black lines belong to two different dendrites as the similar colouring indicates a similar crystallographic orientation. From the image centre to the top, a third area of similar orientation could be located, but the result is not clear enough to obtain a reliable result.

At the largest undercooling of $\Delta T = 347\,\mathrm{K}$, the front morphology was attributed to be planar in the video from the high-speed camera. For a plane front, a microstructure free of segregation is expected. However, the microstructure (Fig. 4.13 and Fig. 4.14) is also dendritic. The image in Fig. 4.13 (a) shows a different surface structure than Fig. 4.10 at the same length scale. The topography is rougher, and no circular features are found on the surface. The bright solid is surrounded by large dark shrinkage holes, marked by red arrows.

A section through the geometrical centre of the sample showed the microstructure in Fig. 4.13 (b) and Fig. 4.13 (c). The microstructure shows dendrites. In Fig. 4.13 (b), the shrinkage holes which were found on the surface are also visible and marked by red arrows. Similar to the previous analyses, dendritic structures emerging from the sample surface and pointing towards the sample centre can be found around the whole sample surface, e.g. also at the positions marked by the red

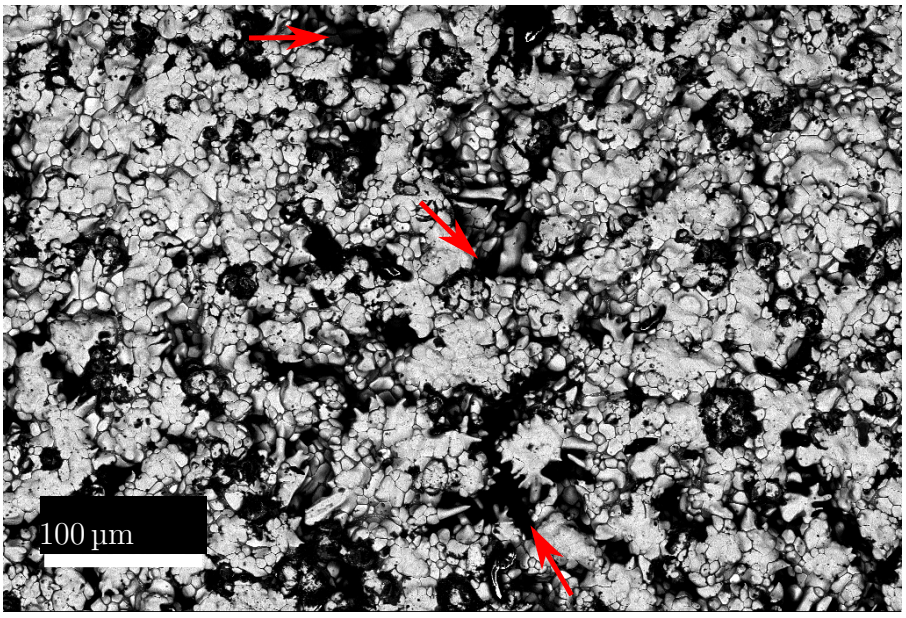

(a) Sample surface with rough topography and shrinkage pores (red arrows).

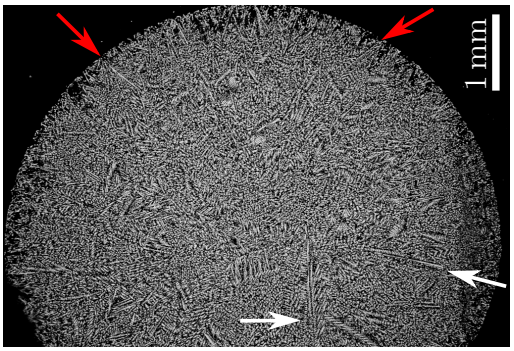

(b) A layer beneath the surface with some long dendrite arms pointing towards the sample centre.

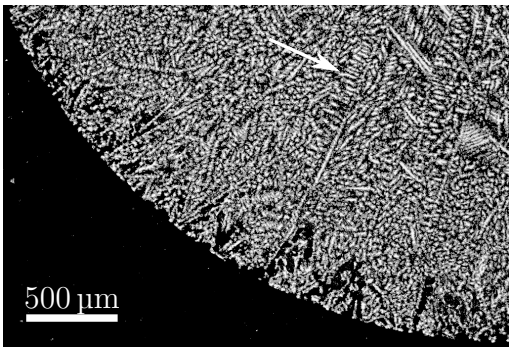

(c) Dendritic structures beneath the sample surface with a long dendrite arm with perpendicular secondary branches.

Figure 4.13: Surface and microstructure of a sample solidified at an undercooling of $\Delta T = 347\,\mathrm{K}$.

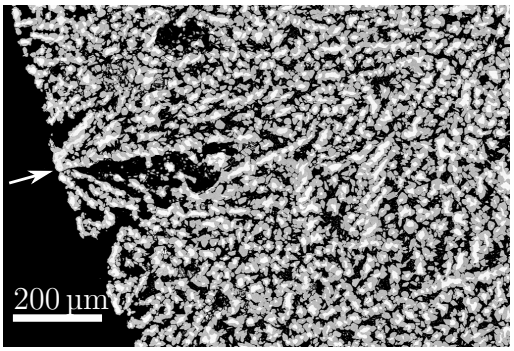

(a) Microstructure image showing the dendrite used for EBSD analysis

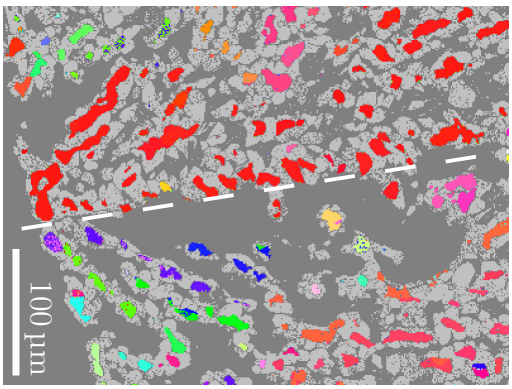

(b) Two different crystallographic orientation of dendrite armss emerging from one point.

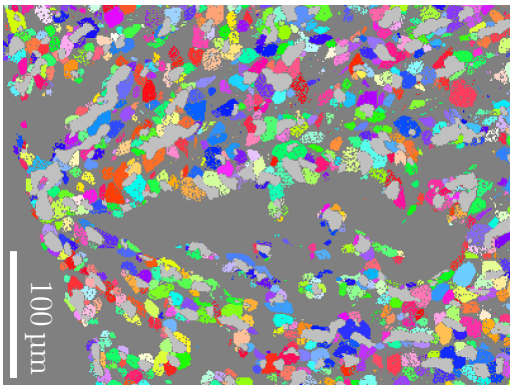

(c) Various crystallographic orientations in the area of the peritectic Al_3Ni phase.

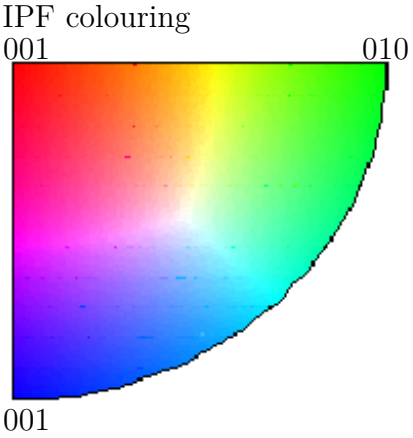

(d) IPF colouring used for Al_3Ni.

Figure 4.14: Dendrite arms (a) extending from the sample surface found in a sample solidified at $\Delta T = 347\,\mathrm{K}$ with similar crystallographic orientations and (b) various crystallographic orientations of the Al_3Ni peritectic phase.

arrows. In this sample, the distance between the locations are approximately $d \approx 540\,\mu m$. Dendrites with various orientations of side branches are distributed inside the sample, white arrows.

At a higher magnification, the numerous starting points on the sample surface can be better identified, see Fig. 4.13 (c). A long dendrite shows secondary branches grown at an angle of 90° from the primary dendrite stem.

Results obtained by EBSD analysis are shown in Fig. 4.14 with an accompanying microstructure image. Fig. 4.14 (b) shows again the results for the Al_3Ni_2 phase showing that the dendrite interior consists of the Al_3Ni_2 phase. The dendrite arms above the white dashed line all exhibit the same crystallographic orientation, indicating that these belong to the same dendrite. Although the dendrite arms below the white line show a different crystallographic orientation, the growth direction of the arms indicates a belonging to the same starting point.

The results for the Al_3Ni phase is shown in Fig. 4.14 (c) with the respective IPF colouring in Fig. 4.14 (d). The Al_3Ni phase surrounds the Al_3Ni_2 phase, as it would be expected according to the phase diagram. The corresponding crystallographic orientations show various orientations.

4.1.7 Discussion

The experiments with Al-25at.%Ni reproduced the solidification anomaly, i.e. the decelerated growth at increasing undercooling. By Ehlen et al. and Paul [71, 72] different reasons for the growth anomaly were put forward: convection, multiple nuclei, no steady-state growth, equiaxed nucleation, influence of vacancies, and nucleation close to the solidification front.

The influence of the absence of a steady-state due to an inhomogeneous temperature distribution can neither be verified or falsified by the present experiments. However, Pericleous et al. [94] simulated the temperature distribution inside a copper sample processed in the ISS-EML. The maximum temperature difference during heating is reported to be $T_{\mathrm{dif}}^{\mathrm{h}} \approx 0.7\,\mathrm{K}$, where the heating and positioning fields are used. During cooling, where the heater is switched off and only the positioning field is used, the temperature difference reduces to $T_{\mathrm{dif}}^{\mathrm{c}} \approx 0.1\,\mathrm{K}$. To assess the temperature difference in the Al-25at.%Ni sample, it is assumed that the thermal conductivity of the alloy is equal to the thermal conductivity of pure Al, which is $\lambda = 2.26\,\mathrm{J\,cm^{-1}\,s^{-1}\,K^{-1}}$ at room temperature [95]. The thermal conductivity of copper at room temperature is $\lambda = 3.94\,\mathrm{J\,cm^{-1}\,s^{-1}\,K^{-1}}$ [95]. During heating

and cooling the temperature differences inside the sample are thus estimated to be $T_{\mathrm{dif}}^{\mathrm{h}} \approx 1.2\,\mathrm{K}$ and $T_{\mathrm{dif}}^{\mathrm{c}} \approx 0.2\,\mathrm{K}$, respectively.

For terrestrial EML experiments using a silicon sample, Pericleous et al. [94] observed a temperature difference of $T_{\mathrm{dif}} \approx 3\,\mathrm{K}$ in the simulations. The thermal conductivity of silicon at room temperature is $\lambda = 1.56\,\mathrm{J\,cm^{-1}\,s^{-1}\,K^{-1}}$ [96]. The approximation yields a temperature difference of $T_{\mathrm{dif}} \approx 2.0\,\mathrm{K}$ for a pure Al sample. The temperature difference using the ISS-EML and terrestrial EML are negligible compared to the absolute temperatures achieved during the processing. It is, hence, concluded that the absence of a steady-state temperature distribution in the sample is not the reason behind the growth anomaly.

The influence of vacancies has been analysed by Hillert et al. for pure metals [97] and Zheng et al. for the AlNi B2 phase [98]. However, Hillert et al. and Zheng et al. found that the front velocities need to be faster than the velocities measured in the present work. Therefore, the influence of vacancies is also disregarded.

Although the multiple nucleation is the most promising explanation for the anomaly, the influence of forced convection, inverse melting and varying fractions of the solidifying phases are discussed, too. The subsections are based on the discussion in Ref. [88].

Forced convection

Solidification velocities in Al-50at.%Ni were measured on ground and in parabolic flight campaigns [59,78]. It was found to what extent convection has an influence on the growth velocity; in fact it strongly increases the velocity for low undercoolings. The influence of the fluid flow inside the sample was theorectically assessed in Refs. [99, 100], and a comparison between theory and experiments is documented in Ref. [101].

However, the velocity-vs.-undercooling relation in Fig. 4.5 shows no difference between the data measured on earth and in space. To better understand the fluid flow inside the sample in space, simulations were carried out [102].

The results provided by the simulation include the fluid flow velocity for both turbulent and laminar flow, respectively. In the case of turbulent flow, the maximum velocities are in the range of $v_{\mathrm{max}} = 0.4$ to $1.0\,\mathrm{m\,s^{-1}}$, and the maximum velocities during laminar flow in the order of $v_{\mathrm{max}} = 0.040$ to $0.055\,\mathrm{m\,s^{-1}}$ [102]. Compared to results for EML experiments on earth with $v = 0.3\,\mathrm{m\,s^{-1}}$ [58, 75, 76], the fluid flow velocity is strongly reduced in microgravity. However, this reduction

does not change the measured kinetics, and thus forced convection is ruled out to be the origin of the growth anomaly.

Inverse melting

A further possible explanation for the anomaly in Al-Ni alloys is inverse melting as introduced by Greer [103]. Inverse melting describes the remelting of a solid phase upon cooling. Similar effects were observed in systems exhibiting a retrograde monovariant line where partial remelting of a crystal was shown to be possible. A difference is that a retrograde liquid line leads to partial remelting, whereas inverse melting may lead to complete remelting of the crystal. The inspiration for this theory were observations by Blatter and von Allmen [104] in a Ti-30at.%Cr layer on a tungsten substrate. The authors report that in two annealing steps the amorphous phase was first transformed to a crystalline phase by annealing at $T = 1073\,\mathrm{K}$ and back to the amorphous phase at $T = 873\,\mathrm{K}$.

For inverse melting, first a solid crystalline phase needs to precipitate from the melt. Upon further cooling, the Gibbs free energy curves for solid and liquid need to intersect again at a temperature T_i below which inverse melting would be thermodynamically possible. This would only be possible if the low temperature liquid had a lower entropy than the crystalline solid. Upon further cooling, a third intersection of the Gibbs free energy curves leading to resolidification is inevitable, because in the case of alloys, a solid phase must be the most stable phase at $T = 0\,\mathrm{K}$. This requires a very unlikely course of the Gibbs free energy curves.

Taking a look at the entropies of the involved phases shows an unlikely behaviour: when the liquid is cooled, and the first solidification occurs, the entropy lowers. For example, the entropy difference between liquid and solid of pure Al is $\Delta S_f = 10.48\,\mathrm{J\,mol^{-1}\,K^{-1}}$ [95]. By definition, a crystal is a highly ordered system with long range order, e.g. fcc structure for pure Al. For inverse melting, the crystal needs to remelt or change into an amorphous phase during cooling. This requires a lower entropy of the forming liquid or amorphous phase. Due to the highly ordered crystalline phase, this progression of the entropy is implausible.

In Al-50at.%Ni, a metastable disordered phase with superlattice structures was found [67]. However, referring to the phase selection experiments by Shuleshova et al. [23–27], Al_3Ni_2 is the primary phase in Al-25at.%Ni. Although it can not be excluded that the metastable AlNi B2 phase forms primarily, both, the Al_3Ni_2 and AlNi B2 phase, do not form an amourphous phase such as in the Ti-Cr system.

Molecular dynamics simulations presented in [105] showed that cooling rates of $\sim 10^{12}\,\mathrm{K\,s^{-1}}$ would be necessary to allow glass formation in Al-Ni alloys. These high cooling rates are not reached using the EML technique.

Assuming that there is an amorphous phase, which is regarded as a "frozen liquid", the glass transition temperature is of interest. Turnbull suggested that the glass transition temperature can be approximated by $T_g = 0.3T_l$ [29]. From the phase diagram, the two liquidus temperatures $T^{\mathrm{Al_3Ni_2}} = 1406\,\mathrm{K}$, i.e. T_{p2}, and $T^{\mathrm{AlNi\ B2}} = 1950\,\mathrm{K}$ can be extracted. These temperatures would lead to glass transition temperatures of $T_g^{\mathrm{Al_3Ni_2}} = 422\,\mathrm{K}$ and $T_g^{\mathrm{AlNi\ B2}} = 585\,\mathrm{K}$. In the electromagnetic levitation experiments presented here, the highest undercoolings were in the range of $\Delta T \approx 350\,\mathrm{K}$, which is equivalent to temperatures of $T = 1034\,\mathrm{K}$ in the Al-25at.%Ni alloy. Due to the significant difference between the glass transition temperatures and the achievable undercoolings, this can also not be the reason for inverse melting in this alloy. Because of this, the unlikely course of the Gibbs free energy curves and the implausible progression of the entropy, inverse melting is excluded to be the driving force for the anomalous behaviour.

Varying fractions of solidifying phases

A third idea for the reason behind the growth anomaly is the variation of fractions of phases that grow with different velocity. The measurements by Shuleshova et al. [23,24] show that the expected primary phase for the Al-25at.%Ni alloy is always Al_3Ni_2. Only in one instance the simultaneous growth of Al_3Ni_2 and Al_3Ni was observed for an Al-18at.%Ni sample [23, 24].

Calculations of dendrite growth velocities using a sharp interface model [62] were carried out [88], see Fig. 4.15. The curves all display the same monotonous increase for increasing undercooling. The Al_3Ni_2 phase, the favoured phase, has the highest growth velocities, followed by the AlNi B2 phase, which is not to be expected in this alloy. The Al_3Ni phase is the slowest one.

Assuming that the simultaneous growth of different phases occurs, the observed growth velocities can be calculated using the following equation [88]:

$$v = \frac{f_{\mathrm{AlNi}} v_{\mathrm{AlNi}} + f_{\mathrm{Al_3Ni_2}} v_{\mathrm{Al_3Ni_2}} + f_{\mathrm{Al_3Ni}} v_{\mathrm{Al_3Ni}}}{f_{\mathrm{AlNi}} + f_{\mathrm{Al_3Ni_2}} + f_{\mathrm{Al_3Ni}}}. \tag{4.8}$$

It can be seen that the velocity can indeed be a superposition of the different growth velocities. For that, the fraction of Al_3Ni would need to increase steeply to

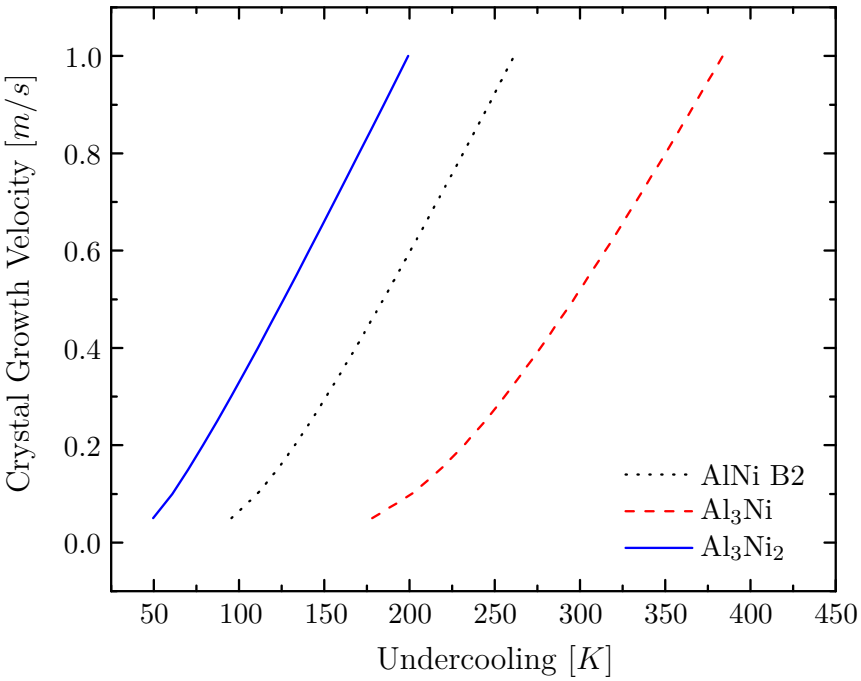

Figure 4.15: Results from the model [62] for the three phases AlNi B2, Al_3Ni_2 and Al_3Ni in the Al-Ni system at a composition of Al-25at.%Ni from [88] showing a monotonous increase.

compensate the velocity increase of the other two phases. The simultaneous growth of two or more phases in this alloy has not been observed experimentally by phase selection experiments. Referring to the results by Tourret et al. [49–51] it is not unlikely that two phases, the Al_3Ni_2 and Al_3Ni grow simultaneously. However, this was observed for small droplets obtained by gas atomization, i.e. very high cooling rates [57], and large undercoolings. Tourret et al. [49–51] also found that the Al_3Ni phase can overgrow Al_3Ni_2 phase and then block its growth during atomization. When this happens, Al_3Ni could grow freely into the melt, which would again follow the expected trend of increasing growth velocities for increasing undercooling. Furthermore, Tourret et al. [50] modelled the solidification of a sample processed using EML and only found growth of the Al_3Ni_2 phase. Hence, varying phase fractions are not the explanation for the anomaly.

Nucleation front

Evidence for the multiple nucleation events is provided by the microstructures, Subsection 4.1.6. These show that there are dendrites emerging from defined points on the sample surface that grow inwards towards the sample centre. In a layer

beneath the surface only dendrite arms with orientations pointing nearly radially inwards are selected. As the starting point on the sample surface is assumed to be a nucleation site for a dendrite, it is evident that the dendrite arms extending from one location show the same crystallographic orientation.

The distances between the nucleation sites where the dendrites start can be determined from the microstructure. The nucleation distances as determined for a few exemplary cases in the microstructure are in the range of $d \approx 460$ to $540\,\mu m$. The nucleation distances become larger for larger undercoolings. Keeping in mind that for the analysis of the scale distances in the video significantly more scales were analysed, the results for the nucleation or scale distance from the microstructure and video analysis, respectively, are in good agreement.

Combining the new microstructure results with the analyses from the videos, a new solidification mechanism is put forward. Instead of a solidification front build by dendrite tips [89, 93], a nucleation front propagates along the sample surface. Each scale in the video represents a nucleus from which dendrites emerge and grow. Ilbagi and Henein [56] report similar results showing several heterogeneous nucleation sites in atomized samples of Al-20at.%Ni. This supports the idea of the new solidification mechanism, described in the following paragraph.

A sketch of the proposed growth mode is shown in Fig. 4.16. The solidification starts with the first nucleus on top of the sample. From there the growth front of newly forming nuclei propagates along the sample surface, coloured arrows on the sample surface. As from each nucleus a dendrite grows inwards (coloured arrows pointing inwards), all dendrites meet by (soft) impingement at a point inside the sample [106], denoted by the orange circle. When the dendrite growth velocity is significantly lower than the front propagation velocity, the dendrites intersect nearly in the sample centre. For larger dendrite growth velocities, the focal point of the dendrites is shifted closer to the point of the last scale [106], in Fig. 4.16 the lowest point of the sample circle. The orange circle would thus be shifted closer to the green arrows on the sample surface.

A consequence of the growth front being a nucleation front is that the analysis method used for the growth velocities by Lengsdorf [4, 5] and in the present work is not valid for the scaled morphology. In this case, the assumption that the envelope of the dendrite tips grows spherically is not fulfilled.

By theoretical considerations, it was shown that for dynamic stability of the solidification front, a positive slope of the velocity-vs.-undercooling relation,

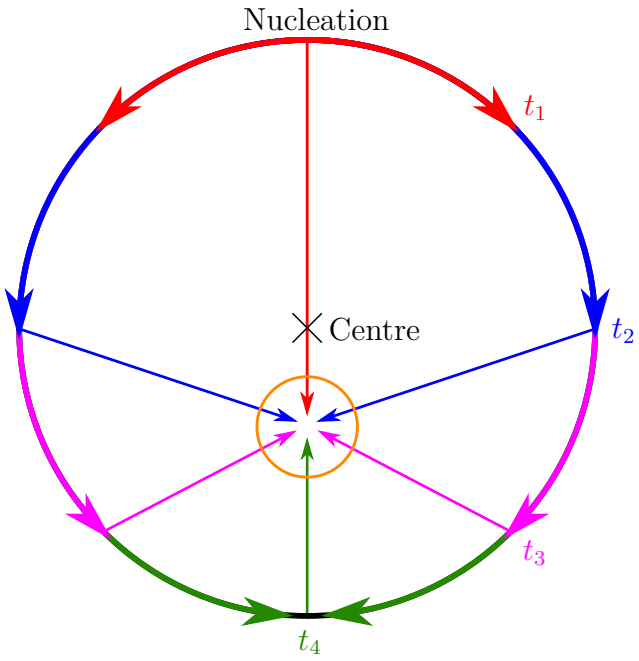

Figure 4.16: Proposed growth mode during scaled solidification: the nucleation front on the surface propagates at a much higher velocity than the growth velocity of the dendrites. The front forms a shell around the sample, and the growing dendrites meet at a point off the sample centre.

$\mathrm{d}v\,/\mathrm{d}\,(\Delta T) > 0$, is required [2, 3]. If the measured velocity is the velocity of the nucleation front and not the dendrite growth velocity, this principle is not violated. The negative slope is thus a consequence of the growth and formation of new scales and not correlated with the dendrite growth velocity. According to the experimental observations scales only form in the range of the velocity curve with negative slope, because the number of scales decreases for increasing undercooling. The increasing size of the scales cannot compensate the reduced number of scales.

The front velocity v_f can in the case of the nucleation front be calculated from the measured data via $v_\mathrm{f} = \pi v_\mathrm{m}/\,2$ because of the spherical shape of the sample. The assumption for the front velocity determination is that the solid grows spherically. This assumption does not hold for the scales as they grow along the surface, and dendrites grow from the scales. Therefore, the distance which needs to be used for the calculation of the velocity is not the diameter of the sphere but half its circumference.

As suggested by Mullis [106], this imposes a constraint on the dendrite growth velocity v_D which needs to fulfil $v_D < 2/\,\pi v_\mathrm{f}$. If the dendrite growth velocity is larger than the front velocity, the solidification proceeds as expected by a spherically growing envelope. As the examined sample show, the focal point is often located at the sample centre, it can be concluded that v_D is much smaller than v_f because the more similar the velocities are, the farther away is the meeting point of the dendrites from the sample centre. After the scales form a shell on the surface of the sample, further solidification leads to shrinkage pores in the sample.

The proposed mechanism is quite similar to that suggested in Refs. [60,71,72]. In these references, it is suggested that nucleation happens in a layer on the surface of the sample and dendrites grow from the surface to the centre of the sample. Only Paul [72] indicated a relation to the velocity-vs.-undercooling relation and that the size of the scales is determined by the undercooling. However, size and density of scales were not quantified. It is shown in the present work for the first time that the scale distance and radius increase with increasing undercooling, while the number of scales decreases.

The new results indicate that the anomaly in the Al-Ni system is not an anomaly of the growth behaviour but an anomaly of the nucleation. Althouhg growth front nucleation has been observed in phase-field simulations [34–38] or molecular dynamics simulations [39], a conclusive explanation for the stimulated nucleation cannot be provided with respect to the experiments presented here.

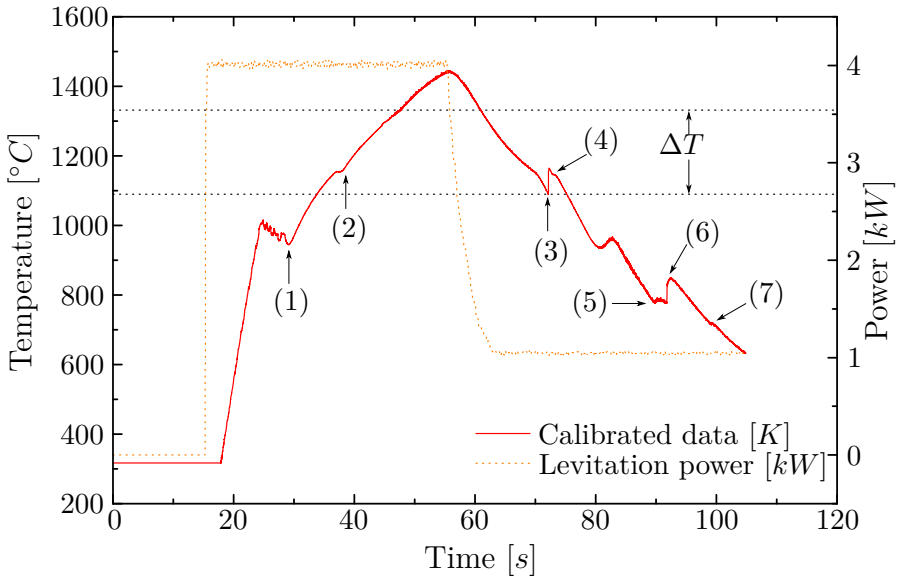

Figure 4.17: Temperature/time profile of a Al-28.5at.%Ni sample solidified on earth at an undercooling of $\Delta T = 219\,\mathrm{K}$ (see text for processes/effects occurring at marked points)

As the previous discussion concentrated on the undercooling range where the scaled morphology was observed, $\Delta T < 300\,\mathrm{K}$, a change in the solidification mechanism is indicated by the change in the front morphology observed in microgravity at larger undercoolings. Due to the low number of data points, this cannot be satisfactorily evaluated.

4.2 Measurement results for Al-28.5at.%Ni samples

The second alloy that was investigated was the Al-28.5at.%Ni alloy. As this alloy is in between the Al-25at.%Ni and Al-30at.%Ni alloys which show an overall negative trend of the velocity curve [4, 5], it is expected that the Al-28.5at.%Ni shows the same behaviour. For this alloy only measurements on earth were carried out.

4.2.1 Characteristics of the temperature/time profile

A representative temperature/time profile for the solidification of the Al-28.5at.%Ni alloy is depicted in Fig. 4.17. It shows the solidification of a sample solidifying at an undercooling of $\Delta T = 242\,\mathrm{K}$. The solid red curve shows the calibrated temperature and the dotted orange curve the power. As no detailed measurements

of the emissivity as for Al-25at.%Ni and Al-35at.%Ni are available, the calibration was applied to the entire cycle.

Again the characteristic features like oxide break-up at (1) and a plateau for the peritectic reaction at (2) are visible. When the liquidus temperature is reached, marked with the upper dotted straight line, during heating (heating power see dotted line in Fig. 4.17), a change of slope is visible. When the required superheating is reached, the heating power is reduced and the sample starts to cool down. Convective cooling by He gas is initiated shortly before the first recalescence (3). According to the phase diagram, the AlNi B2 phase solidifies primarily. Quickly after the recalescence, a small plateau is visible (4). This is the first peritectic reaction as described above.

The phase diagram implies that after the peritectic reaction at (4) a second peritectic and a eutectic reaction occur. However, in the temperature/time profile three following events can be found. At (5) a small recalescence and an unexpected plateau are visible. The plateau at (5) occured only occasionally, and not during all cycles. No reliable correlation to the initial undercooling, the temperature of the small recalescence or to the undercooling relative to the peritectic reaction was found.

After the plateau, a more distinct recalescence at (6) occurs. This can be associated with the second peritectic reaction and the formation of Al_3Ni, followed by the eutectic reaction leading to the plateau at (7). The temperature of the eutectic plateau is approximately 100 K too high because of the calibration is carried out for the melt and therefore not accounting for the changed emissivity.

4.2.2 Plane, wavy and scaled front morphologies

During the processing of the Al-28.5at.%Ni alloy, three different growth morphologies were observed: plane, wavy and scaled.

A plane front was observed up to undercoolings of $\Delta T \approx 150\,\mathrm{K}$. An example is shown in Fig. 4.18 (a). The bright solid phase appears to have a planar interface to the remaining liquid. In this case the solidification started on the back side of the sample.

At the highest undercoolings above $\Delta T > 180\,\mathrm{K}$, the front shows scales, which were already observed in Al-25at.%Ni, see Subsection 4.1.2. In Fig. 4.18 (b), an example for this morphology is depicted. The formation and brightness distribution - bright outline enclosing a darker area - are similar as those in Al-25at.%Ni.

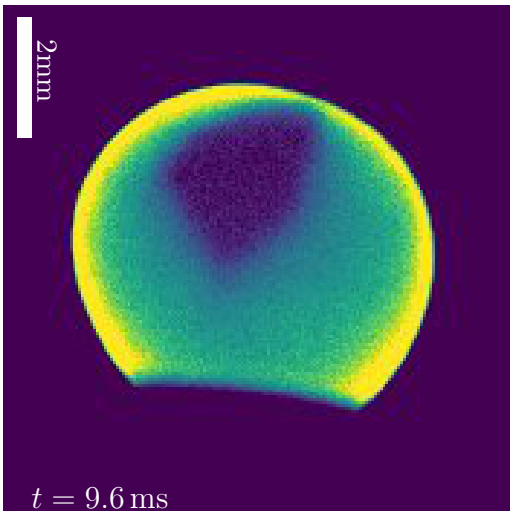

(a) Snapshot of a plane front at $\Delta T = 147\,\mathrm{K}$

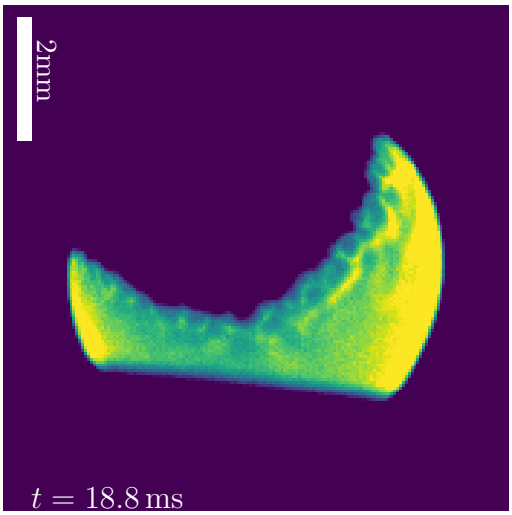

(b) Snapshot of scales at $\Delta T = 295\,\mathrm{K}$

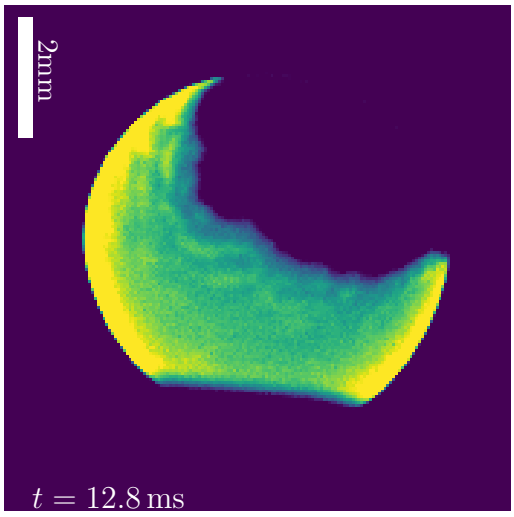

(c) Snapshot of a wavy front at $\Delta T = 219\,\mathrm{K}$

Figure 4.18: Three different front morphologies were observed: plane, Fig. 4.18 (a), scaled, Fig. 4.18 (b) and wavy, Fig. 4.18 (c),.

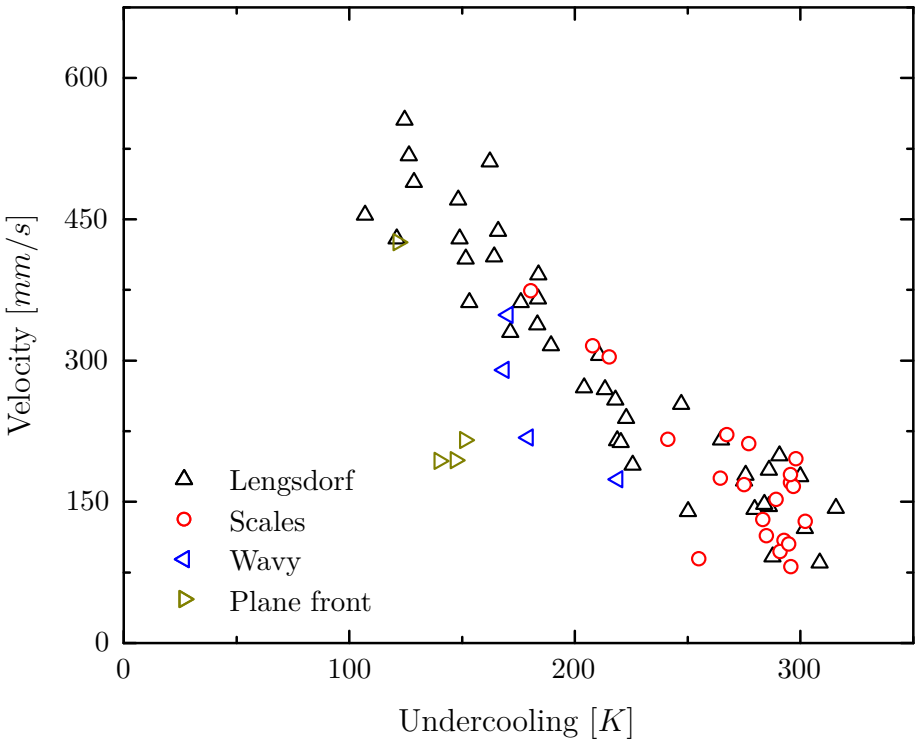

Figure 4.19: Negative velocity trend in Al-28.5at.%Ni with large scatter at the end and some outliers mostly due to the correction for the end of solidification but showing the same trend as the Al-30at.%Ni alloy (taken from [5]; wavy and scaled front morphologies overlap.

Behind the front in Fig. 4.18 (c), bright stripes are visible which are essentially parallel to the front. These stripes can also be found at intermediate undercoolings $160\,\mathrm{K} < \Delta T < 220\,\mathrm{K}$. Because no distinct scales like in Fig. 4.18 (c) were visible, this front type is classified as wavy.

4.2.3 Velocity measurement results for Al-28.5at.%Ni

For Al-28.5at.%Ni, velocity measurements were successfully carried out for undercoolings in the range of $100\,\mathrm{K} < \Delta T < 300\,\mathrm{K}$. The same method which was used to determine the velocities in the Al-25at.%Ni alloy was applied, described in Subsection 4.1.3.

In Fig. 4.19 the results of the measurements are shown. The black triangles represent data obtained by Lengsdorf et al. [5] for an Al-30at.%Ni alloy. Although the concentration is different, the new data points for Al-28.5at.%Ni show the same trend and order of magnitude as measured for Al-30at.%Ni. The velocity decreases

linearly over the whole range of measured undercoolings up to $\Delta T = 300\,\mathrm{K}$. Most of the outliers are due to the correction of the radius for the end of solidification, see Subsection 4.1.3.

In analogy to the classification of the growth front and front velocity in Al-25at.%Ni, the different markers in Fig. 4.19 denote the various front morphologies. The dark yellow triangles pointing to the right show the regime of the plane front. This front was observed for undercoolings up to $\Delta T \approx 150\,\mathrm{K}$. Between $\Delta T = 160$ and $220\,\mathrm{K}$ the front showed a wavy morphology. The front shows the scaled morphology for undercoolings $\Delta T > 180\,\mathrm{K}$.

4.2.4 Results obtained by tomographic analysis

Tomography was also applied for this alloy using a sample solidified at an undercooling of $\Delta T = 151\,\mathrm{K}$ with the scaled morphology. The mounting resin is again visible as the grey particles below the sample in Fig. 4.20 (a). The dark grey part of the sample surface was in contact with the mounting resin, and its colour is a remnant of the image enhancement. However, the sample surface shows an even structure. The light grey surface is disturbed by evenly distributed dark spots. These could be identified as points on the surface, but are not as clear as the ones in Fig. 4.8 (a) for Al-25at.%Ni.

The interior of the sample in Fig. 4.20 (b) shows a fine structure. A few shrinkage holes are distributed close to the surface. Close to the sample centre, a shrinkage pore can be seen. Further inside the sample, the pore is larger, and the fine structure is now visible as a layer underneath the surface with a thickness of $d \approx 1.8\,\mathrm{mm}$. Inside the pore, dendritic structures pointing inwards are visible. These seem to emerge from the fine structured layer. However, a unique origin cannot be identified. After crossing the sample centre with the sections, the central pore vanishes, and the fine grained structure fills again the whole image.

4.2.5 Microstructure analysis

In order to analyse the microstructures of samples solidified at different undercoolings, four representative samples were chosen with undercoolings prior to solidification of $\Delta T = 32\,\mathrm{K}$, $151\,\mathrm{K}$, $255\,\mathrm{K}$ and $296\,\mathrm{K}$.

At the smallest undercooling, $\Delta T = 32\,\mathrm{K}$, the microstructure shows coarse dendritic structures, see Fig. 4.21 (a). The structure does not change significantly in

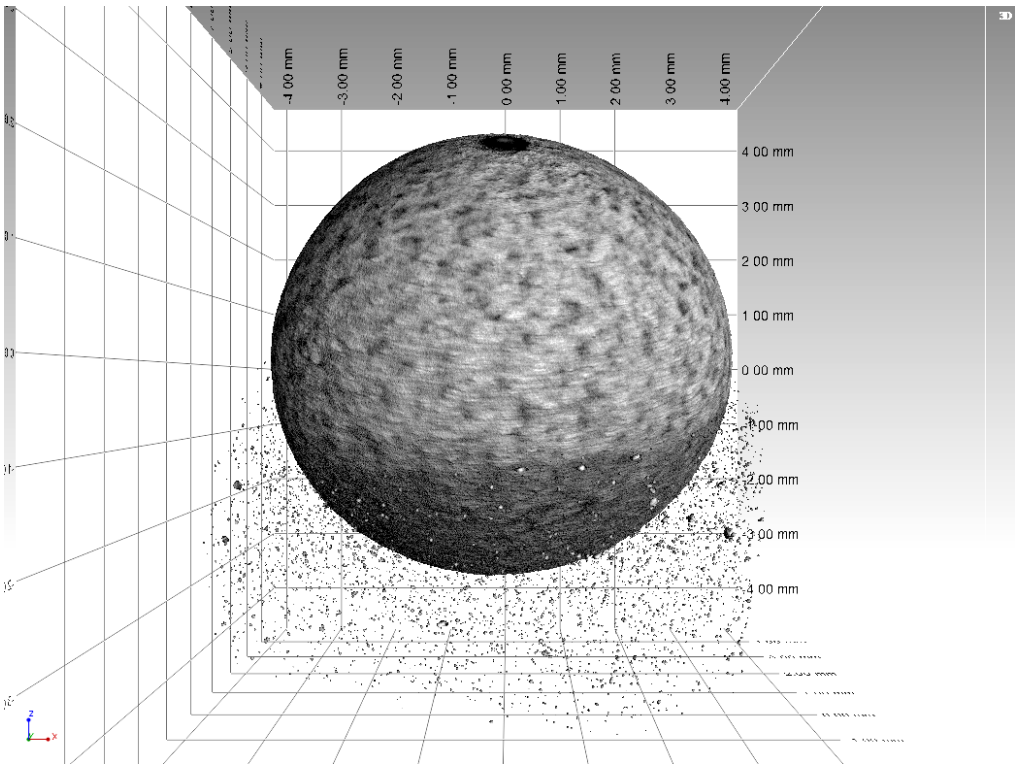

(a) Reconstructed sample surface without any prominent features unlike the Al-25at.%Ni sample in Fig. 4.8.

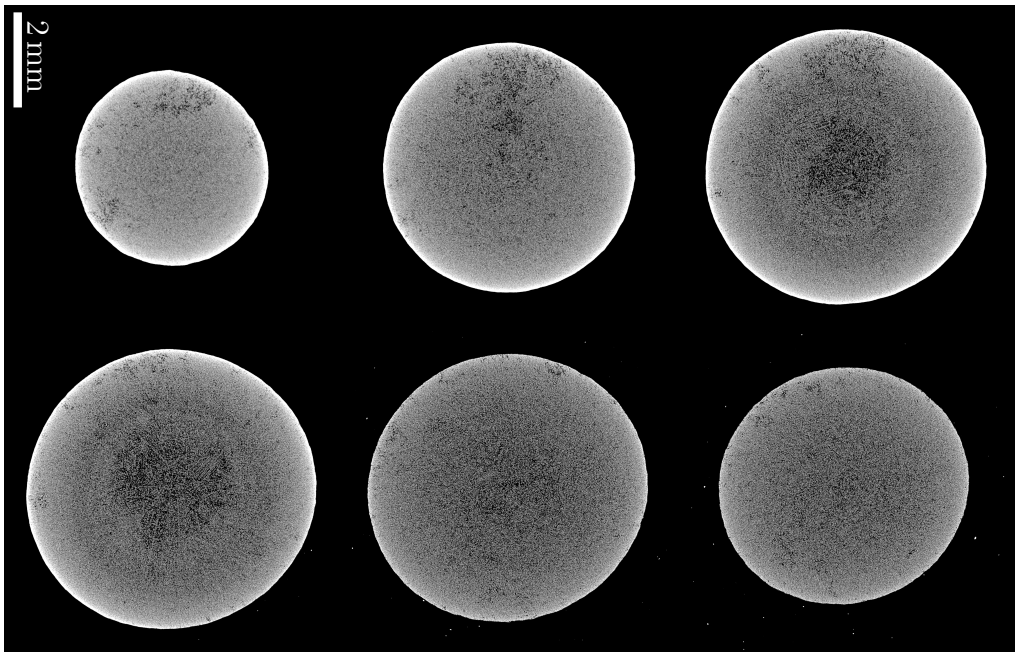

(b) Uniform microstructure inside the sample except for a small part at the sample centre showing inwards oriented dendrite arms.

Figure 4.20: Tomography results of an Al-28.5at.%Ni sample solidified at $\Delta T = 151\,\mathrm{K}$.

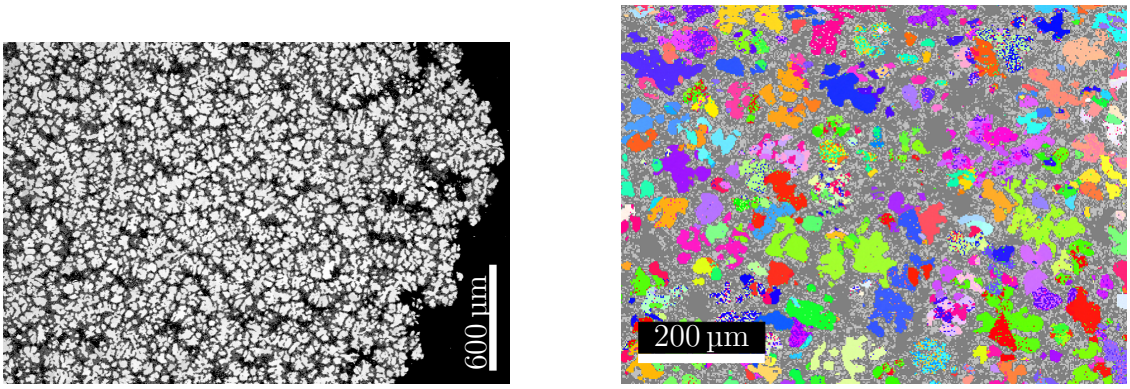

(a) Small dendrites

(b) Various orientations of dendrites.

Figure 4.21: Microstructure of Al-28.5at.%Ni solidified at $\Delta T = 32\,\mathrm{K}$ showing small dendrites with various orientations.

the interior of the sample. The dendrites show a bright grey interior representing the Al_3Ni_2 phase which is surrounded by dark grey, the Al_3Ni phase. To determine the crystallographic orientation, EBSD measurements were carried out. Fig. 4.21 (b) shows the result for the Al_3Ni_2 phase. The dendrites all show different orientations. The used colour code is shown in Fig. 4.12 (c).

For a small number of dendrites, the size was measured using the area of the Al_3Ni_2 phase in Fig. 4.21 (b). The measured sizes are in the range of $d \approx 60$ to $219\,\mu\mathrm{m}$. Compared to the sizes determined for the dendrites in Al-25at.%Ni in Fig. 4.9 (b), which are in the range of $d \approx 164\,\mu\mathrm{m}$ to $523\,\mu\mathrm{m}$, the dendrites in this Al-28.5at.%Ni alloy are smaller.

At $\Delta T = 151\,\mathrm{K}$, the microstructure changed as shown in Fig. 4.22. The growth front during solidification was attributed to be planar. The microstructure shows a layer with a fine dendritic structure at a small magnification in Fig. 4.22 (a). The layer has a thickness of $d \approx 1.8\,\mathrm{mm}$ beneath the surface. From that layer, dendrite arms extend inwards towards the sample centre. Two of these dendrite arms are marked exemplarily by magenta arrows. Shrinkage pores, denoted by cyan arrows, are visible on the right hand side of the sample as well as in the sample centre.

At a higher magnification, the red rectangle in Fig. 4.22 (a) denotes the area which is magnified in Fig. 4.22 (b), the layer with the fine dendritic structure is better visible. At this magnification it is evident that the dendrite arms reaching into the sample emerge from that fine dendritic structure, marked by the magenta arrow. An EBSD analysis of the red rectangle in Fig. 4.22 (b) is shown in

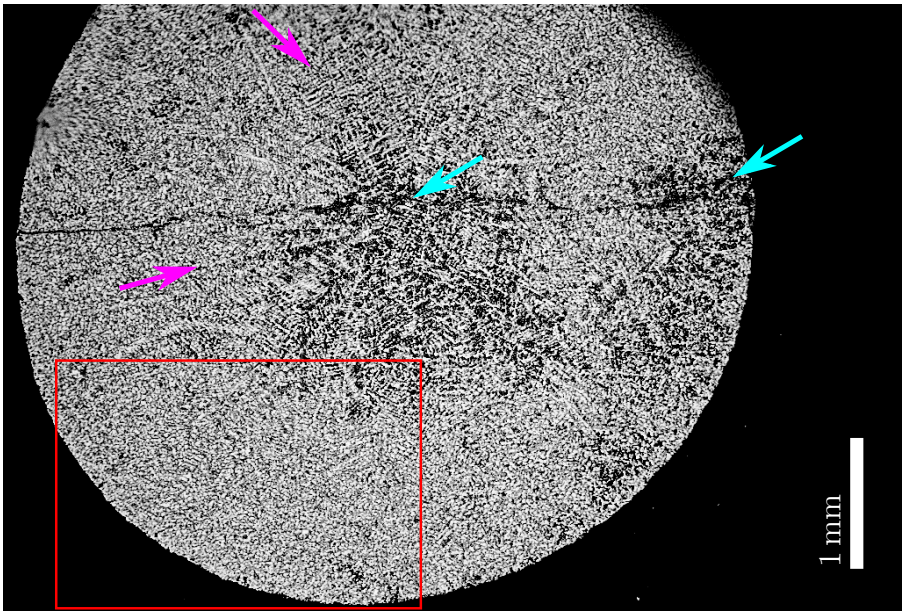

(a) Shrinkage pores in the sample centre and the right side, cyan arrows, with inwards pointing dendrite arms reaching into the shrinkage pores in the sample centre, magenta arrows

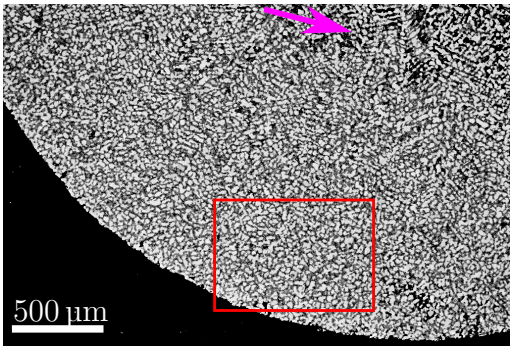

(b) Fine structure beneath the sample surface with radially inwards pointing dendrites emerging from the fine structured layer, magenta arrow

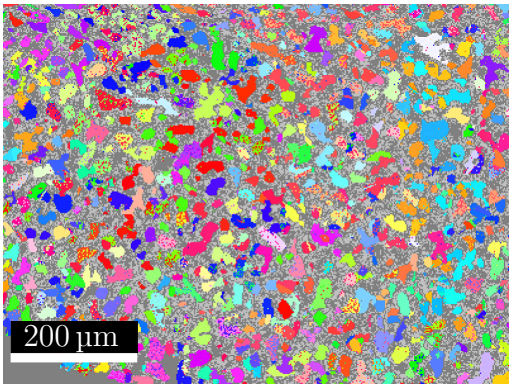

(c) Various orientations of the dendrite interiors composed of Al_3Ni_2 in the solid shell beneath the surface.

Figure 4.22: Sample solidified at an undercooling of $\Delta T = 151\,\mathrm{K}$; red rectangles denote the area of the next image, i.e. red rectangle in (a) for (b) and in (b) for (c).

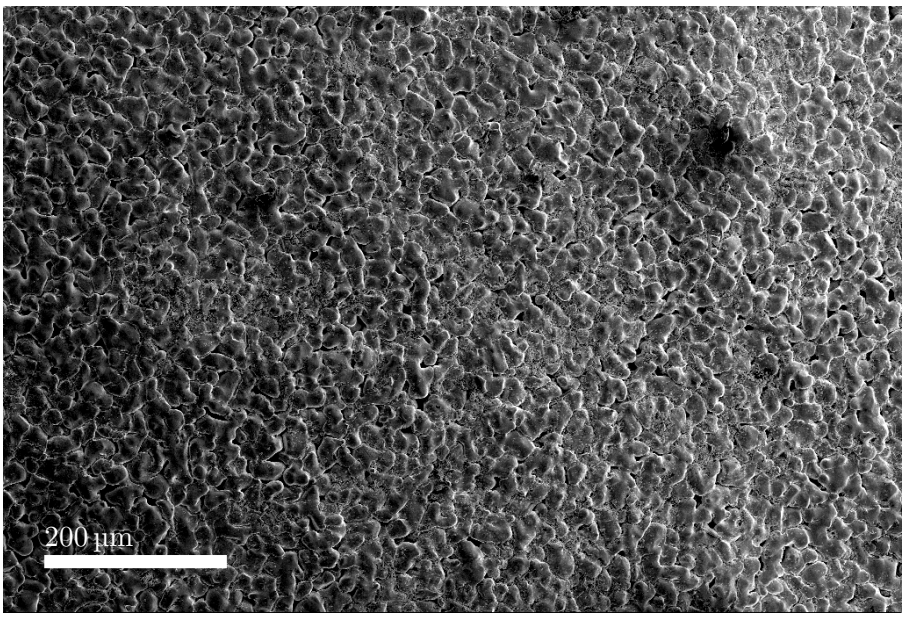

Figure 4.23: Surface of sample solidified at an undercooling of $\Delta T = 255\,\mathrm{K}$ showing a different topography than the circular features of Al-25at.%Ni (Fig. 4.10) or the rough topography (Fig. 4.13 (a))

Fig. 4.22 (c). Only the results representing the Al_3Ni_2 phase are depicted. Similar microstructural features are found in the sample solidified at $\Delta T = 32\,\mathrm{K}$. The dendrite core is identified as Al_3Ni_2 and it is surrounded by Al_3Ni. The size of the Al_3Ni_2 spots are approximately $d \approx 50$ to $94\,\mu\mathrm{m}$.

The first sample selected for microstructure analysis, which showed scales during solidification, solidified at an undercooling of $\Delta T = 255\,\mathrm{K}$. Because of the scaled morphology, the surface of this sample was inspected, see Fig. 4.23. The surface of the sample shows an uneven topography which does not show the circular features, see Fig. 4.10, or is as rough as the topography in Fig. 4.13 (a), which were observed in Al-25at.%Ni. However, the topography seen in Fig. 4.23 does not show strong deviations along the whole surface.

The microstructure inside the sample solidified at an undercooling of $\Delta T = 255\,\mathrm{K}$ is shown in Fig. 4.24. The microstructue in Fig. 4.24 (a) shows a fine dendritic structure across the entire section. Although this fine dendritic structure resembles the structure which has been observed in the previously described sample, solidified at an undercooling of $\Delta T = 151\,\mathrm{K}$ presented in Fig. 4.22, no clear dendrite arms are visible at this magnification (Fig. 4.24 (a)). Shrinkage pores, exemplarily marked by the cyan ellipse, are also found. These shrinkage pores, however, are not con-

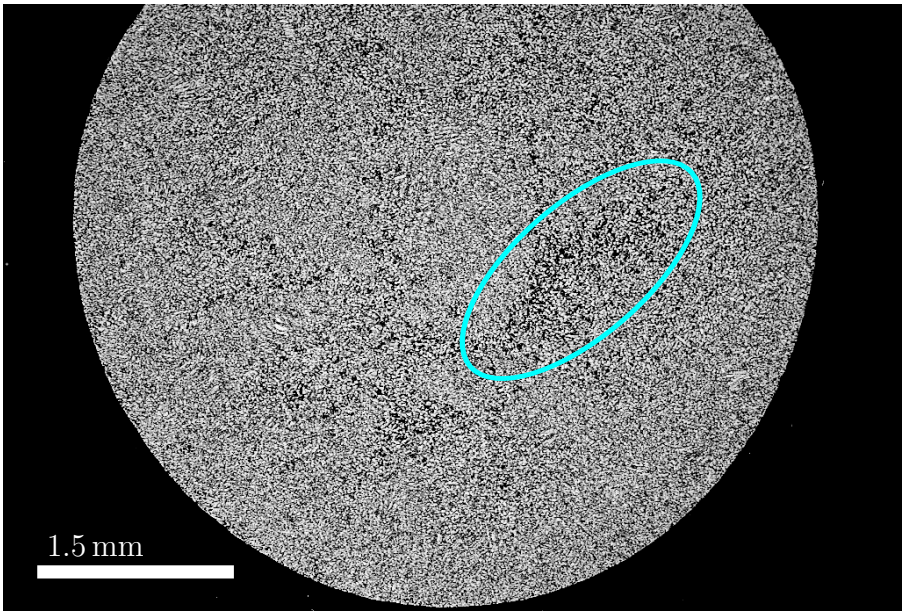

(a) Fine structure in the sample with shrinkage pores (cyan ellipse).

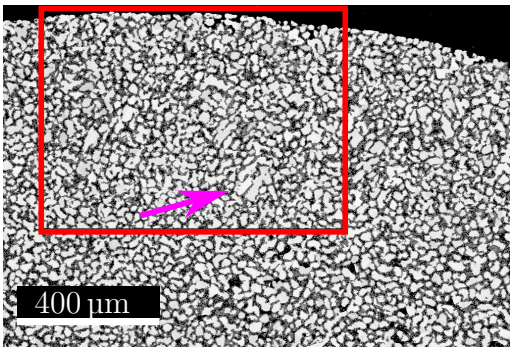

(b) Microstructure with dendritic structures, magenta arrow.

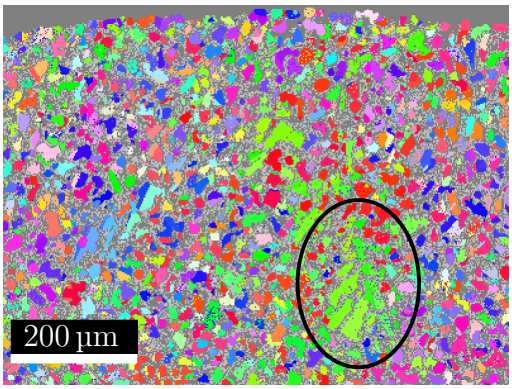

(c) EBSD analysis of the area marked by the red rectangle in Fig. 4.24 (b) showing dendritic features, black circle

Figure 4.24: Microstructure and EBSD measurement results of a sample solidified at an undercooling of $\Delta T = 255\,\mathrm{K}$ showing a fine structure across the entire section with only a few visible dendrite arms.

centrated in the centre of the sample, as it was found for the previous sample, see Fig. 4.22 (a).

Fig. 4.24 (b) shows an image with a higher magnification. It becomes more evident that the fine dendritic structure is similar to that of the sample solidified at an undercooling of $\Delta T = 151\,\mathrm{K}$ in Fig. 4.22. Also, a dendrite arm-like structure is visible which is marked by the magenta arrow in Fig. 4.24 (b). The red rectangle shows the area which was analysed by means of EBSD. The result of the EBSD analysis is shown in Fig. 4.24 (c). The result is again only shown for the Al_3Ni_2 phase. In analogy to the previous results, the interior of the dendrites is again Al_3Ni_2 which is surrounded by the Al_3Ni phase. A measurement of a few sizes of the dendrite cores yields lengths of $d \approx 18$ to $176\,\mu\mathrm{m}$ for the dendrite arm.

The sample with the largest undercooling investigated by means of scanning electron microscopy solidified at $\Delta T = 296\,\mathrm{K}$. The growth front showed the scaled morphology. Fig. 4.25 shows two microstructure images of this sample. The overview image in Fig. 4.25 (a) shows a fine dendritic structure. The microstructure shows the same structure across the entire section. At a higher magnification of a position close to the sample centre, it becomes visible that the white areas, identified as Al_3Ni_2, e.g. magenta arrow in Fig. 4.25 (b), are surrounded by a dark grey phase, Al_3Ni, yellow arrow, as well as a light grey area with an undentified phase, cyan arrow. The area with an unidentified phase has an Al content of $c_{\mathrm{Al}} = 71\,\mathrm{at.\%}$ and Ni content of $c_{\mathrm{Ni}} = 29\,\mathrm{at.\%}$, determined by EDX.

For this sample two EBSD results are shown in Fig. 4.26. The EBSD results for the overview image in Fig. 4.25 (a) are shown in Fig. 4.26 (a). Depicted is again the result for the Al_3Ni_2 phase. In this image, Fig. 4.26 (a), it is evident, that large dendrites with fine dendrite arms exist in the sample. These are evident due to the same crystallographic orientation in the dendrite arm centre. For example, the black ellipse in Fig. 4.26 (a) marks one of the large dendrites. Above the ellipse, marked by the white dashed lines, a second dendrite can be identified.

The second finding from EBSD is shown in Fig. 4.26 (b). Boundaries inside a single dendrite interior consisting of Al_3Ni_2 can be found. The arrows emphasize the five different orientations (denoted by blue, pink, orange, yellow and green) which were observed while the arrow heads are coloured according to the orientation. The interface are either straight (yellow/orange, blue/lilac) or curved (yellow/green, orange/green). The EBSD results can be used to determine the rotation angle and an approximation for the rotation axis. The difference between the orientation

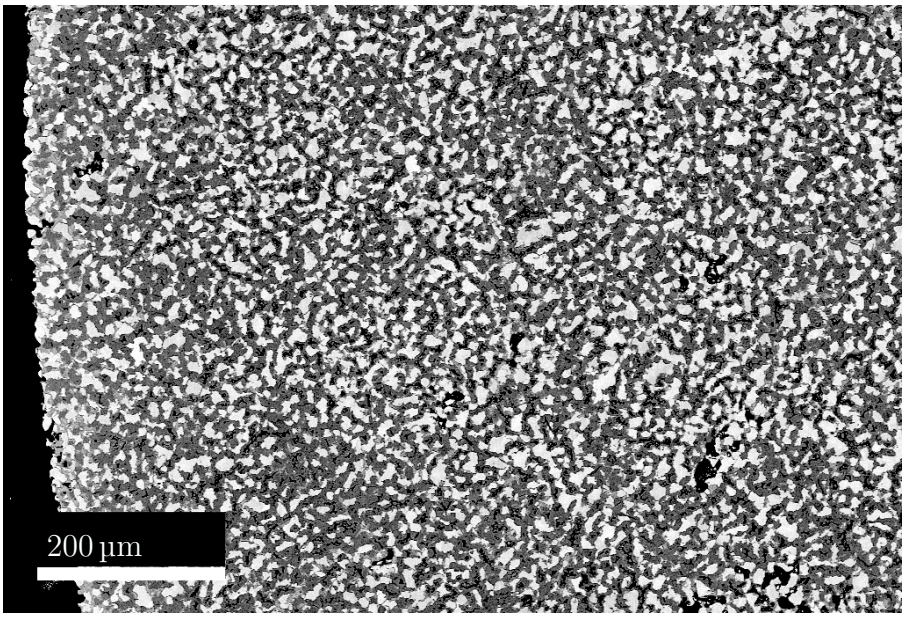

(a) Fine dendritic structure

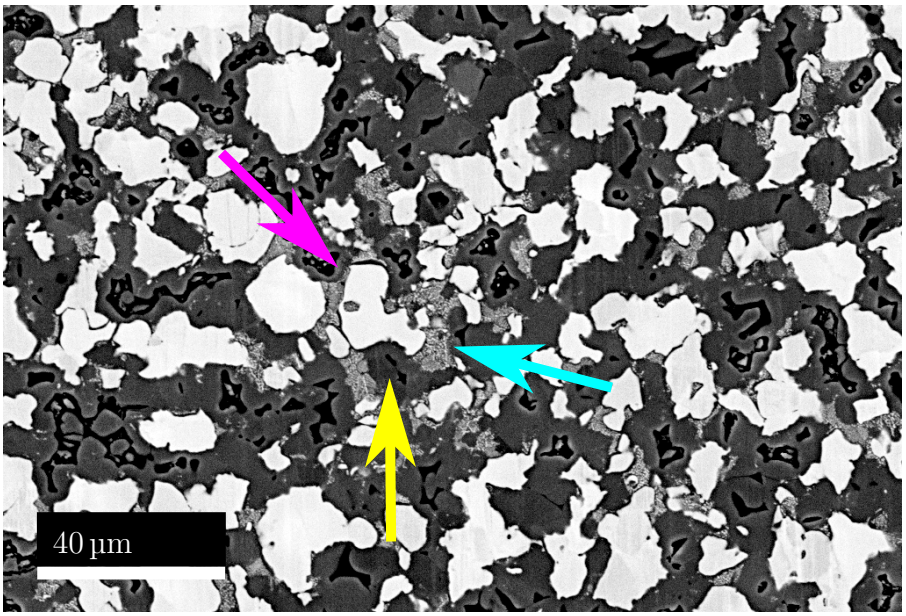

(b) Unidentified phase surrounding the Al_3Ni_2 phase.

Figure 4.25: Microstructural images of an Al-28.5at.%Ni sample solidified at $\Delta T = 296\,\mathrm{K}$ showing the fine structure in the whole sample.

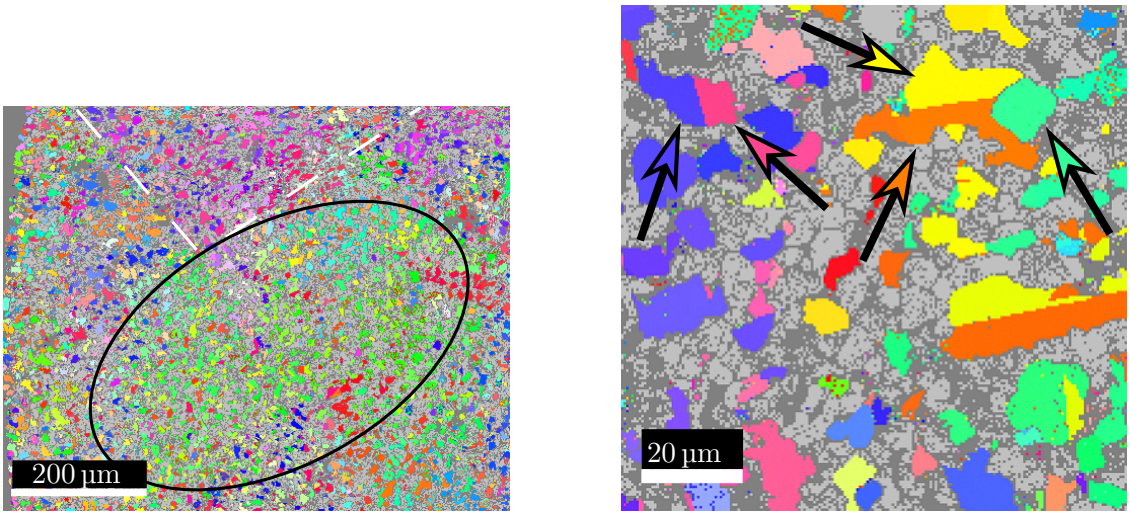

(a) Fine structure exhibits large dendrites inside the sample.

(b) Twin boundaries in the Al_3Ni_2 phase.

Figure 4.26: EBSD measurements showing large grains inside the sample and twin boundaries in the Al_3Ni_2 phase.

at the straight interface between pink and blue is a rotation of $\sim 91°$ around the $\left[1\bar{1}\bar{1}\right]$ axis. Between the yellow and orange parts, also a straight interface denoting a rotation by $\sim 90°$around the [211] can be seen. A curved interface between orange and green, and yellow and green denotes rotations by $\sim 57°$ around $\left[42\bar{1}\right]$, and $\sim 63.0°$ around $\left[\bar{3}\bar{2}1\right]$, respectively.

4.2.6 Discussion

According to the velocity measurements from Refs. [4, 5], the alloys with $c_{\mathrm{Ni}} = 30\,\mathrm{at.\%}$ and $31.5\,\mathrm{at.\%}$ show a negative slope over the whole range of measured undercoolings. As the Al-28.5at.%Ni alloy is in the same region of the phase diagram with respect to the primary phase and the transformation steps, it is reasonable to compare the Al-28.5at.%Ni alloy with Al-30at.%Ni and Al-31.5at.%Ni.

In the present work, experiments for the Al-28.5at.%Ni alloy were carried out which show the same negative slope of the velocity-vs.-undercooling curve over the whole range of measured undercoolings. The comparison between Al-28.5at.%Ni and Al-30at.%Ni in Fig. 4.19 shows that no significant difference between the velocity-vs.-undercooling relation of the two alloys exists. However, the classification of the front morphologies shows similar results compared to the Al-25at.%Ni alloy. The scales are the dominant morphology in the range of the negative slope.

This was reported in Ref. [72] for Al-31.5at.%Ni, too. At the lowest undercooling a plane front morphology was observed. This indicates that up to $\Delta T \approx 150\,\mathrm{K}$ the expected solidification mechanism of dendrite tips with a spherical envelope growing into the undercooled melt could be dominant. With increasing undercooling, the mechanism changes to the one described for Al-25at.%Ni, see Subsection 4.1.7, where a nucleation front propagates along the sample surface from which dendrites grow inwards. This is also validated by the microstructure. The larger scales at deeper undercoolings, described in [72], were also observed for the Al-28.5at.%Ni alloy, but not quantified due to the insufficient resolution of the video data.

During previous sounding rocket missions using Al-31.5at.%Ni, two front velocities were obtained which indicated the expected solidification behaviour of increasing growth velocities with increasing undercooling in the Al-31.5at.%Ni alloy [4, 5]. The microstructure of the sample shows dendrites pointing inwards from the sample surface [52, 60]. Based on the new results obtained here for the Al-25at.%Ni and Al-28.5at.%Ni alloy, this type of microstructure represents the negative slope and also in this case the front was a nucleation front, as suggested in Ref. [60]. This contradicts the suggestion in Refs. [4, 5] that the slope of the curve of the Al-31.5at.%Ni is governed by the gravitational conditions, i.e. positive in μg and negative in $1g$.

In-situ measurements by Shuleshova et al. [23–27] using the Al-31.5at.%Ni alloy showed that the primary phase is the AlNi B2 phase for low and intermediate undercoolings. For $\Delta T > 320\,\mathrm{K}$ the primary phase changes to Al_3Ni_2 in Al-31.5at.%Ni. Shuleshova et al. [23–27] also report that the primary AlNi B2 phase is completely transformed by the peritectic reaction to Al_3Ni_2 with respect to the measurement accuracy as the reflections of the Al_3Ni_2 phase superimpose those of the AlNi B2 phase. That these transformation steps are also present in the Al-28.5at.%Ni alloy is indicated by the microstructure results, as no residues of the primary phase were found. However, the microstructure mostly shows a dendritic structure. Yet, it significantly changes with undercooling. In samples with undercoolings $\Delta T \leq 151\,\mathrm{K}$, dendrite arms parallel to the section are visible, see Fig. 4.22. For larger undercoolings, $\Delta T \geq 255\,\mathrm{K}$, a fine structure of the whole bulk material is observed, see Fig. 4.24 and Fig. 4.25 (b).

During the in-situ measurements by Shuleshova et al., a metastable phase in Al-31.5at.%Ni was detected before the second peritectic reaction occured [23, 24, 26]. The formation of the metastable phase is visible as a plateau in the tempera-

ture/time profiles [23,24,26]. This plateau was also found in the temperature/time profiles of Al-28.5at.%Ni, marker (5) in Fig. 4.17. At the highest undercooling, the temperature/time profile does not show the plateau at (4), see Fig. 4.17, but a pronounced plateau at (5). The respective microstructure shows an unidentified phase in Fig. 4.25 (b). This was only found at this large undercooling, so it may be a residue of the decomposition of the metastable phase. The EDX results with a content of $c_{\mathrm{Al}} = 70.6\,\mathrm{at.\%}$ and $c_{\mathrm{Ni}} = 29.4\,\mathrm{at.\%}$ agrees well with the composition range of $c_{\mathrm{Al}} = 24$ to $30\,\mathrm{at.\%}$ documented in [47].

The EBSD analysis at the highest undercooling of $\Delta T = 296\,\mathrm{K}$ showed boundaries between different crystallographic orientations within an area filled by the Al_3Ni_2 phase in Fig. 4.26 (b). These boundaries denote rotations of either $\sim 60°$ or $\approx 90°$. The rotation of $\sim 60°$, which was found at straight boundaries, e.g. pink/blue or yellow/orange in Fig. 4.26 (b), resembles the angle of twins in the fcc system with 60°. Therefore, the possibility of twins in the Al_3Ni_2 crystals is briefly discussed.

In Refs. [107–109], where the latter two references are comments, a mechanism for the transformation of a B2 structure to a trigonal $P\bar{3}m1$ structure is presented. This corresponds to the transformation observed in the Al-28.5at.%Ni alloy during solidification. The AlNi B2 phase is transformed to the Al_3Ni_2 phase. The Al_3Ni_2 phase has a trigonal $P\bar{3}m1$ structure [110]. Further literature indicates twinning angles of 60° or 90° in hexagonal crystal structures [111,112]. However, these are for pure metals with a hexagonal crystal structure. As the results obtained by means of EBSD do not provide a high accuracy, the possible twinning either in Al_3Ni_2 or during the transformation of the AlNi B2 phase should be investigated further by using high-resolution transmission electron microscopy.

4.3 Results for the Al-35at.%Ni

The third and last investigated alloy was the Al-35at.%Ni alloy. The measurements by Lengsdorf et al. [5] show a minimum in the velocity-vs.-undercooling relation. To study this minimum in greater detail, experiments with this alloy were carried out on board the ISS.

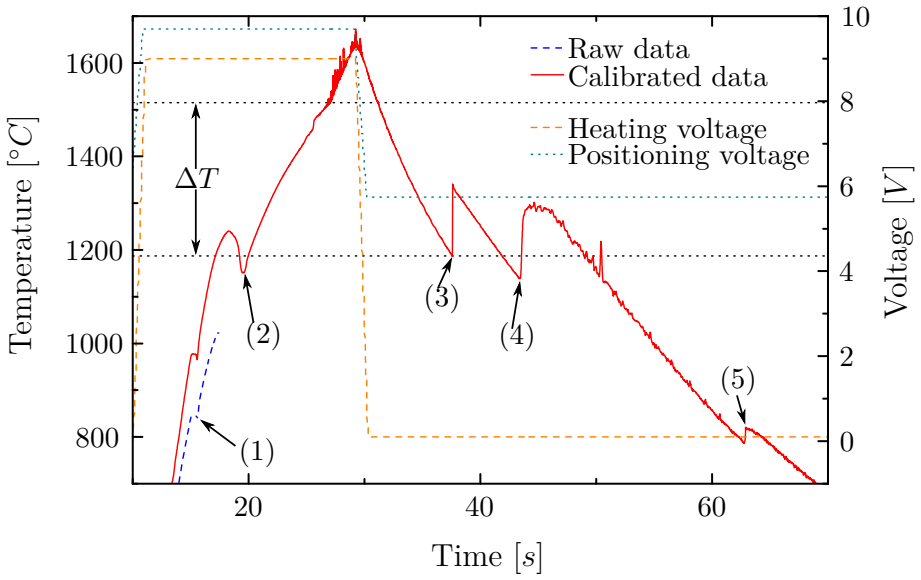

Figure 4.27: Temperature/timeprofile for Al-35at.%Ni. Raw data representing the correct temperature shown until oxide evaporation.

4.3.1 Characteristics of the temperature/time profile

In Fig. 4.27, a representative temperature/time profile recorded during the processing on board the ISS is shown. Beside the raw and calibrated data, the heating and positioning control voltages are depicted.

The temperature/time profiles for the Al-35at.%Ni alloy always show the same characteristic features, c.f. Fig. 4.27. During heating, three different points of interest are marked. At (1), a small plateau at $T \approx 850\,°\mathrm{C}$ in the uncalibrated data is seen. This corresponds to the peritectic temperature of Al_3Ni. Further heating leads to the evaporation of the oxides, and the measured temperature drops due to the change in emissivity, (2). Again, the temperature at which the sample is fully molten can be identified at the change of slope in the profile, marked by the upper dotted black line.

The first recalescence is marked by (3). The sample solidfied at an undercooling of $\Delta T = 329\,\mathrm{K}$. Shortly after the first recalescence, a second recalescence is clearly visible, marker (4). However, the recalescence temperature does not correspond to the temperature of a non-variant or univariant transformation in the phase diagram. Upon further cooling, at (5) a small recalescence with a maximum temperature close to the Al_3Ni peritectic temperature is visible.

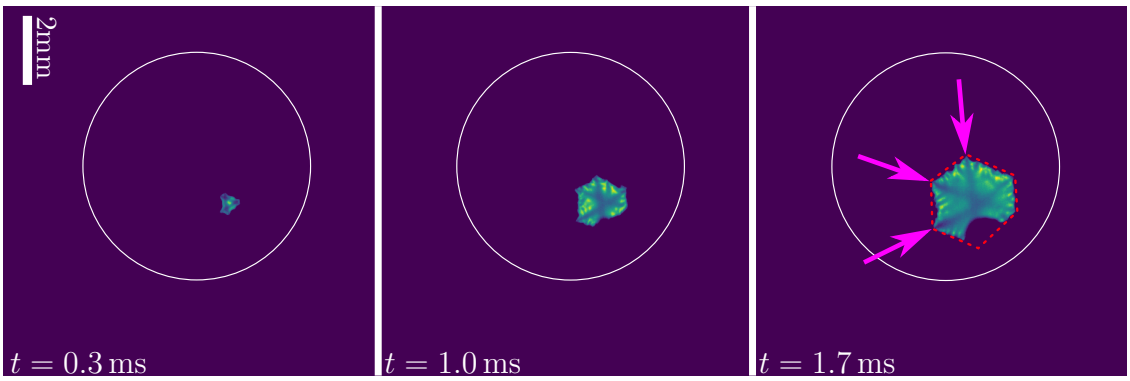

(a) Propagation of a dendritic growth front with hexagonal envelope shape; magenta arrows denote the dark lines, red dashed line denotes the front envelope.

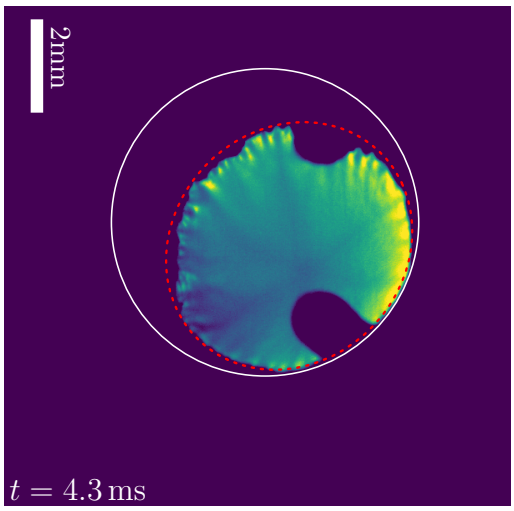

(b) Changed front envelope shape from hexagonal to circular

Figure 4.28: Snapshots of a solidification at an undercooling of $\Delta T = 329\,\mathrm{K}$ showing a dendritic front morphology.

4.3.2 Scaled and dendritic front morphologies

The videos recorded under microgravity conditions show three different front morphologies, from which one is seen in two different varieties. For undercoolings $\Delta T < 150\,\mathrm{K}$ a plane front was observed. At undercoolings ranging from $\Delta T \geq 190\,\mathrm{K}$ to $\Delta T \leq 250\,\mathrm{K}$, the scaled front morphology was found. To achieve these undercoolings, a trigger needle was used in parts of the experiments to initiate solidification. At the highest undercoolings $\Delta T > 300\,\mathrm{K}$, the front showed a dendritic morphology.

In Fig. 4.28, an image sequence with a dendritic front morphology at $\Delta T = 329\,\mathrm{K}$ is shown. Inside the solidified part, three dark lines each terminating in the dendrite

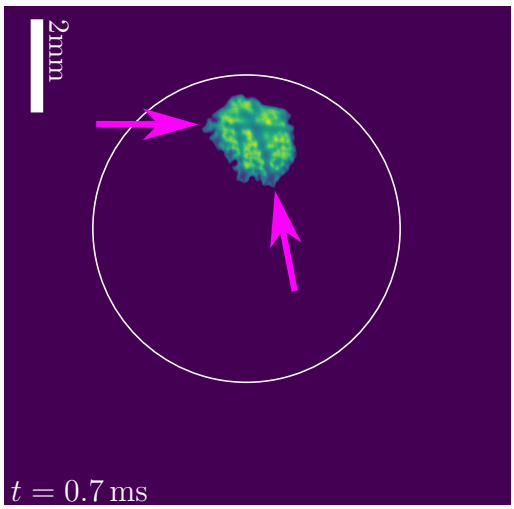

Figure 4.29: Dendritic structure with two visible dark lines, i.e. dendrite stems.

tips are visible, marked by magenta arrows. These dark lines could thus be primary dendrite stems. The edge of the whole solid resembles a hexagonal shape, red dashed line. At later times, the hexagonal outline is lost, and the front becomes circular. This is shown in Fig. 4.28 (b), denoted by dashed red line. Dendrite tips are visible around the entire outline.

The dendritic front morphology showed a second variety, where two primary dendrite stems can be identified, in Fig. 4.29 shown by two magenta arrows. Besides this difference to Fig. 4.28 (a), the front shows the same dendrite tips and behaviour as before.

Besides these variations of the dendritic morphology, again the scaled morphology was found for undercoolings ranging from $\Delta T = 190$ to 250 K, see Fig. 4.30 (a). In the experiments, the trigger needle was used to initiate solidification at a series of undercoolings. In Fig. 4.30 (b) the effect of the triggering is visible, white arrow shows the position of the needle. The first frame shows the moment when the needle touches the sample, i.e. $t = 0$ ms. From the contact point, the solidification starts, and the front grows with a circular morphology across the surface, $t = 1.3$ to 5.3 ms.

The image sequence in Fig. 4.30 (b) shows another feature which was described in Al-28.5at.%Ni (Subsection 4.2.2), particularly the stripes behind the solidification front, where one stripe is exemplarily marked by a black arrow at $t = 4.0$ ms. As can be seen in the image sequence, the centre of each scale is darker than its edge. When the edges merge, they form the stripes behind the solidification front. These

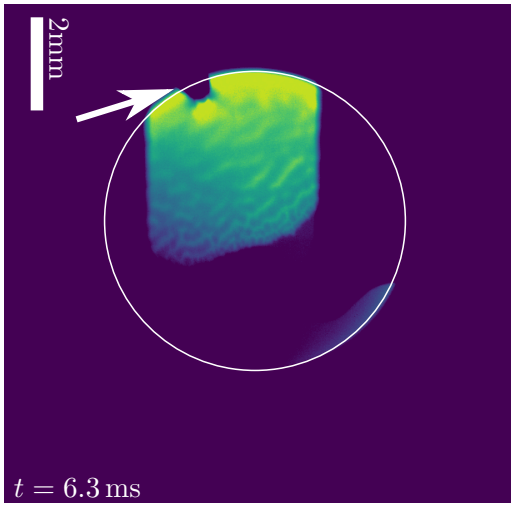

(a) Scaled front morphology during solidification initiated with a trigger needle.

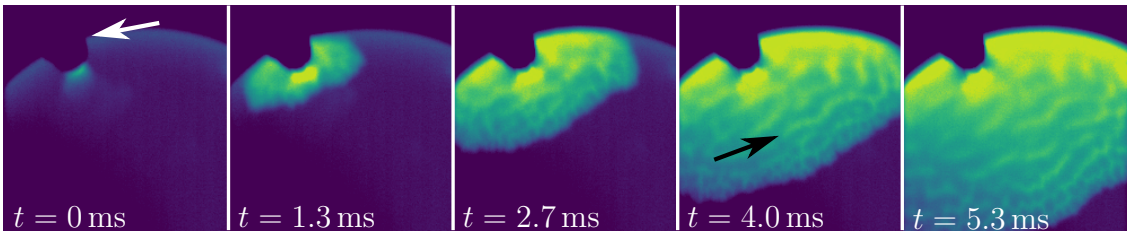

(b) Image sequence showing the propagation of the scaled front with stripes behind the front (black arrow).

Figure 4.30: Scaled front morphology exhibiting stripes during solidification initiated at an undercooling of $\Delta T = 191\,\mathrm{K}$ using the trigger needle (white arrow).

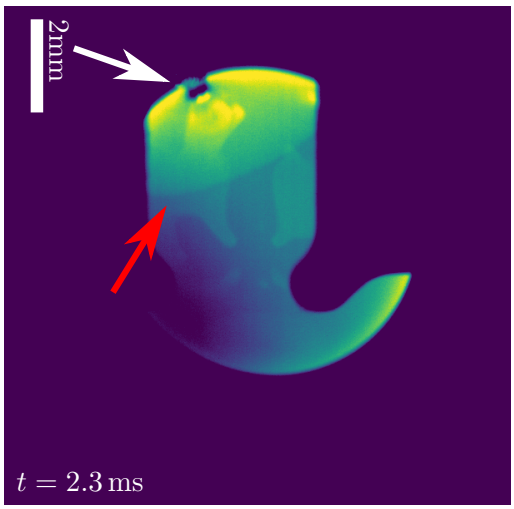

Figure 4.31: Plane front (red arrow) during solidification initiated by triggering (white arrow) at an undercooling of $\Delta T = 142\,\mathrm{K}$.

stripes are similar to the wavy front morphology observed in Al-28.5at.%Ni, see Subsection 4.2.2.

Although rapid solidification initiated by the trigger needle is so fast that the trigger needle has no possibility to penetrate the sample, the needle can still collect constituents of the sample material either when touching the sample during a triggering event or by condensation of evaporated metals leading to sticking of the sample to the trigger needle. The collection of sample material is more likely to happen at low undercoolings as the large fraction not solidifying facilitates the collection of constituents of the sample material by the trigger needle. Considering that the sample gradually sticks more and more to the trigger needle, when more cycles using triggering are carried out, the number of possible trigger cycles is limited.

During one cycle using the trigger needle to initiate solidification, the front morphology differed from the previous two, it was planar, see Fig. 4.31. The white arrow denotes the trigger needle while the red arrow marks the front position. It is the same front morphology as found for Al-28.5at.%Ni, see Subsection 4.2.2.

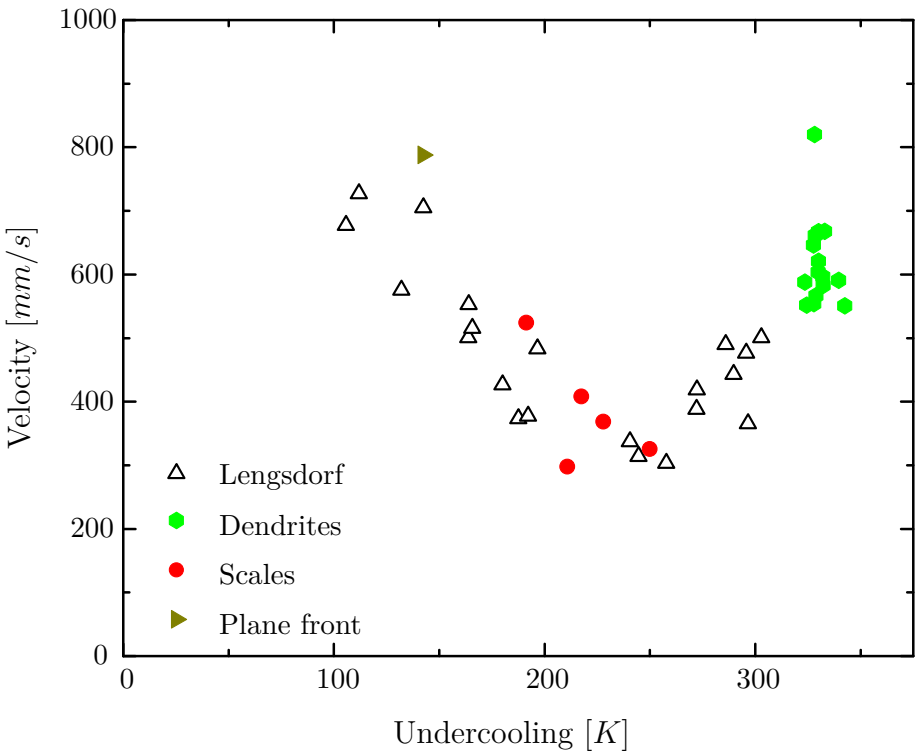

Figure 4.32: Al-35at.%Ni velocity-vs.-undercooling relationship from microgravity in comparison with previous measurements by Lengsdorf et al. [5] showing different front morphologies in separated undercooling ranges.

4.3.3 Velocity-vs.-undercooling relationship measured in microgravity

From the high-speed videos, the growth velocity of the front was determined by using the method described in Subsection 4.1.3. The result in Fig. 4.32 shows the results by Lengsdorf et al. [5] as well as the new results obtained in microgravity. The velocity was measured in the range of $100\,\mathrm{K} < \Delta T < 350\,\mathrm{K}$. The previous data show decreasing front velocities for undercoolings smaller than $\Delta T \approx 250\,\mathrm{K}$. At larger undercoolings, the velocity increases.

The new data below $\Delta T \approx 250\,\mathrm{K}$ reproduce the previously measured trend well. At larger undercoolings, the new data extend the observed trend by enlarging the range of measured undercoolings by approximately 50 K. However, at the deepest undercoolings, the values show a quite large scatter.

In parallel to the previous results, the classification of the front morphologies for the undercoolings was carried out. At the lowest undercooling, $\Delta T = 142\,\mathrm{K}$, a plane front was observed (brown triangle). For undercoolings up to the minimum of the curve at $\Delta T \approx 250\,\mathrm{K}$, scales (red circles) were found. At the highest undercoolings, $\Delta T > 300\,\mathrm{K}$, the dendritic morphology (green diamonds) was seen.

4.3.4 Analysis of number and distances of scales in microgravity

As the experiments were also carried out on board the ISS, the number of scales and the distance between scale centres and their nearest neighbours is analysed. The procedure is shortly described and followed by the results of the analysis.

Short description of the analysis procedure

Fig. 4.33 shows an exemplary analysis of an experimental run with the Al-35at.%Ni alloy. In Fig. 4.33 (a) selected scales are marked by green dots. The experiments were conducted using the exact same experimental setup on board the ISS as for the Al-25at.%Ni alloy with the same magnification in the high-speed video data. A first measurement of the scale distances in the Al-35at.%Ni alloy shows scale distances in the range of $d = 0.2$ to 0.6 mm, which is distinctly smaller than for the Al-25at.%Ni alloy with scale distances of $d = 0.3$ up to 1.5 mm. Due to these small scale distances corresponding to small scale radii in the Al-35at.%Ni alloy, the scale outlines were not analysed.

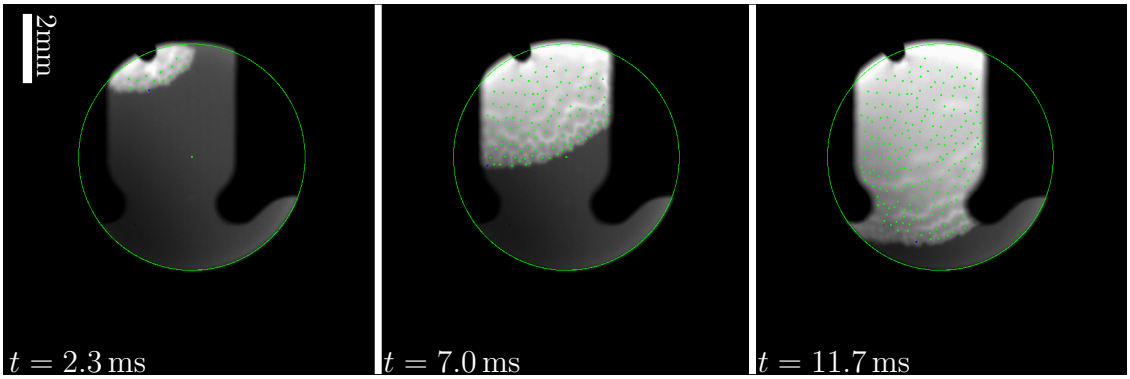

(a) Manually marked scales

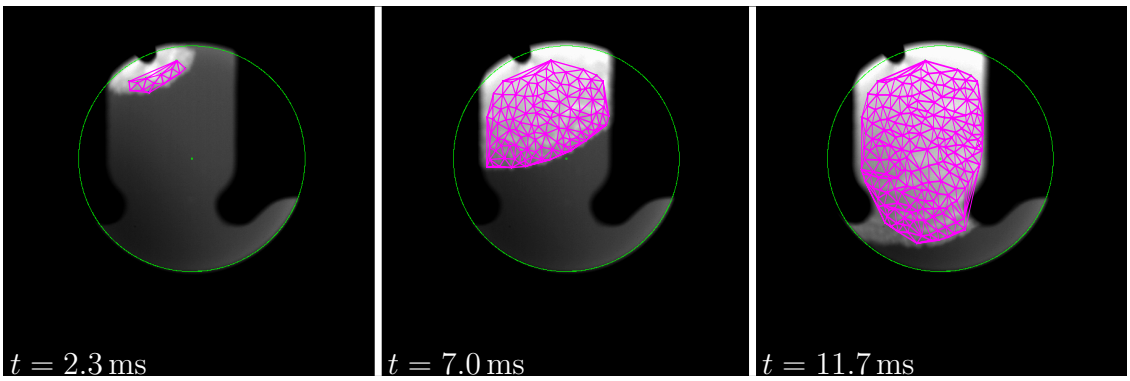

(b) Determination of nearest neighbours via Delaunay triangulation

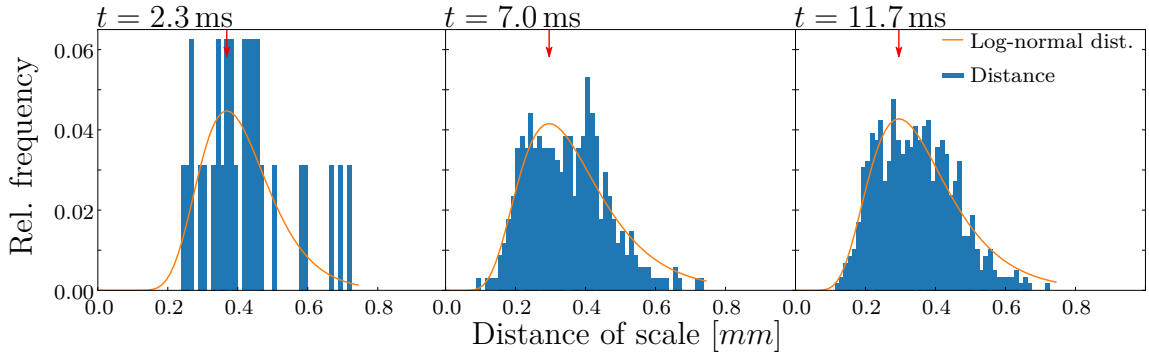

(c) Scale distance distribution function

Figure 4.33: The three step analysis procedure (similar to Fig. 4.6) for the analysis of the number of scales and scale distance to nearest neighbours: (a) marking of the scales; (b) Delaunay triangulation to find adjacent scales; (c) sorting the scale distances into a histogram with bin size of 0.0125 mm and a cut-off at $d = 0.75\,\mathrm{mm}$, fitting a log-normal distribution and determining the peak position.

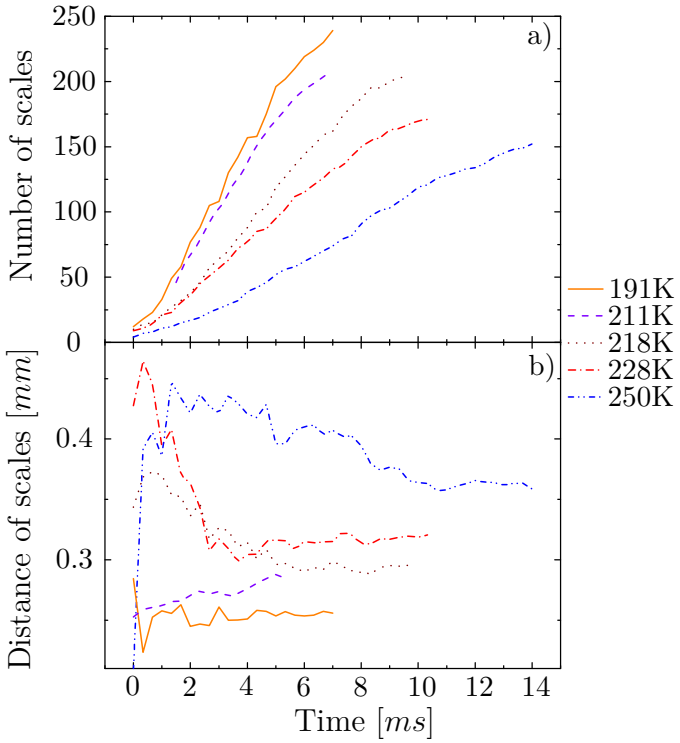

Figure 4.34: Results from the experiments in microgravity: number of scales increases linearly while the scale distance shows an initial transient before reaching a constant value.

The network of nearest neighbouring scales in Fig. 4.33 (b) shows the same artefacts of false classifications at its outline or the sample holder as already described in Subsection 4.1.4. Therefore, to determine the relative frequency of the scale distances, a cut-off at $d \geq 0.75\,\text{mm}$ is used. The bin size was set to 0.0125 mm.

The relative frequency of the scale distances in Fig. 4.33 (c) at $t = 2.3\,\text{ms}$ is sparsely filled with 32 distances of 14 scales. After $\Delta t = 4.7\,\text{ms}$, already 347 scale distances of 119 scales are analysed for the respective histogram. The last histogram contains the distances between 209 scales, i.e. 588 scale distances. This strong increase of the number of scale distances can be nicely seen as the histograms become more populated over time. As the results for the Al-25at.%Ni alloy before, see Fig. 4.6 (c), the histogram develops a tail to the right side of larger scale distances at $t \geq 7\,\text{ms}$ in Fig. 4.33 (c). The log-normal distribution which was used to find the most often appearing scale distance fits the histogram nicely.

The number and distances of scales

A synopsis of the results of the analysis of scale distances is shown in Fig. 4.34. The scales were not visible directly from the beginning of solidification, thus the curves do not start at zero. The first image which showed distinct scales was set as $t = 0\,\mathrm{ms}$ for this plot.

One cycle at $\Delta T = 211\,\mathrm{K}$ showed the end of solidification. To fit this into the graph for the number of scales, Fig. 4.34(a), this cycle was extrapolated to zero scales. The end of solidification is interpreted with caution (see Subsection 4.1.4, Fig. 4.6) although in this case the results fit to the trend as described below.

All the curves for the number of scales show the same behaviour. At the beginning they all have a transient regime, where the slope increases. Afterwards the curves are essentially linear, and close to the end the slope decreases. The slope of the curves strongly depends on the undercooling. Higher undercoolings feature a lower slope, meaning that fewer scales form per time unit at higher undercoolings. The curve that showed mostly the end of solidification ($\Delta T = 211\,\mathrm{K}$) also follows this trend.

Regarding the distances gained from the fit of the log-normal distribution, and initial transient can be distinguished from the steady state. After the initial transient, the curves attain a constant value. Although the curve for $\Delta T = 211\,\mathrm{K}$ shows a slow increase over the entire available measurement time, the scale distance follows again the trend observed for Al-25at.%Ni, see Subsection 4.1.4, where the scale distance increases with increasing undercooling.

4.3.5 Discussion

During the processing of this alloy in microgravity, the previous results for the velocity-vs.-undercooling relation obtained by Lengsdorf et al. [5] were reproduced for the anomaly, while the undercooling range was extended by $\approx 50\,\mathrm{K}$. During some cycles, the trigger was successfully used to control the nucleation undercooling. The trigger once initiated the growth of a plane front. The plane front morphology was observed at the lowest undercooling, similar as for Al-28.5at.%Ni. At increased undercoolings, the trigger initiated the scaled morphology. Again, the velocity decreases for increasing undercooling. In analogy to Al-25at.%Ni and Al-28.5at.%Ni, the scaled morphology was only observed in the range of the decreasing velocities, which is explained by a nucleation front propagating along the sample surface.

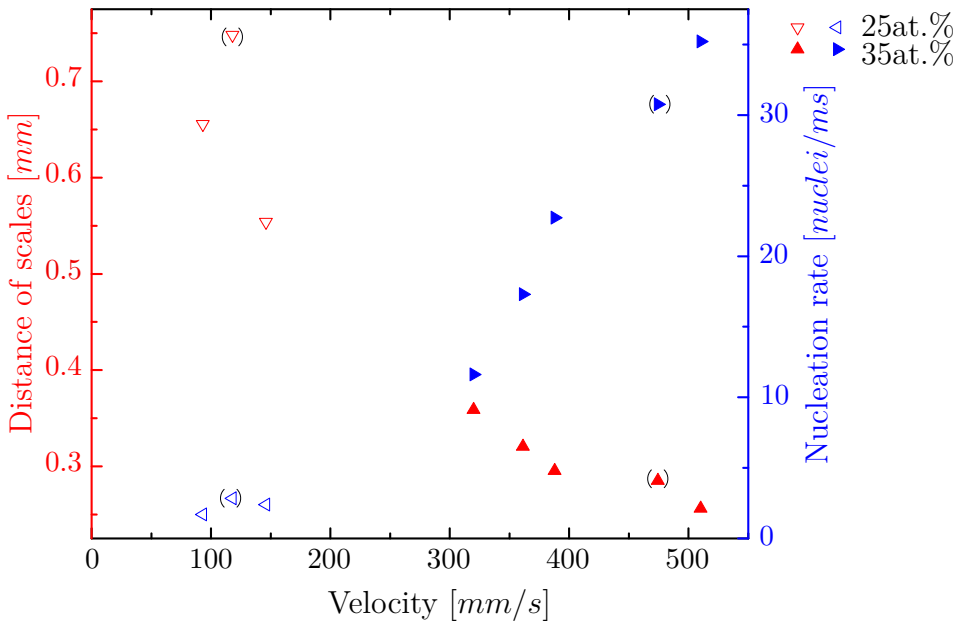

Figure 4.35: Results from the analysis of the scale distance and the nucleation rate, i.e. the slope of the curve of the number of scales, for Al-25at.%Ni and Al-35at.%Ni. The decreasing growth velocity is due to the decreasing nucleation rate.

The analysis of the number of scales and scale distances was carried out for Al-35at.%Ni, too. The Al-35at.%Ni alloy showed $\gtrsim 150$ scales, whereas for the Al-25at.%Ni alloy $\lesssim 100$ scales were observed. Because the statistics of this analysis was thus distinctly improved, the trend that the nucleation rate, i.e. the slope of the number of scales, decreases and the distance between the scale centres increases with increasing undercooling can be seen more clearly, see Fig. 4.35, directly verifying the idea by Paul [72].

Fig. 4.35 depicts the analysis results of the scale distances and nucleation rates for the Al-25at.%Ni and Al-35at.%Ni alloys against the measured velocity. An increasing velocity corresponds to a decreasing undercooling. The values in brackets correspond to cycles where the initial point of nucleation was not in the field of view of the camera, and only the end of solidification was observed. Fig. 4.35 demonstrates that the same trends of decreasing nucleation rate and increasing scale distances with increasing undercooling are present in the Al-25at.%Ni and Al-35at.%Ni alloys. It is therefore concluded that the same mechanism responsible for the nucleation front acts in these two alloys. Thus, the decreasing front velocity is due to the decrease of the nucleation rate as the increasing scale distance

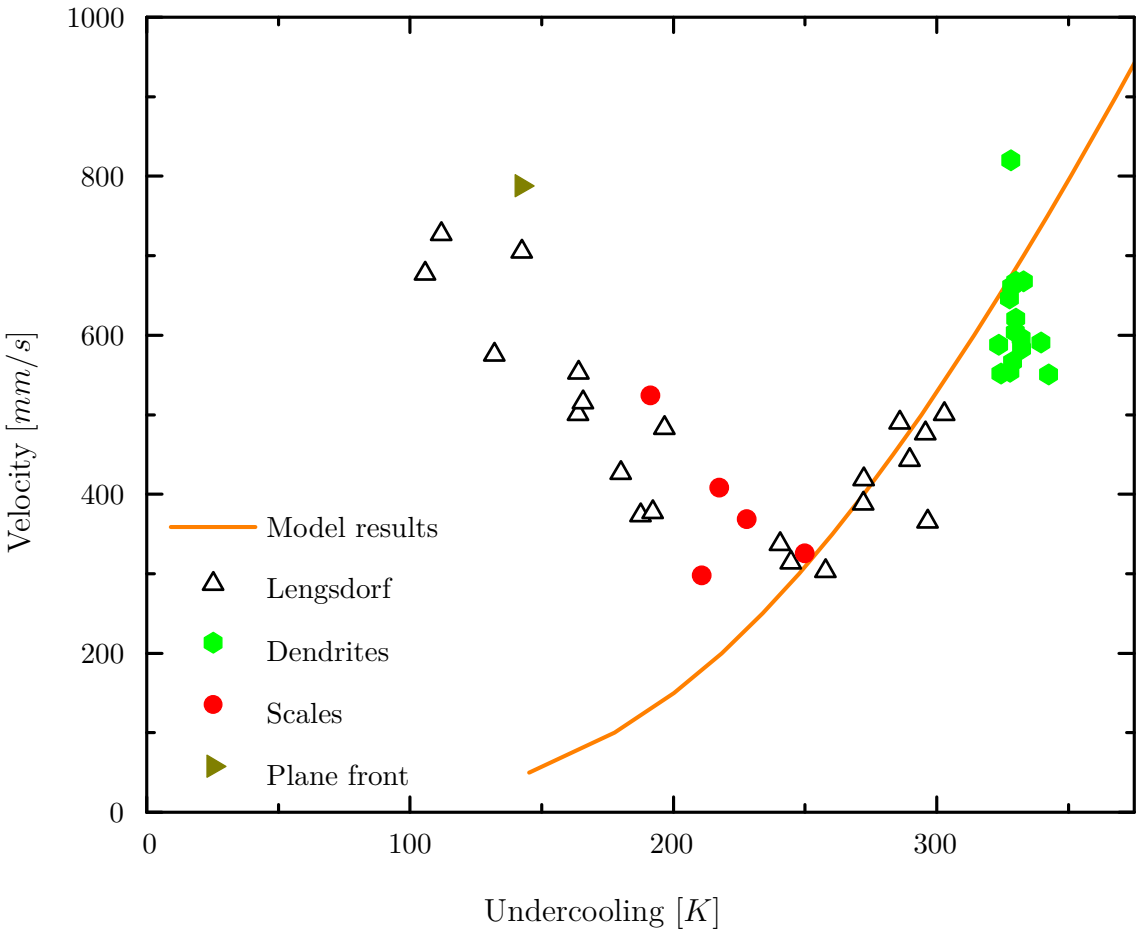

Figure 4.36: Using the sharp interface model [62] to calculate the growth velocity in Al-35at.%Ni shows that the branch featuring the positive slope is nicely reproduced by the model results.

(and radius) are not able to compensate for the fewer scales. However, the mechanism which leads to the nucleation in the vicinity of the existing solid remains unidentified.

For deeper undercoolings $\Delta T > 250\,\mathrm{K}$, the front velocity does not show the anomalous behaviour, but rather the expected velocity increase with increasing undercooling. At the same time, the front morphology changes from scaled to dendritic. In contrast to the Al-25at.%Ni alloy, where no increasing velocity was measured for the dendritic morphology, this systematic change of morphology and slope is described in the Al-35at.%Ni alloy for the first time. Therefore, the used analysis method, see Subsection 4.1.3, should allow to measure the correct dendrite growth velocity. Fig. 4.36 includes velocities calculated with a sharp-interface model [62, 64], solid line. The calculations reproduce the branch of positive slope which

was observed in both the old and the new measurements. It is therefore concluded that the branch with positive slope shows the expected growth behaviour.

In contrast to the other examined Al-Ni alloys, Al-35at.%Ni shows a minimum in the velocity-vs.-undercooling relation at $\Delta T \approx 250\,\mathrm{K}$ which is still poorly understood. The change of the slope may relate to hypercooling. For a congruently melting system, a temperature independent specific heat capacity in the undercooled melt and adiabatic solidification, see Subsection 4.1.1, Eq. (4.1) can be used to calculate the hypercooling limit. Also the strong segregation in Al-Ni alloys needs to be neglected. Using $\Delta H_f = 8833\,\mathrm{J\,mol^{-1}}$ and $c_p^l = 35.7\,\mathrm{J\,mol^{-1}\,K^{-1}}$ a hypercooling limit of $\Delta T_{\mathrm{hyp}} = 247\,\mathrm{K}$ is calculated. ΔH_f and c_p^l are taken from [113] and calculated using the ThermoCalc Software [86]. The position of the minimum thus coincides with the hypercooling limit for the Al-35at.%Ni alloy.

Experiments with binary metallic melts solidifying under hypercooling conditions showed dendritic microstructures [114]. As the highest growth velocities observed in the Al-35at.%Ni alloy are $v < 1\,\mathrm{m\,s^{-1}}$, it is unlikely that the limit of absolute stability is reached. The limit of absolute stability leading to plane front solidification requires velocities $v > v_{\mathrm{abs}}$ where v_{abs} is given by [115]

$$v_{\mathrm{abs}} = \frac{\alpha}{\Gamma}\Delta T, \tag{4.9}$$

with the thermal diffusivity in the melt α and the Gibbs-Thomson-coefficient Γ. Using the values provided in [70], $\alpha = 9.5 \times 10^{-6}\,\mathrm{m^2\,s^{-1}}$ and $\Gamma = 2.7 \times 10^{-7}\,\mathrm{K\,m}$, the limit of absolute stability is in the order of $V_{\mathrm{abs}}\,(350\,\mathrm{K}) \approx 12\,\mathrm{km\,s^{-1}}$ which is distinctly faster than the velocities observed here. Therefore, dendrites are the expected growth morphology.

The different front morphologies observed in this thesis, plane front, scales, dendrites can now be attributed to different sections of a front velocity-vs.-undercooling curve and different solidification mechanisms, see Fig. 4.37. The wavy front morphology is attributed to be also the scaled front morphology, as it is observed in the Al-35at.%Ni alloy, that the characteristic stripes for the wavy morphology, are due to blurred scale outlines. Although no data were recorded for the lowest undercoolings close to $\Delta T = 0\,\mathrm{K}$, blue dashed line, it is suggested that in this range the front is plane because it only occured at the lowest undercoolings. This plane front is the intersection of the two spheres, one representing the envelope of dendrites and the other representing the sample surface (similar to [93]). The shape of the curve

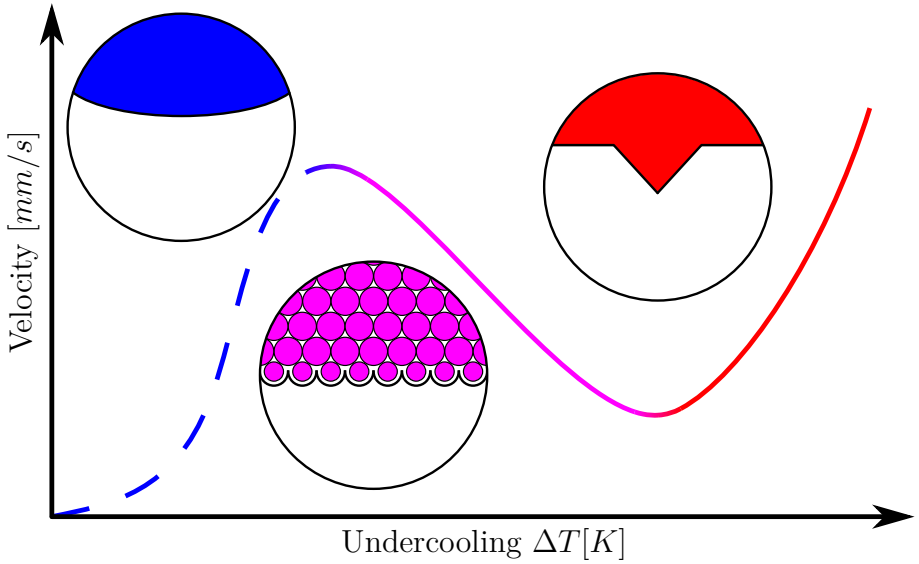

Figure 4.37: Suggested front velocity-vs.-undercooling curve: plane and dendritic front correspond to increasing front velocities while the scaled morphology corresponds to a decreasing front velocity.

starts at $v\,(\Delta T = 0\,\mathrm{K}) = 0\,\mathrm{m\,s^{-1}}$ and increases up to the point where the scales form, because the plane front belongs to the expected velocity increase [89]. This shape of the curve is also supported by velocity measurements in Al-31.5at.%Ni carried out by [23] showing an increasing velocity in the range of $\Delta T = 50$ to 100 K. At undercoolings larger than the undercooling at the minimum, the observed dendritic front shows the trend predicted by theory, see Fig. 4.32. In these two regions, determinations of the front velocity should allow determinations of the dendrite growth velocity.

However, in-between the two regions of the expected velocity trend in Fig. 4.37, the new growth mechanism for scales takes over and governs solidification. This shows that the assumption of a spherical outline of the growth front for the velocity analysis of Al-Ni alloys, used in [4, 5] and in the velocity analysis carried out here, is not valid, and the front velocity does not correlate with the dendrite growth velocity. It is suggested that the dendrite growth velocity is distinctly smaller than the nucleation front velocity up to the minimum. This is implied by the microstructure analysis which shows dendrites growing radially inwards.

CHAPTER 5

Conclusion

In this thesis, experiments for the rapid solidification of Al-Ni alloys under gravity and microgravity conditions were carried out. The main objective of these experiments was the study of the growth anomaly in the Al-Ni alloys. In previous experiments a decreasing growth velocity with increasing undercooling has been observed in Al-Ni alloys [4, 5]. From theoretical considerations an increasing growth velocity with increasing undercooling is expected [2, 3, 88].

The experiments in microgravity using the EML on board the ISS show the same velocity-vs.-undercooling relation as the previous terrestrial experiments. However, the high-speed video data obtained during the first recalescence provide new information about the front morphology as different morphologies were observed: planar, scaled and dendritic front morphologies. The planar front morphology was observed at the lowest undercoolings. It is important to note that this plane front corresponds to the intersection of the sphere representing the envelope of the growing dendrites with the sphere representing the sample surface [91–93]. This assumption of a spherical envelope is the basis for the velocity analysis [91–93].

At larger undercoolings, a scaled morphology was observed. This front morphology is build by circular features, so called scales. The scales form in the vicinity of the already existing solid. As the scales are able to grow, the front motion is a superposition of the formation of new scales and the growth of the existing ones. In microstructure analyses of samples processed on earth, which showed the scaled front during solidification, dendrites extending from the sample surface were found. It is concluded that the nucleation takes place on the surface, and that each

scale corresponds to a nucleation event. The observed front is thus not a dendritic growth front, but rather a nucleation front propagating along the sample surface. Therefore, the assumption of the spherical envelope is not met, and the used velocity analysis method is not applicable. As this scaled morphology corresponds to the branches of the velocity-vs.-undercooling relation exhibiting the negative slope, the finding of the nucleation front is able to resolve the contradiction between theoretical expectations for a dendritic growth front and the experimental results measured for a nucleation front. Besides the explanation using the nucleation front, forced convection, inverse melting and varying fractions of solidifying phases were discussed, but ruled out here.

Analyses of the number of scales, scale sizes and distances show that the number of scales decreases with increasing undercooling, while the scale sizes and distances increase. The negative trend of the velocity-vs.-undercooling relation can hence be explained by the decreasing nucleation rate. Although the scales are larger, the loss of scales cannot be compensated.

Microstructure analyses show a dendritic structure. In the Al-25at.%Ni and Al-28.5at.%Ni alloy, dendrite arms meeting at the sample centre were found in some samples. As the dendrite growth velocity cannot be measured if the front is scaled, the microstructure results allow to give at least an order of magnitude for the dendrite growth velocity [106]. If the dendrite growth velocity would be close to the front velocity, the meeting point of the dendrites would be shifted closer to the last points of nucleation. However, they intersect at the sample centre indicating a distinctly slower dendrite growth velocity.

The third morphology observed during the experiments using the ISS-EML to investigate the Al-25at.%Ni and Al-35at.%Ni, is a dendritic morphology. This morphology is found at the largest undercoolings. In the Al-35at.%Ni alloy, a minimum in the velocity-vs.-undercooling relation is measured. A dendritic morphology is observed for the branch featuring the increasing growth velocities corresponding to the expected behaviour. This leads to the conclusion that for undercoolings larger than the minimum, the expected growth behaviour is observed.

Bibliography

[1] Herlach, D. M., Galenko, P. K. and Holland-Moritz, D. *Metastable solids from undercooled melts*. Pergamon materials series (Elsevier, Amsterdam and London, 2007).

[2] Galenko, P. K. and Danilov, D. A. *Selection of the dynamically stable regime of rapid solidification front motion in an isothermal binary alloy*. Journal of Crystal Growth **216**, 512–526 (2000).

[3] Reuther, K., Galenko, P. K. and Rettenmayr, M. *Dynamic instability of the steady state of a planar front during non-equilibrium solidification of binary alloys*. Journal of Crystal Growth **506**, 55–60 (2019).

[4] Lengsdorf, R., Galenko, P. K. and Herlach, D. M. Measurement of dendrite growth on al-ni alloys in reduced gravity. In Lacoste, H. (ed.) *European rocket and balloon programmes and related research*, ESA SP (ESA Communication Production Off, Noordwijk, 2009).

[5] Lengsdorf, R., Holland-Moritz, D. and Herlach, D. M. *Anomalous dendrite growth in undercooled melts of Al–Ni alloys in relation to results obtained in reduced gravity*. Scripta Materialia **62**, 365–367 (2010).

[6] Volmer, M. and Weber, t. *Keimbildung in übersättigten Gebilden*. Zeitschrift für Physikalische Chemie **119U** (1926).

[7] Becker, R. and Döring, W. *Kinetische Behandlung der Keimbildung in übersättigten Dämpfen*. Annalen der Physik **416**, 719–752 (1935).

[8] Turnbull, D. and Fisher, J. C. *Rate of Nucleation in Condensed Systems.* The Journal of Chemical Physics **17**, 71–73 (1949).

[9] Fisher, J. C. *Errata: Rate of Nucleation in Condensed Systems.* The Journal of Chemical Physics **17**, 429 (1949).

[10] Volmer, M. *Über Keimbildung und Keimwirkung als Spezialfälle der heterogenen Katalyse.* Zeitschrift für Elektrochemie und angewandte physikalische Chemie **35**, 555–561 (1929).

[11] Turnbull, D. *Kinetics of Heterogeneous Nucleation.* The Journal of Chemical Physics **18**, 198–203 (1950).

[12] Klein, S. *Nucleation in undercooled melts of pure zirconium and zirconium based alloys.* Dissertation, Ruhr-Universität Bochum, Bochum (19.11.2010).

[13] Kobold, R. *Crystal growth in undercooled melts of glass forming Zr-based alloys.* Dissertation, Ruhr-Universität Bochum, Bochum (15.6.2016).

[14] Herlach, D. M., Palberg, T., Klassen, I., Klein, S. and Kobold, R. *Overview: Experimental studies of crystal nucleation: Metals and colloids.* The Journal of Chemical Physics **145**, 211703 (2016).

[15] Schenk, T., Holland-Moritz, D., Simonet, V., Bellissent, R. and Herlach, D. M. *Icosahedral short-range order in deeply undercooled metallic melts.* Physical Review Letters **89**, 075507 (2002).

[16] Kelton, K. F. et al. *First x-ray scattering studies on electrostatically levitated metallic liquids: demonstrated influence of local icosahedral order on the nucleation barrier.* Physical Review Letters **90**, 195504 (2003).

[17] Kelton, K. F., Greer, A. L., Herlach, D. M. and Holland-Moritz, D. *The Influence of Order on the Nucleation Barrier.* MRS Bulletin **29**, 940–944 (2004).

[18] Simonet, V. et al. *Local order and magnetism in liquid Al-Pd-Mn alloys.* Physical Review B **58**, 6273–6286 (1998).

[19] Simonet, V., Hippert, F., Audier, M. and Bellissent, R. *Local order in liquids forming quasicrystals and approximant phases.* Physical Review B **65**, 169 (2001).

[20] Reichert, H. et al. *Observation of five-fold local symmetry in liquid lead.* Nature **408**, 839–841 (2000).

[21] Notthoff, C., Feuerbacher, B., Franz, H., Herlach, D. M. and Holland-Moritz, D. *Direct determination of metastable phase diagram by synchrotron radiation experiments on undercooled metallic melts.* Physical Review Letters **86**, 1038–1041 (2001).

[22] Notthoff, C., Franz, H., Hanfland, M., Herlach, D. M., Holland-Moritz, D. and Petry, W. *Electromagnetic levitation apparatus for investigations of the phase selection in undercooled melts by energy-dispersive x-ray diffraction.* Scripta Materialia **71**, 3791 (2000).

[23] Shuleshova, O. *Equilibrium and metastable solidification in Ti-Al-Nb and Al-Ni systems.* Dissertation, Technische Universität Dresden, Dresden (14.12.2009). URL http://nbn-resolving.de/urn:nbn:de:bsz:14-qucosa-38636.

[24] Shuleshova, O., Holland-Moritz, D., Löser, W., Reinhart, G., Iles, G. N. and Büchner, B. *Metastable formation of decagonal quasicrystals during solidification of undercooled Al-Ni melts: In situ observations by synchrotron radiation.* Europhysics Letters **86**, 36002 (2009).

[25] Shuleshova, O., Holland-Moritz, D., Löser, W., Lindenkreuz, H.-G. and Büchner, B. *In situ observation of phase selection in undercooled Ni–Al melts.* International Journal of Cast Metals Research **22**, 286–289 (2013).

[26] Shuleshova, O., Löser, W., Holland-Moritz, D., Herlach, D. M. and Eckert, J. *Solidification and melting of high temperature materials: In situ observations by synchrotron radiation.* Journal of Materials Science **47**, 4497–4513 (2012).

[27] Löser, W., Shuleshova, O., Lindenkreuz, H.-G. and Büchner, B. Melt undercooling experiments for raney-ni type ni-50wt.%al alloys. In Jones, H. (ed.) *Solidification processing 2007* (Dep. of Engineering Materials the Univ. of Sheffield, Sheffield, 2007).

[28] Shuleshova, O. et al. *In situ observations of solidification processes in γ-TiAl alloys by synchrotron radiation.* Acta Materialia **58**, 2408–2418 (2010).

[29] Turnbull, D. *Under what conditions can a glass be formed?* Contemporary Physics **10**, 473–488 (1969).

[30] Skripov, V. P. *Homogeneous nucleation in melts and amorphous films.* Curr. Top. Mater. Sci. (Current Topics in Materials Science) **2**, 327–378 (1977).

[31] Skripov, V. P., Baidakov, V. G. and Kaverin, A. M. *Nucleation in superheated argon, krypton and xenon liquids.* Physica A: Statistical Mechanics and its Applications **95**, 169–180 (1979).

[32] Dantzig, J. A. and Rappaz, M. *Solidification.* Engineering sciences Materials (EPFL Press and CRC Press, Lausanne and Boca Raton, Fla., 2009), 1st ed. edn.

[33] Gránásy, L. et al. *Phase-field modeling of crystal nucleation in undercooled liquids – A review.* Progress in Materials Science **106**, 100569 (2019).

[34] Gránásy, L., Pusztai, T., Börzsönyi, T., Warren, J. A. and Douglas, J. F. *A general mechanism of polycrystalline growth.* Nature materials **3**, 645–650 (2004).

[35] Pusztai, T., Bortel, G. and Gránásy, L. *Phase field theory of polycrystalline solidification in three dimensions.* Europhysics Letters (EPL) **71**, 131–137 (2005).

[36] Gránásy, L., Pusztai, T., Tegze, G., Warren, J. A. and Douglas, J. F. *Growth and form of spherulites.* Physical review. E, Statistical, nonlinear, and soft matter physics **72**, 011605 (2005).

[37] Gránásy, L., Pusztai, T. and Warren, J. A. *Modelling polycrystalline solidification using phase field theory.* Journal of Physics: Condensed Matter **16**, R1205–R1235 (2004).

[38] Podmaniczky, F., Tóth, G. I., Tegze, G. and Gránásy, L. *Hydrodynamic theory of freezing: Nucleation and polycrystalline growth.* Physical review. E **95**, 052801 (2017).

[39] Shibuta, Y., Sakane, S., Miyoshi, E., Okita, S., Takaki, T. and Ohno, M. *Heterogeneity in homogeneous nucleation from billion-atom molecular dynamics simulation of solidification of pure metal.* Nature communications **8**, 10 (2017).

[40] Gránásy, L. et al. *Phase-Field Modeling of Polycrystalline Solidification: From Needle Crystals to Spherulites—A Review.* Metallurgical and Materials Transactions A **45**, 1694–1719 (2014).

[41] Bale, C. W. et al. *FactSage thermochemical software and databases, 2010–2016.* Calphad **54**, 35–53 (2016).

[42] Hughes, T., Lautenschlager, E. P., Cohen, J. B. and Brittain, J. O. *X-Ray Diffraction Investigation of β′-NiAl Alloys.* Journal of Applied Physics **42**, 3705–3716 (1971).

[43] Grushko, B. and Velikanova, T. Y. *Formation of Quasicrystals and Related Structures in Systems of Aluminum with Transition Metals. Part 1. Binary Systems Formed by Aluminum with 3d Metals.* Powder Metall. Metal Ceram. (Powder Metallurgy and Metal Ceramics) **43**, 72–86 (2004).

[44] Li, X. Z. and Kuo, K. H. *Decagonal quasicrystals with different periodicities along the tenfold axis in rapidly solidified Al-Ni alloys.* Philosophical Magazine Letters **58**, 167–171 (1988).

[45] Grushko, B. and Holland-Moritz, D. *High-Ni Al-Ni-Co decagonal phase.* Scripta Materialia **35**, 1141–1146 (1996).

[46] Pohla, C. and Ryder, P. L. *Quasicrystals in Al-Ni alloys.* Materials Science and Engineering: A **134**, 947–950 (1991).

[47] Pohla, C. and Ryder, P. *Crystalline and quasicrystalline phases in rapidly solidified Al-Ni alloys.* Acta Materialia **45**, 2155–2166 (1997).

[48] Gandin, C.-A., Tourret, D., Volkmann, T., Herlach, D. M., Ilbagi, A. and Henein, H. Solidification modeling: from electromagnetic levitation to atomization processing. In Herlach, D. M. (ed.) *Solidification of containerless undercooled melts* (Wiley-VCH, Weinheim, 2012).

[49] Tourret, D. and Gandin, C.-A. *A generalized segregation model for concurrent dendritic, peritectic and eutectic solidification.* Acta Materialia **57**, 2066–2079 (2009).

[50] Tourret, D., Gandin, C.-A., Volkmann, T. and Herlach, D. M. *Multiple non-equilibrium phase transformations: Modeling versus electro-magnetic levitation experiment.* Acta Materialia **59**, 4665–4677 (2011).

[51] Tourret, D. et al. *Gas atomization of Al–Ni powders: Solidification modeling and neutron diffraction analysis.* Acta Materialia **59**, 6658–6669 (2011).

[52] Ilbagi, A., Khatibi, P. D., Henein, H., Lengsdorf, R. and Herlach, D. M. *Effect of cooling rate on solidification of Al-Ni alloys.* Journal of Physics: Conference Series **327**, 012010 (2011).

[53] Ilbagi, A. et al. *Containerless Solidification and Characterization of Industrial Alloys (NEQUISOL).* Journal of Physics: Conference Series **327**, 012007 (2011).

[54] Ilbagi, A., Henein, H. and Phillion, A. B. *Phase quantification of impulse atomized Al68.5Ni31.5 alloy.* Journal of Materials Science **46**, 6235–6242 (2011).

[55] Ilbagi, A., Tourret, D., Henein, H. and Gandin, C.-A. *Neutron diffraction analysis and solidification modeling of Impulse-Atomized Al-36 wt%Ni.* IOP Conference Series: Materials Science and Engineering **33**, 012060 (2012).

[56] Ilbagi, A. and Henein, H. *3D Quantitative Characterization of Rapidly Solidified Al-36 Wt Pct Ni.* Metallurgical and Materials Transactions A **45**, 2152–2160 (2014).

[57] Zheng, B., Lin, Y., Zhou, Y. and Lavernia, E. J. *Gas Atomization of Amorphous Aluminum: Part I. Thermal Behavior Calculations.* Metallurgical and Materials Transactions B **40**, 768–778 (2009).

[58] Hyers, R. W., Matson, D. M., Kelton, K. F. and Rogers, J. R. *Convection in containerless processing.* Annals of the New York Academy of Sciences **1027**, 474–494 (2004).

[59] Reutzel, S., Hartmann, H., Galenko, P. K., Schneider, S. and Herlach, D. M. *Change of the kinetics of solidification and microstructure formation induced by convection in the Ni–Al system.* Applied Physics Letters **91**, 041913 (2007).

[60] Herlach, D. M. et al. *Solidification of Undercooled Melts of Al-Based Alloys on Earth and in Space.* JOM **69**, 1303–1310 (2017).

[61] Funke, O. et al. *Dendrite growth velocity in levitated undercooled nickel melts.* Journal of Crystal Growth **297**, 211–222 (2006).

[62] Galenko, P. K. and Danilov, D. A. *Model for free dendritic alloy growth under interfacial and bulk phase nonequilibrium conditions.* Journal of Crystal Growth **197**, 992–1002 (1999).

[63] Galenko, P. K. and Jou, D. *Rapid solidification as non-ergodic phenomenon.* Physics Reports **818**, 1–70 (2019).

[64] Galenko, P. K. and Danilov, D. A. *Local nonequilibrium effect on rapid dendritic growth in a binary alloy melt.* Physics Letters A **235**, 271–280 (1997).

[65] Eckler, K., Cochrane, R. F., Herlach, D. M., Feuerbacher, B. and Jurisch, M. *Evidence for a transition from diffusion-controlled to thermally controlled solidification in metallic alloys.* Physical Review B **45**, 5019–5022 (1992).

[66] Sahm, P. R., Egry, I. and Volkmann, T. (eds.) *Schmelze, Erstarrung, Grenzflächen: Eine Einführung in die Physik und Technologie flüssiger und fester Metalle* (Springer Berlin Heidelberg, Berlin, Heidelberg and s.l., 1999).

[67] Hartmann, H., Holland-Moritz, D., Galenko, P. K. and Herlach, D. M. *Evidence of the transition from ordered to disordered growth during rapid solidification of an intermetallic phase.* Europhysics Letters **87**, 40007 (2009).

[68] Wang, H., Herlach, D. M. and Liu, R. P. *Dendrite growth in Cu 50 Zr 50 glass-forming melts, thermodynamics vs. kinetics.* Europhysics Letters **105**, 36001 (2014).

[69] Galenko, P. K., Wonneberger, R., Koch, S., Ankudinov, V., Kharanzhevskiy, E. V. and Rettenmayr, M. *Bell-shaped "dendrite velocity-undercooling" relationship with an abrupt drop of solidification kinetics in glass forming Cu-Zr(-Ni) melts.* Journal of Crystal Growth **532**, 125411 (2020).

[70] Ehlen, G. J. and Herlach, D. M. *Investigation of solidification in undercooled Al-rich Al-Ni alloy systems.* IOP Conference Series: Materials Science and Engineering **33**, 012066 (2012).

[71] Ehlen, G. J., Wang, H. and Herlach, D. M. *Concentration Dependent Growth Velocities in Undercooled Al-Rich Al-Ni Alloy Systems.* Materials Science Forum **790-791**, 485–490 (2014).

[72] Paul, P. *Experimentelle Untersuchung von Erstarrungsvorgängen in unterkühlten Aluminium-Nickel- und Aluminium-Eisen-Legierungen.* Masterarbeit, Friedrich-Schiller-Universität Jena, Jena (2.3.2018).

[73] Boden, S., Eckert, S., Willers, B. and Gerbeth, G. *X-Ray Radioscopic Visualization of the Solutal Convection during Solidification of a Ga-30 Wt Pct In Alloy.* Metallurgical and Materials Transactions A **39**, 613–623 (2008).

[74] Nguyen-Thi, H. et al. *Investigation of gravity effects on solidification of binary alloys with in situ X-ray radiography on earth and in microgravity environment.* Journal of Physics: Conference Series **327**, 012012 (2011).

[75] Hyers, R. W. *Fluid flow effects in levitated droplets.* Measurement Science and Technology **16**, 394–401 (2005).

[76] Hyers, R. W., Trapaga, G. and Abedian, B. *Laminar-turbulent transition in an electromagnetically levitated droplet.* Metallurgical and Materials Transactions B **34**, 29–36 (2003).

[77] Jeong, J. H., Goldenfeld, N. and Dantzig, J. A. *Phase field model for three-dimensional dendritic growth with fluid flow.* Physical review. E, Statistical, nonlinear, and soft matter physics **64**, 041602 (2001).

[78] Herlach, D. M. *Crystal nucleation and dendrite growth of metastable phases in undercooled melts.* Journal of Alloys and Compounds **509**, S13–S17 (2011).

[79] Galenko, P. K., Funke, O., Wang, J. and Herlach, D. M. *Kinetics of dendritic growth under the influence of convective flow in solidification of undercooled droplets.* Materials Science and Engineering: A **375-377**, 488–492 (2004).

[80] Galenko, P. K., Binder, S. and Ehlen, G. J. Forced flow effect on dendritic growth kinetics in a binary nonisothermal system. In Herlach, D. M. and Matson, D. M. (eds.) *Solidification of Containerless Undercooled Melts*, vol. 21, 349–362 (Wiley-VCH Verlag GmbH & Co. KGaA, Weinheim, Germany, 2012).

[81] Egry, I. and Voss, D. *Present Activities of the Investigators Working Group (IWG) for the Electromagnetic Levitator (EML) on ISS-A Status Report.* International Journal of Microgravity Science and Application **27**, 178–182 (2010).

[82] Seidel, A., Soellner, W. and Stenzel, C. *EML - an electromagnetic levitator for the International Space Station.* Journal of Physics: Conference Series **327**, 012057 (2011).

[83] Seidel, A., Soellner, W. and Stenzel, C. *Materials science investigations using electromagnetic levitation.* Journal of Physics: Conference Series **327**, 012015 (2011).

[84] Soellner, W., Seidel, A., Stenzel, C., Dreier, W. and Glaubitz, B. *EML-Containerless Processing Facility for Materials Science Research Onboard the ISS.* International Journal of Microgravity Science and Application **27**, 183–189 (2010).

[85] Gandin, C.-A., Mosbah, S., Volkmann, T. and Herlach, D. M. *Experimental and numerical modeling of equiaxed solidification in metallic alloys.* Acta Materialia **56**, 3023–3035 (2008).

[86] Andersson, J.-O., Helander, T., Höglund, L., Shi, P. and Sundman, B. *Thermo-Calc & DICTRA, computational tools for materials science.* Calphad **26**, 273–312 (2002).

[87] Herlach, D. M., Karrasch, C. and Burggraf, S. *EML-ADP-GSP-FS-02-1-0.*

[88] Herlach, D. M. et al. *Dendrite growth in undercooled Al-rich Al-Ni melts measured on Earth and in Space.* Physical Review Materials **3**, 073402 (2019).

[89] Volkmann, T. Measurements of crystal growth velocities in undercooled melts of metals. In Herlach, D. M. and Matson, D. M. (eds.) *Solidification of Containerless Undercooled Melts*, vol. 48, 239–259 (Wiley-VCH Verlag GmbH & Co. KGaA, Weinheim, Germany, 2012).

[90] Binder, S. *Undercooling and solidification of tetragonal Ni2B under different convective flow conditions.* Dissertation, Ruhr-Universität Bochum, Bochum (27.01.2011).

[91] Karrasch, C. *Solidification kinetics in undercooled pure iron and iron-boron alloys under different fluid flow conditions.* Dissertation, Ruhr-Universität Bochum, Bochum (2016).

[92] Gegner, J. *ftt - front tracking tool* (2013). Institut für Materialphysik im Weltraum, Deutsches Zentrum für Luft- und Raumfahrt, Köln.

[93] Assadi, H., Reutzel, S. and Herlach, D. M. *Kinetics of solidification of B2 intermetallic phase in the Ni–Al system.* Acta Materialia **54**, 2793–2800 (2006).

[94] Pericleous, K., Bojarevics, V. and Roy, A. *Modeling of EML in Combined AC/DC Magnetic Fields as the Basis for Microgravity Experiments.* International Journal of Microgravity Science and Application **30**, 56–63 (2013).

[95] Gottstein, G. *Materialwissenschaft und Werkstofftechnik: Physikalische Grundlagen.* Springer-Lehrbuch (Springer Vieweg, Berlin, 2014), 4., neu bearb. aufl. 2014 edn.

[96] Glassbrenner, C. J. and Slack, G. A. *Thermal Conductivity of Silicon and Germanium from 3K to the Melting Point.* Physical Review **134**, A1058–A1069 (1964).

[97] Hillert, M., Schwind, M. and Selleby, M. *Trapping of vacancies by rapid solidification.* Acta Materialia **50**, 3285–3293 (2002).

[98] Zheng, X. Q., Yang, Y., Gao, Y. F., Hoyt, J. J., Asta, M. and Sun, D. Y. *Disorder trapping during crystallization of the B2-ordered NiAl compound.* Physical review. E, Statistical, nonlinear, and soft matter physics **85**, 041601 (2012).

[99] Galenko, P. K., Reuther, K., Kazak, O. V., Alexandrov, D. V. and Rettenmayr, M. *Effect of convective transport on dendritic crystal growth from pure and alloy melts.* Applied Physics Letters **111**, 031602 (2017).

[100] Galenko, P. K., Herlach, D. M., Funke, O. and Phanikumar, G. Phase-field modeling of dendritic solidification in undercooled droplets. In Vincenzini, P. and Lami, A. (eds.) *Computational modeling and simulation of materials III*, Advances in science and technology, 565–572 (Techna Group, Faenza, 2004).

[101] Gao, J., Han, M., Kao, A., Pericleous, K., Alexandrov, D. V. and Galenko, P. K. *Dendritic growth velocities in an undercooled melt of pure nickel under static magnetic fields: A test of theory with convection.* Acta Materialia **103**, 184–191 (2016).

[102] Bracker, G. et al. Modeling of fluid flow effects on experiments using electromagnetic levitation in reduced gravity. In Lambotte, G., Lee, J., Allanore, A. and Wagstaff, S. (eds.) *Materials Processing Fundamentals 2019*, 171–180 (Springer International Publishing, Cham, 2019).

[103] Greer, A. L. *The thermodynamics of inverse melting.* Journal of the Less Common Metals **140**, 327–334 (1988).

[104] Blatter, A. and von Allmen, M. *Reversible amorphization in laser-quenched titanium alloys.* Physical Review Letters **54**, 2103–2106 (1985).

[105] Zhang, G., An, Q. and Goddard, W. A. *Composition Dependence of Glass Forming Propensity in Al−Ni Alloys.* The Journal of Physical Chemistry C **115**, 2320–2331 (2011).

[106] Mullis, A. M. *ISS Report: personal communication* (14.08.2019).

[107] Wang, F. E. *Transformation Twinning of B 2(CsCl)–Type Structure Based on an Inhomogeneous Shear Model.* Journal of Applied Physics **43**, 92–97 (1972).

[108] Wasilewski, R. J. *Comment on "Transformation twinning of B 2(CsCl)–type structure based on an inhomogeneous shear model".* Journal of Applied Physics **43**, 3599–3600 (1972).

[109] Wang, F. E. *Reply to "Comment on Transformation twinning of B 2(CsCl)–type structure based on an Inhomogeneous shear model' ".* Journal of Applied Physics **43**, 3600 (1972).

[110] Bradley, A. J. and Taylor, A. *The crystal structures of Ni_2Al_3 and $NiAl_3$.* The London, Edinburgh, and Dublin Philosophical Magazine and Journal of Science **23**, 1049–1067 (1937).

[111] Jäger, A., Ostapovets, A., Molnár, P. and Lejček, P. $\left\{10\bar{1}2\right\}-\left\{10\bar{1}2\right\}$ *Double twinning in magnesium.* Philosophical Magazine Letters **91**, 537–544 (2011).

[112] Ostapovets, A. and Molnár, P. *On the relationship between the "shuffling-dominated" and "shear-dominated" mechanisms for* $\left\{10\bar{1}2\right\}$ *twinning in magnesium.* Scripta Materialia **69**, 287–290 (2013).

[113] Herlach, D. M., Karrasch, C. and Burggraf, S. *EML-ADP-GSP-FS-24-1-0.*

[114] Wilde, G., Görler, G. P. and Willnecker, R. *Hypercooling of completely miscible alloys.* Applied Physics Letters **69**, 2995–2997 (1996).

[115] Galenko, P. K. and Danilov, D. A. *Linear morphological stability analysis of the solid-liquid interface in rapid solidification of a binary system.* Physical review. E, Statistical, nonlinear, and soft matter physics **69**, 051608 (2004).

Konferenzen und Publikationen

Konferenzen

- M. Reinartz, S. Burggraf, M. Rettenmayr, D. M. Herlach, *Rapid Solidification of Aluminum-Nickel Melts in Earth and Space Environment*, 6^th Decennial International Conference on Solidification Processing, 25.-28. Juli 2017, Old Windsor, GB (Poster)

- F. Kargl, M. Reinartz, *Morphological Transitions: In-situ Observation of Equiaxed Growth in Al-Zn Alloys*, 6^th Decennial International Conference on Solidification Processing, 25.-28. Juli 2017, Old Windsor, GB (Poster)

- D. M. Herlach, M. Kolbe, M. Reinartz, P. K. Galenko, M. Rettenmayr, *Anomalous dendrite growth in undercooled melts of Al-Ni alloys*, 147^{th} TMS Annual Meeting & Exhibition 2018, 11.-15. März 2018, Phoenix, Arizona, USA (Vortrag)

- G. Bracker, Y. Luo, B. Damaschke, K. Samwer, M. Reinartz, S. Burggraf, D. M. Herlach, M. Rettenmayr, D. Matson, R. Hyers, *Modeling of Fluid Flow Effects on Experiments using Electromagnetic Levitation in Reduced Gravity*, 148^{th} TMS Annual Meeting & Exhibition 2019, 10.-14. März 2019, San Antonio (Texas), USA (Vortrag)

- M. Rettenmayr, M. Reinartz, S. Burggraf, M. Kolbe, P. Paul, P. K. Galenko, D. M. Herlach, *Solidification of Al-Ni melts under Terrestrial and Microgravity Conditions*, The 7^{th} International Conference on Solidification and Gravity, 3.-6. September 2018, Miskolc-Lillafüred, HU (Vortrag)

- M. Reinartz, S. Burggraf, M. Kolbe, P. Paul, P. K. Galenko, D. M. Herlach, M. Rettenmayr, *Solidification of Al-Ni Melts under Microgravity Conditions*, The 7$^{\text{th}}$ International Conference on Solidification and Gravity, 3.-6. September 2018, Miskolc-Lillafüred, HU (Poster)

- M. Reinartz, S. Burggraf, M. Kolve, P. Paul, S. Koch, P. K. Galenko, D. M. Herlach, M. Rettenmayr, *Study of Nucleation and Growth in Rapidly Solidifying Al-Ni Alloys*, 5$^{\text{th}}$ International Conference on Advances in Solidification Processes, 17.-21. Juni 2019, Salzburg, AU (Vortrag)

Publikationen

- G. Bracker, X. Xiao, J. Lee, M. Reinartz, S. Burggraf, D. M. Herlach, M. Rettenmayr, D. M. Matson, R. W. Hyers, *Modeling of Fluid Flow Effects on Experiments Using Electromagnetic Levitation in Reduced Gravity* in G. Lambotte, J. Lee, A. Allanore, S. Wagstaff (eds.) *Materials Processing Fundamentals 2019* pp. 171-180 (Springer International Publishing, Cham, 2019)

- D. M. Herlach, S. Burggraf, M. Reinartz, P. K. Galenko, M. Rettenmayr, Ch.-A. Gandin, H. Henein, A. Mullis, A. Ilbagi, J. Valloton, *Dendrite growth in undercooled Al-rich Al-Ni melts measured on Earth and in Space*, Physical Review Materials **3** (2019) 073402

- G. P. Bracker, E. B. Baker, J. Nawer, M. E. Sellers, A. K. Gangopadhyay, K. F. Kelton, X. Xiao, J. Lee, M. Reinartz, S. Burggraf, D. M. Herlach, M. Rettenmayr, D. M. Matson, R. W. Hyers, *The effect of flow regime on surface oscillations during electromagnetic levitation experiments*, to be published

Ehrenwörtliche Erklärung

Ich erkläre hiermit ehrenwörtlich, dass ich die vorliegende Arbeit selbständig, ohne unzulässige Hilfe Dritter und ohne Benutzung anderer als der angegebenen Hilfsmittel und Literatur angefertigt habe. Die aus anderen Quellen direkt oder indirekt übernommenen Daten und Konzepte sind unter Angabe der Quelle gekennzeichnet.

Bei der Auswahl und Auswertung folgenden Materials haben mir die nachstehend aufgeführten Personen in der jeweils beschriebenen Weise entgeltlich/unentgeltlich geholfen:

1. Prof. Dr. Markus Rettenmayr (Otto-Schott-Institut für Materialforschung, Friedrich-Schiller-Universität Jena): die Hilfe als mein Betreuer erstreckte sich über sämtliche Bereiche meiner Promotion,

2. Stefan Burggraf (Institut für Materialphysik im Weltraum, Deutsches Zentrum für Luft- und Raumfahrt, Köln): Unterstützung bei der Durchführung und Auswertung der Weltraumexperimente,

3. Gwendolyn Bracker (University of Massachusetts Amherst, USA): Berechnung der Strömungsgeschwindigkeit in Proben, die auf der Raumstation prozessiert wurden,

4. PD Dr. Peter K. Galenko (Otto-Schott-Institut für Materialforschung, Friedrich-Schiller-Universität Jena): Unterstützung bei der Diskussion und Einordnung der Ergebnisse sowie für die Berechnungen zur Erstarrungsgeschwindigkeit mit seinem Modell,

5. Prof. Dr. Dieter M. Herlach (Institut für Materialphysik im Weltraum, Deutsches Zentrum für Luft- und Raumfahrt, Köln): Unterstützung bei der Durchführung der Weltraumexperimente, sowie bei der Diskussion,

6. Prof. Robert W. Hyers (University of Massachusetts Amherst, USA): Berechnung der Strömungsgeschwindigkeit in Proben, die auf der Raumstation prozessiert wurden,

7. Dr. Matthias Kolbe (Institut für Materialphysik im Weltraum, Deutsches Zentrum für Luft- und Raumfahrt, Köln): Vorbereitung und Durchführung der Rasterelektronenmikroskopie sowie Aufbereitung der Daten, und Unterstützung bei der Einordnung und Diskussion meiner Ergebnisse,

8. Prof. Andrew Mullis (University of Leeds, UK): Diskussion der Ergebnisse,

9. Dr. Sonja Steinbach (Institut für Materialphysik im Weltraum, Deutsches Zentrum für Luft- und Raumfahrt, Köln): Vorbereitung und Durchführung der Tomographie sowie Aufbereitung und Diskussion der Ergebnisse,

10. Johannes Wilke (Otto-Schott-Institut für Materialforschung, Friedrich-Schiller-Universität Jena): Unterstützung bei den Geräten zur Probenpräparation und dem Rasterelektronenmikroskop,

11. Robert Wonneberger (Otto-Schott-Institut für Materialforschung, Friedrich-Schiller-Universität Jena): Unterstützung bei den Geräten zur Probenpräparation,

12. Nutzerzentrum für Weltraumexperimente (Deutsches Zentrum für Luft- und Raumfahrt, Köln): Technische Durchführung der Experimente auf der Raumstation,

13. Institut für Materialphysik im Weltraum (Deutsches Zentrum für Luft- und Raumfahrt, Köln): Unterstützung besonders während der ersten sechs Monate meiner Dissertation als Gastdoktorand am Institut in Köln aber auch darüber hinaus.

Weitere Personen waren an der inhaltlich-materiellen Erstellung der vorliegenden Arbeit nicht beteiligt. Insbesondere habe ich hierfür nicht die entgeltliche Hilfe von Vermittlungs- bzw. Beratungsdiensten (Promotionsberater oder andere Personen) in Anspruch genommen. Niemand hat von mir unmittelbar oder mittelbar geldwerte Leistungen für Arbeiten erhalten, die im Zusammenhang mit dem Inhalt der vorgelegten Dissertation stehen.

Die Arbeit wurde bisher weder im In- noch im Ausland in gleicher oder ähnlicher Form einer anderen Prüfungsbehörde vorgelegt.

Die geltende Promotionsordnung der Physikalisch-Astronomischen Fakultät ist mir bekannt.

Ich versichere ehrenwörtlich, dass ich nach bestem Wissen die reine Wahrheit gesagt und nichts verschwiegen habe.

Jena, den 08. Juli 2020

Danksagung

Am Ende dieser Dissertation möchte ich mich bei allen bedanken, die mir in den verschiedensten Situationen während meiner Promotion geholfen und mich unterstützt haben.

Als erstes danke ich Professor Dr. Markus Rettenmayr dafür, dass er mich in seine Gruppe aufgenommen hat, und mir die Möglichkeit geboten hat, meine Dissertation bei ihm anzufertigen. Ich danke ihm für das in mich gesetzte Vertrauen bei der Durchführung der Experimente auf der ISS und während der Parabelflüge. Außerdem bot er mir vielfältige Möglichkeiten meine Arbeit auf Konferenzen und internationalen Meetings zu präsentation. Dabei hat mir seine Anleitung bei der Vorbereitung sehr geholfen. Ich bin ihm für seine Hilfe und Unterstützung auch in schwierigen Phasen meiner Promotion sehr dankbar.

Außerdem danke ich Professor Dr. Dieter Herlach für die Ratschläge und Unterstützung, die er mir zukommenließ. Bei den Experimenten auf der Raumstation und der Diskussion meiner Ergebnisse war er eine sehr große Hilfe.

Bezüglich der Experimente auf der ISS möchte ich mich bei allen beteiligten Mitarbeitern des Microgravity User Support Centers (MUSC) am Deutschen Zentrum für Luft- und Raumfahrt (DLR) in Köln bedanken. Dabei möchte ich besonders Dr. Stephan Schneider, Dr Julianna Schmitz, Dr. Sandra Schumann, Dr. Jan Gegner, Dr. Mitja Beckers und Dr. Marc Engelhardt hervorheben, die während der Nachtschichten die Steuerung des Aufbaus übernommen haben, und für ein angenehmes Arbeiten auch mitten in der Nacht gesorgt haben.

Besonders danke ich Dr. Matthias Kolbe vom Institut für Materialphysik im Weltraum, DLR Köln, für die Rasterelektronenmikroskopie und EBSD-Messungen. Die Diskussionen mit ihm waren für mich sehr hilfreich, um die Ergebnisse zu strukturieren und einzuordnen.

Dr. Sonja Steinbach ebenfalls vom Institut für Materialphysik im Weltraum danke ich sehr für die tomographischen Messungen und die Hilfe sowohl bei der Auswertung und Diskussion der Daten.

Außerdem danke ich Dr. Peter Galenko für die Unterstützung bei der Erstellung von Publikationen und der Diskussion meiner Ergebnisse.

Stellvertretend für alle, die bei der Europäischen Raumfahrtorganisation (ESA) und den Industriepartnern für den ISS-EML zuständig sind, möchte ich mich sehr bei Dr. Wim Sillekens (ESA) bedanken.

Der Arbeitsgruppe Metallische Werkstoffe der Uni Jena danke ich sehr für die herzliche Aufnahme. Ohne die Hilfe bei der Reparatur des EMLs und den Tipps, Ratschlägen und Diskussionen hätte die Arbeit deutlich länger gedauert. Dafür danke ich Tobias Kaaden und Anton Zimare. Besonders danke ich Stefanie Koch für ihre Hilfe und guten Tipps und die sonstige Unterstützung.

In den ersten Monaten meiner Arbeit an der FSU Jena war ich an das Institut für Materialphysik im Weltraum, DLR Köln, abgeordnet. Daher danke ich dem Institut und dem DLR für die Unterstützung, die mir in dieser Zeit, aber auch darüber hinaus zukam.

Diese Arbeit wurde im Rahmen eines DFG-Projektes (HE1601/26) und des ESA-MAP-Projektes NEQUISOL (15236/02/NL/SH) angefertigt. Daher danke ich der DFG und ESA sehr für diese Unterstützung.